UNIVERSITY OF SOUTHAMPTON

FACULTY OF ENGINEERING, SCIENCE & MATHEMATICS

OPTOELECTRONICS RESEARCH CENTRE

Optical Fibre Nanowire Devices

by

Fei Xu

Thesis for the degree of Doctor of Philosophy

Oct 2008

UNIVERSITY OF SOUTHAMPTON

ABSTRACT

FACULTY OF ENGINEERING, SCIENCE & MATHEMATICS

OPTOELECTRONICS RESEARCH CENTRE

Doctor of Philosophy

Optical Fibre Nanowire Devices

by Fei Xu

The Optical Fibre Nanowire (OFN) is a potential building block in future micro- and nano-photonic device since it offers a number of unique optical and mechanical properties. In this thesis, the background and fundamental features of nanowires are introduced; the theory, design and demonstration of novel nanowire devices are discussed.

At first, a short adiabatic taper tip is manufactured, and it is used as optical tweezers for trapping 1μm microspheres.

Then, the most important devices - the OFN resonators including the simple Optical Nanowire Loop Resonator (ONLR) and complicated 3D Optical Nanowire Microcoil Resonator (OMNR) - are investigated theoretically and experimentally. A one-turn loop resonator and two-, three-, and four-turn ONMR are demonstrated experimentally; several kinds of methods on optimizing the ONMR profile are presented to make the manufacture of high-Q ONMRs easier. In order to protect and stabilize the ONMR, embedding the device in Teflon is demonstrated.

Finally, more applications in refractometric sensing are presented: schemes of sensors based on an embedded ONLR and ONMR are presented. The sensor sensitivities are calculated: 700 nm/RIU (RIU is the Refractive Index Unit) can be achieved at the wavelength of 970 nm for a diameter of 600 nm. Additionally, a refractometric sensor based on an embedded ONMR is demonstrated experimentally; its sensitivity is about 40 nm/RIU.

Contents

List of Figures

List of Tables

DECLARATION OF AUTHORSHIP

I, Fei Xu declare that the thesis entitled *Optical fibre nanowire devices* and the work presented in the thesis are both my own, and have been generated by me as the result of my own original research. I confirm that:

- this work was done wholly or mainly while in candidature for a research degree at this University;
- where any part of this thesis has previously been submitted for a degree or any other qualification at this University or any other institution, this has been clearly stated;
- where I have consulted the published work of others, this is always clearly attributed;
- where I have quoted from the work of others, the source is always given. With the exception of such quotations, this thesis is entirely my own work;
- I have acknowledged all main sources of help;
- where the thesis is based on work done by myself jointly with others, I have made clear exactly what was done by others and what I have contributed myself;
- Parts of this work have been published in the journal articles and conference proceedings reported in the list of publications at the end of the thesis.

Signed: ………Fei Xu…………………………………………………..

Date:………May 2008…………………………………………………….

Acknowledgements

It is my most pleasant task to acknowledge the help that I have received from a lot of nice people in the ORC during my PhD. In particular, I am deeply indebted to Dr. Gilberto Brambilla for his constant guidance, assistance and understanding. He is an excellent tutor with great patience, especially as I had no experience in fibre technology at the beginning of my study; and he is a very kind friend to help me and give me supports and opportunities as much as possible.

I am also greatly appreciative of Dr. Neil Broderick for his generous support, he gave me the opportunity to study here and so much help on my work during these years, and he spent a lot of time on my thesis, making it much better than the original version.

It was my great pleasure to work with Dr. Peter Horak after the ORC fire; he helped me to start the simulation on 3D resonators and polished my papers during the most difficult period.

I would like to thank Prof James Wilkinson, who was my examiner of the nine and fifteen months reports, he gave me a lot of suggestions for my work ,and also suggested that we use Teflon as a coating material.

I also received a lot of help and suggestions from Dr. Xian Feng, Dr. Tracy Melvin, Dr. Bill Brocklesby, Dr. Wei Loh, Dr. Jayanta Sahu, Prof. Dave Richardson, Dr. Senthil Ganapathy, Dr. Jerry Prawiharjo, Dr. Chung-Che Huang, Mrs. Ping Hua…, I often borrowed some samples or equipment from their groups, too.

A special thank to Mrs. Eve Smith for her friendly help and administrative support throughout my study. I am also indebted to Dr. Eleanor Tarbox for her advice on my study and life, and constructive comments on this thesis; Mrs. Janet Mansour, Mrs. Wendy White, Mr. Ed Weatherby, Mr. Kevin Sumner, Miss Tanya Morrow, Mr. Mark Lessey, Miss Zoe Evans, Mrs Mandy Both, Miss Tina Clark, Mr. Chris Nash, Mr. Robert Standish, Mr. Andrew Webb, and Mr. Lee Whitelock, they gave me so much help and made things convenient.

Of course, I am so happy to know many students during these years, and thank these students who helped me: Yuwapat Panitchob, Adriaan van Brakel, Gregor Elliott, Huw Major, Mukhzeer Mohamad Shahimin, Kang Kang Chen,

Junhua Ji,, Zhaowei Zhang, Weijia Yang, Fei He, Chun Tian, Chong Yew Lee, Hamish Hunt, Christopher Holmes, Mridu Kalita, Srinivasan Iyer, Natasha Vukovic.

I also would like to thank the British Council and the Optoelectronics Research Centre for Overseas Research Students Awards and other financial support, and the Institution of Engineering and Technology for the travel grant.

Last but not least, my utmost gratitude to my parents, sister and girl friend for their love and support.

Acronyms

3D	Three Dimension
CMCRS	Coated Microfibre Coil Resonator Sensor
CW	Continuous-Wave
EDFA	Erbium-doped Optical Fiber Amplifier
ENLR	Embedded Nanowire Loop Resonator
FSR	Free Spectral Range
FWHM	Full Width at Half Maximum
MCR	Microfibre Coil Resonators
OFN	Optical Fibre Nanowire
ONLR	Optical Nanowire Loop Resonator
ONMR	Optical Nanowire Microcoil Resonator
OSA	Optical Spectrum Analysis
PMMA	PolyMethylMethAcrylate
RIU	Refractive Index Unit
SNOM	Scanning Near-Field Optical Microscopy
TR	Tolerance Ratio

Chapter1

Introduction

1.1 Scope and Objective

This thesis is based on my work on Optical Fibre Nanowire (OFN) from Jan 2005, related to fundamental theoretical characteristics, loss, and experimental demonstration of several kinds of OFN devices. The main objective of this research is to develop an understanding of the aspects related to the fundamental characteristic of nanowires, and to the theory, design and demonstration of novel nanowire devices. The key topics underlying this work can be summarized as follows:

- To develop an understanding of the fundamental theoretical properties, loss and manufacture technique of OFN.
- To develop an understanding of the theory of OFN shape, design and manufacture short adiabatic taper tips for optical tweezers.
- To investigate theoretically and demonstrate experimentally resonators based on nanowires (simple loop resonator; complex 3D-multicoil resonator).
- To develop novel sensors based on microfibre resonators.

1.2 Optical Fibre Tapers and Nanowires

Since Kao and Hockham of “Standard Telephones and Cables” proposed glass waveguides as a practical medium for communication in 1965, optical fibres have been the basis of the modern information society. The most common fibre is the standard telecom single mode fibre (SMF-28), which has a diameter of 125 μm and a core of 10 μm; fibre devices based on this kind of fibre have found a wide range of application in optical communications, sensing, optics, biology, medicine and much more [1-4]. However, for a number of applications, it is important to reduce the fibre diameter as this increases the evanescent field allowing for strong interaction with the environment. A simple way to reduce the diameter of the fibre is to taper it. Optical fibre tapers are made by stretching a heated fibre, forming a structure comprising a narrow stretched filament (the taper waist) each end of which is linked to an unstretched fibre by a conical section (the taper transition), as shown in Fig. 1.1.

Fig. 1.1: Illustration of an optical fibre taper.

For a tapered fibre obtained from a standard single-mode fibre whose diameter has been reduced to submicrometer range, it is possible that an appreciable part of the guided power is guided outside the taper. A lot of applications such as modal interferometers and spectral filters or sensors [5-7], arise from the possibility of acting directly on the guided field by the intermediary of the refractive index of the exterior medium with chemicals as external media [8]. Tapers can also be considered in atomic optics to reflect De Broglie waves by using radiative forces produced by intense evanescent waves, serving as ‘‘atomic mirrors’’ and replacing the amplification system at much lower cost [8, 9]. Bures’ calculation showed that it is possible to obtain theoretical densities in the range of 10^8 W/cm^2 at the fibre surface for the fundamental HE_{11} mode carrying a power of 1 Watt [10]. Additionally, tapers have often been used in nonlinear optics [11]. More and more applications require minimizing the diameter of the taper to nanometre dimensions resulting in OFN. In this thesis, an OFN is a fibre taper with a waist of submicrometer- and nanometer- diameter (tens to thousands times thinner than the commonly used micrometer-diameter waveguides). Sometimes, an OFN is called a microfibre or nanofibre.

For tapered fibre applications, the mode size is important because it is related to the intensity distribution and to the evanesce field. J.D. Love first showed the relationship between the fundamental mode size and the taper diameter [12]. The spot size ω of the light propagating in the taper is strongly dependent on the diameter ϕ [12] through the V number:

$$\mathrm{V} = \frac{2\pi}{\lambda}\frac{\phi}{2} NA \tag{1.1}$$

where NA represents the numerical aperture and λ the wavelength. V_{cl} has been calculated from Eq. (1.1) for a mode confined by the silica-air interface (NA~1 if the silica and air refractive indices are taken to be 1.444 and 1 respectively).

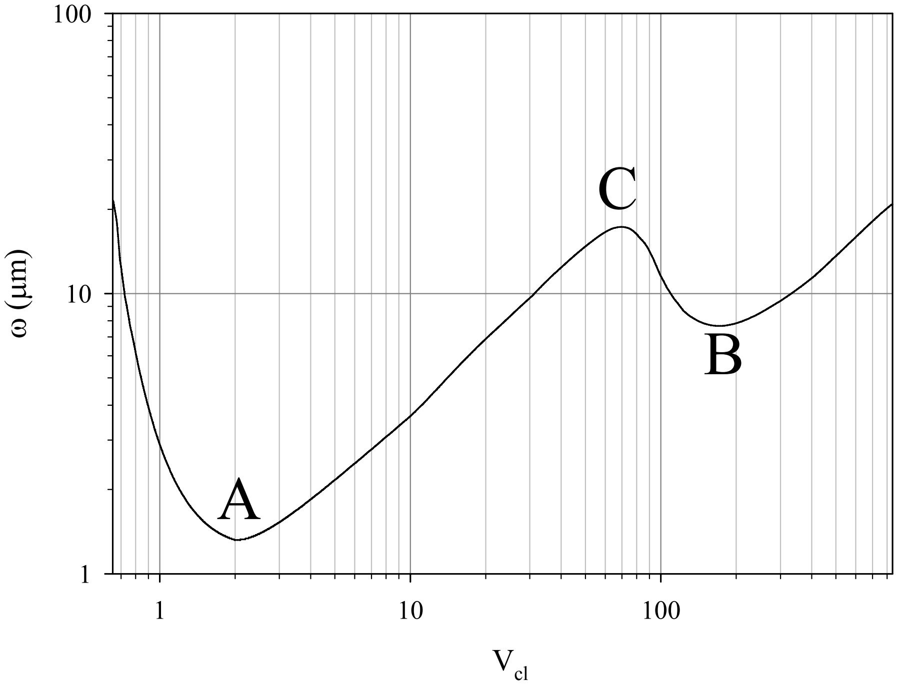

Fig. 1.2 Dependence of the spot size [12] on the cladding V number of a tapered telecom fiber; A and B are the points of maximum confinement in the cladding (A) and in the core (B), C the cladding guiding condition for which is maximized. V is related to the cladding diameter by Eq. (1.1).

A telecom optical fiber is positioned at the right in Fig. 1.2. When the optical fiber diameter decreases, V_{cl} decreases and ω initially decreases until a minimum point (B) is reached; this is the maximum confinement within the core. After that, the mode is no longer guided in the core and ω suddenly increases to a maximum (C) associated with cladding guiding. For even smaller diameters ω decreases with decreasing V until it reaches a minimum (A) for V~2 and then it increases again. This region at V<2 is typical of OFNs: the mode is only weakly guided by the waveguide, ω can be orders of magnitude bigger than the physical diameter of the OFN and a larger fraction of the power resides in the evanescent field. When the diameter is about several hundred nanometres to several micrometers, the ratio between the mode size and the diameter is very small and the intensity is high; when the diameter is less than several hundred nanometers, the evanescent field is large and the intensity is spread over a large area.

Applications of OFNs have previously been limited because of the difficulties in fabricating low-loss submicron structures. Traditional taper diameters were tens of micrometers. With the development of computer-controllable taper rigs, it has been possible to manufacture precise and thinner tapers [13]. Prior to 2003 two attempts to manufacture sub-wavelength wires using a top-down process have been reported in literature [13, 14]. In Ref 13, Bures obtained a 400nm-diameter OFN but the loss was very large and difficult to reproduce. In December 2003 Tong et al. presented a two-step process to fabricate low-loss sub-wavelength silica wires [15], which involved wrapping and drawing a pre-tapered section of standard fibre around a heated sapphire tip. Although the measured loss was orders of magnitude higher than that achieved later with flame-brushing techniques [16], it was low enough to open the way to a host of new devices for optical communications, sensing, lasers, biology and chemistry. Then single-step fabrication techniques were reported: researchers at the University of

Southampton [16] pulled the nanofibres by using the standard manufacturing method of fibre tapers and couplers: this is based on a small flame moving under an optical fibre which is heated and stretched (flame-brushing technique); simultaneously researchers at OFS inc.[17] replaced the small flame with a sapphire capillary tube (microfurnace) heated by a CO_2 laser beam.

1.3 Properties and Applications of Nanowires

With the development of new fabrication methods, nanowires with length in excess of 100 millimetres, radii as small 30nm [18] and losses as small as ~0.001dB/mm [19] can be produced. They have the potential to become building blocks in future micro- and nano-photonic devices since they offer a number of unique optical and mechanical properties, including:

- Large evanescent fields; for very small OFN radii (red region in Fig. 1.2) a considerable fraction of the transmitted power can propagate in the evanescent field outside of a nanowire [15, 16]. This allows for the fabrication of atom guides [20], sensors [21, 22] and high-Q resonators [23, 24].

- High nonlinearity; at marginally bigger diameters (around point A in fig. 1.2) light can be confined to a very small area over long device lengths allowing the ready observation of nonlinear interactions, such as supercontinuum generation [19, 25, 26], at relatively modest power levels.

- Extreme flexibility and configurability; nanowires can easily be bent and manipulated and yet remain relatively strong mechanically. Bend radii of the order of a few microns can be readily achieved with relatively low induced bend loss [15, 27] allowing for highly compact devices with complex geometry e.g. two-dimension (2D) and three-dimension (3D) multi-ring resonators [28].

- Low-loss interconnection to other fibres and fiberized components; OFN are fabricated by stretching optical fibres and thus preserve the original dimensions of the optical fibre at their input and output (Fig. 1.1) allowing ready splicing to standard fibres. This represents a significant advantage when compared to small-core microstructured fibres that always present significant insertion/extraction losses.

There are a number of applications of OFN that have been reported. Amongst these, a fraction is based on fibre taper tips. A fibre taper tip is an OFN with only one output or input end and a taper transition. A fibre taper tip can be obtained by breaking the whole OFN, and it can be fabricated by pipette puller, or by etching. One important application of optical fibre tips is optical trapping as optical tweezers. Optical tweezers use forces exerted by a strongly focused beam of light to trap small objects. The force is based on the transfer of momentum between the beam of radiation and the object that it is passing through. A sharp tip is preferred because the near field close to the sharp tip mainly consists of evanescent components which decay rapidly with distance from the tip, which could generate a trapping potential deep enough to overcome Brownian motion and capture a nanometric particle [29]. Low loss is also important as high power sources are expensive. The use of short ultra-low loss fibre tips have been used as high efficient optical tweezers with low powers (~10 mW) [30].

Other applications of OFN are based on microresonators. In recent years, research interest in optical microresonators has grown dramatically. This is due to the perception of their great potential in optical communications, sensing, signal processing applications, and quantum optics, just to cite a few. Optical microresonators with a size less than a few millimeters confine light to small volumes. A microscale volume ensures that the resonant frequencies are more sparsely distributed than they are in a corresponding ‘macroscale’ resonator. Microresonators have been achieved with a range of different designs, including whispering gallery resonators [31-34], microring resonators [35-37], micropost (or micropillar) cavities [38, 39], photonic crystal defect microcavities [40], microdisk [41], Fabry-Perot bulk optical cavity [42], microspheres [43] etc. Such microresonators are ideally suited for numerous applications in science and technology, for example, for the realization of microlasers, narrow filters, optical switching, ultrafine sensing, displacement measurements, high resolution spectroscopy, and studies of nonlinear optical effects.

There are two kinds of OFN resonators: the simple loop resonator and the more complicated 3D microcoil resonator. In 2004, the self-touching optical nanowire loop resonator (ONLR) was first fabricated at OFS inc. [23] by bending a microfibre on itself and keeping two sections of a microfibre together by taking advantage of surface attraction forces (Wan der Waals and electrostatic), as shown in Fig.1.3. The diameter of the OFN was 900 nm and the Q-factor of the resonator was ~120,000. A major drawback of the self-touching loop resonator in air is its geometrical stability; the coupling is strongly affected by the microcoil geometry and a small change in shape results in a large change in its transmission properties. Fig. 1.4 shows another type of loop resonator: the knot resonator [44], which is manufactured by knotting a broken nanowire by hand (using a microscope). Knot resonators have the benefit of a long, stable, coupling region but they present severe drawbacks including the complexity of fabrication, the need to break the microfibre to make a knot, the necessity for an additional coupler at the output or input of the resonator, high loss and the presence of only one standard telecom fibre pigtail.

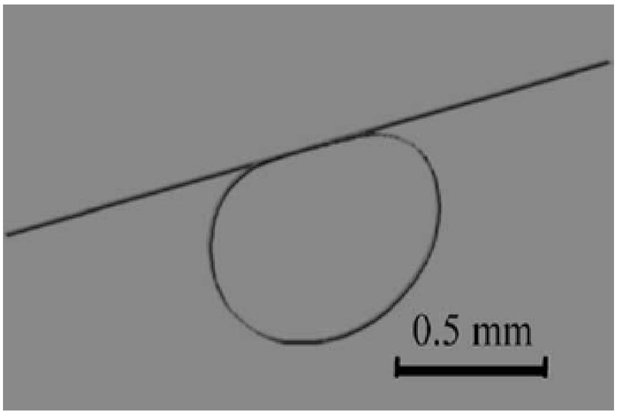

Fig. 1.3: Picture of ONLR by Sumetsky[23].

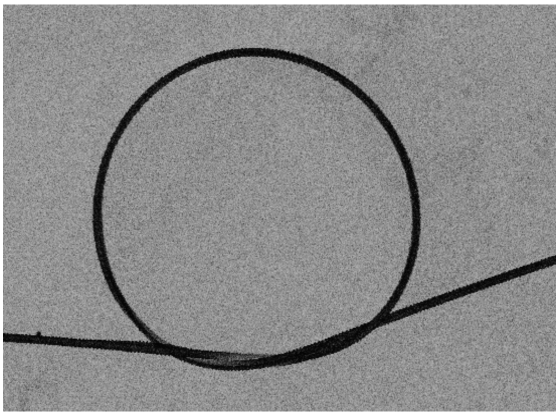

Fig. 1.4: Illustration of the knot resonator fabricated at the ORC.

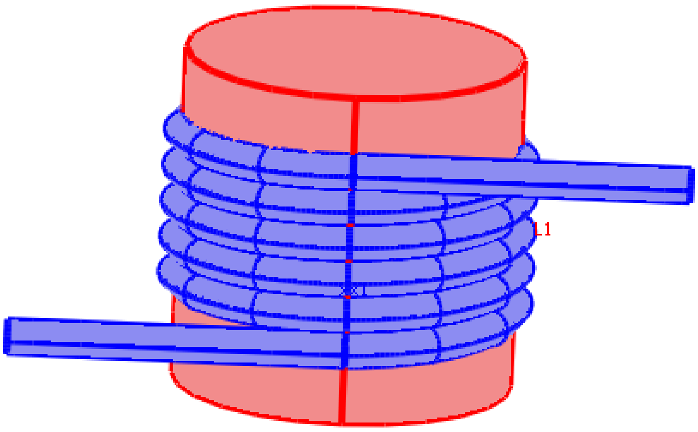

Fig. 1.5: Illustration of ONMR[28].

In 2004, a three-dimension multiple-turn optical nanowire microcoil resonator (ONMR) was proposed [28] as shown in Fig. 1.5. ONMRs wrapped on a low index rod can overcome the problem of stability and have the potential of using this device as a basic functional element for the microfibre-based photonics. The 3D ONMR-based optical devices have two significant advantages over planar devices: smaller losses and greater compactness. The manufacture is still difficult because the OFN is liable to be broken during wrapping. Prior to 2007, experimental demonstrations of ONMRs were reported in liquid [45] and in air [46]. In order to obtain a practical device, the ONMR was coated with low index polymer Teflon [47].

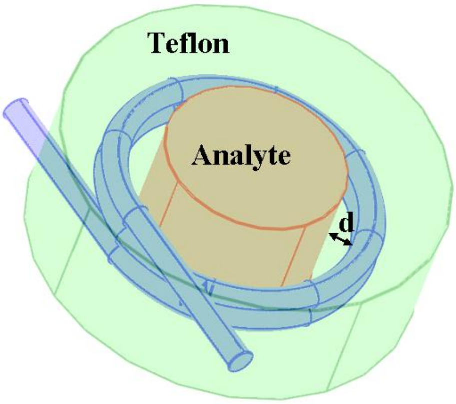

Fig. 1.6: Illustration of a sensor based on coated ONMR. The blue one is the nanowire, the green part is the coating and the grey one is the analyte channel.[48].

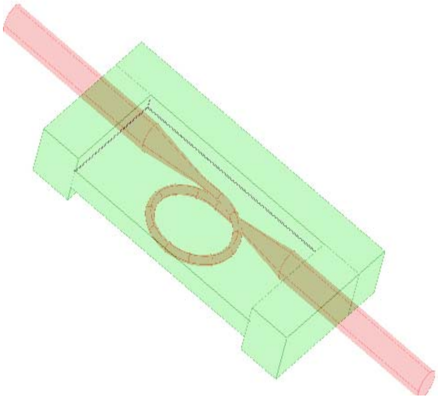

Fig. 1.7: Illustration of a sensor based on coated ONLR. The red one is the nanowire, the green part is the coating [49].

The development of our manufacturing techniques for ONMR and ONLR made it possible for them to be employed as high sensitivity microfludic sensors [49, 50]. Generally, a thick coating is preferred for good protection but a thin coating allows for a large evanesce field. Two configurations solved the problem of the balance between coating thickness and evanescence field as shown in Fig. 1.6 and Fig. 1.7. A sensor based on a coated ONMR was manufactured by removing the disposable rod in a coated ONMR; the second sensor based on a coated ONLR was manufactured by putting the loop resonator between two disposable substrates and then removing the two substrates. Sensitivity as high as 700 nm/RIU was predicted, where RIU is the refractive index unit. In 2008, the two sensors were experimentally demonstrated.

1.4 Outline

In this thesis, I investigate the waveguide characteristics and loss of OFNs; fabricate very short adiabatic tapers for optical tweezers, simple loop resonators, complex 3D-microcoil resonator; and present an optical microfibre coil resonator refract metric sensor.

The thesis outline is as follows:

- Chapter 2 reviews several manufacturing methods of fibre taper and OFN, and the theory of the shape model of fibre tapers.
- Chapter 3 reviews the fundamental waveguide theory of fibre taper and calculate some important parameters such as effective index, and power fractal factor.
- Chapter 4 presents the mechanics of loss in nanowires, the measurement of internal loss, and the demonstration of long-term transmission stability.
- Chapter 5 introduces the theory and manufacture of short adiabatic optical tapers for tweezers. Experiments on optical trapping of 1μm-diameter microsphere are shown.

- Chapter 6 presents the fabrication and spectrum of optical nanowire loop resonator, the stabilization of ONLR by sandwiching them between two aerogel, and the fabrication of a filter by combining two ONLRs.

- Chapter 7 introduces and analyses a 3D resonator; the mode theory was used to obtain the transmission spectra and three kinds of optimum method were presented to facilitate the manufacture of high-Q 3D microcoil resonators.

- Chapter 8 discusses the experimental manufacture of Optical Microfibre Coil Resonators and their embedding in Teflon.

- Chapter 9 presents new sensors based on ONLR and ONMR, their manufacture, the evaluation of their sensitivity and a comparison with current sensor. The experimental results of ONMR sensor are also reported.

- Chapter 10 is the summary.

1.5 References

1. M. Yamane, Y. Asahara, and ebrary Inc., *Glasses for photonics* (Cambridge University Press, Cambridge, [England] ; New York, 2000).

2. G. P. Agrawal, *Fiber-optic communication systems* (Wiley-Interscience, New York, 2002).

3. G. P. Agrawal, *Nonlinear fiber optics* (Academic Press, San Diego, 2001).

4. G. P. Agrawal, *Applications of nonlinear fiber optics* (Academic Press, San Diego, 2001).

5. S. Lacroix, F. Gonthier, and J. Bures, "All-Fiber Wavelength Filter from Successive Biconical Tapers," Optics Letters **11**, 671-673 (1986).

6. S. L. F. Gonthier, X. Daxhelet, R. J. Black, and J. Bures, "Broadband all-fiber filters for wavelength division multiplexing applications," Applied Physics Letters **54**, 1290-1292 (1989).

7. K. Lewotsky, "Taper enhances sensitivity of immunoassay sensor," Laser Focus World **33**, 46-52 (1997).

8. J. Bures, and R. Ghosh, "Power density of the evanescent field in the vicinity of a tapered fiber," J. Opt. Soc. Am. A **16**, 1992-1996 (1999).

9. A. Landragin, J. Y. Courtois, G. Labeyrie, N. Vansteenkiste, C. I. Westbrook, and A. Aspect, "Measurement of the van der Waals force in an atomic mirror," Physical Review Letters **77**, 1464-1467 (1996).

10. J. Bures, and R. Ghosh, "Power density of the evanescent field in the vicinity of a tapered fiber," Journal of the Optical Society of America a-Optics Image Science and Vision **16**, 1992-1996 (1999).

11. P. Dumais, F. Gonthier, S. Lacroix, J. Bures, A. Villeneuve, P. G. J. Wigley, and G. I. Stegeman, "Enhanced self-phase modulation in tapered fibers," Optics Letters **18**, 1996-1998 (1993).

12. J. D. Love, "Spot size, adiabaticity and diffraction in tapered fibres," Electronics Letters **23**, 993-994 (1987).

13. F. Bilodeau, K. O. Hill, D. C. Johnson, and S. Faucher, "Compact, Low-Loss, Fused Biconical Taper Couplers - Overcoupled Operation and Antisymmetric Supermode Cutoff," Optics Letters **12**, 634-636 (1987).

14. F. Bilodeau, K. O. Hill, S. Faucher, and D. C. Johnson, "Low-Loss Highly Overcoupled Fused Couplers - Fabrication and Sensitivity to External-Pressure," Journal of Lightwave Technology **6**, 1476-1482 (1988).

15. L. M. Tong, R. R. Gattass, J. B. Ashcom, S. L. He, J. Y. Lou, M. Y. Shen, I. Maxwell, and E. Mazur, "Subwavelength-diameter silica wires for low-loss optical wave guiding," Nature **426**, 816-819 (2003).

16. G. Brambilla, V. Finazzi, and D. J. Richardson, "Ultra-low-loss optical fiber nanotapers," Optics Express **12**, 2258-2263 (2004).

17. M. Sumetsky, Y. Dulashko, and A. Hale, "Fabrication and study of bent and coiled free silica nanowires: Self-coupling microloop optical interferometer," Optics Express **12**, 3521-3531 (2004).

18. G. Brambilla, F. Xu, and X. Feng, "Fabrication of optical fibre nanowires and their optical and mechanical characterisation," Electronics Letters **42**, 517-519 (2006).

19. S. G. Leon-Saval, T. A. Birks, W. J. Wadsworth, P. S. J. Russell, and M. W. Mason, "Supercontinuum generation in submicron fibre waveguides," Optics Express **12**, 2864-2869 (2004).

20. F. Le Kien, V. I. Balykin, and K. Hakuta, "Atom trap and waveguide using a two-color evanescent light field around a subwavelength-diameter optical fiber," Physical Review A **70**, 011401 (2004).

21. J. Villatoro, and D. Monzon-Hernandez, "Fast detection of hydrogen with nano fiber tapers coated with ultra thin palladium layers," Optics Express **13**, 5087-5092 (2005).

22. J. Y. Lou, L. M. Tong, and Z. Z. Ye, "Modeling of silica nanowires for optical sensing," Optics Express **13**, 2135-2140 (2005).

23. M. Sumetsky, Y. Dulashko, J. M. Fini, A. Hale, and D. J. DiGiovanni, "Demonstration of a microfiber loop optical resonator," in *Optical Fiber*

Communication Conference, 2005. Technical Digest. OFC/NFOEC(2005), p. 3 pp. Vol. 5.

24. M. Sumetsky, Y. Dulashko, J. M. Fini, A. Hale, and D. J. DiGiovanni, "The microfiber loop resonator: Theory, experiment, and application," Journal of Lightwave Technology **24**, 242-250 (2006).

25. W. J. Wadsworth, A. Ortigosa-Blanch, J. C. Knight, T. A. Birks, T. P. M. Man, and P. S. Russell, "Supercontinuum generation in photonic crystal fibers and optical fiber tapers: a novel light source," Journal of the Optical Society of America B-Optical Physics **19**, 2148-2155 (2002).

26. G. Brambilla, F. Koizumi, V. Finazzi, and D. J. Richardson, "Supercontinuum generation in tapered bismuth silicate fibres," Electronics Letters **41**, 795-797 (2005).

27. L. M. Tong, J. Y. Lou, R. R. Gattass, S. L. He, X. W. Chen, L. Liu, and E. Mazur, "Assembly of silica nanowires on silica aerogels for microphotonic devices," Nano Letters **5**, 259-262 (2005).

28. M. Sumetsky, "Optical fiber microcoil resonator," Optics Express **12**, 2303-2316 (2004).

29. L. Novotny, R. X. Bian, and X. S. Xie, "Theory of nanometric optical tweezers," Physical Review Letters **79**, 645-648 (1997).

30. G. Brambilla, G. Brambilla, and F. Xu, "Adiabatic submicrometric tapers for optical tweezers," Electronics Letters **43**, 204-206 (2007).

31. V. B. Braginsky, M. L. Gorodetsky, and V. S. Ilchenko, "Quality-Factor and Nonlinear Properties of Optical Whispering-Gallery Modes," Physics Letters A **137**, 393-397 (1989).

32. V. S. Ilchenko, A. A. Savchenkov, A. B. Matsko, and L. Maleki, "Dispersion compensation in whispering-gallery modes," Journal of the Optical Society of America a-Optics Image Science and Vision **20**, 157-162 (2003).

33. J. C. Knight, G. Cheung, F. Jacques, and T. A. Birks, "Phase-matched excitation of whispering-gallery-mode resonances by a fiber taper," Optics Letters **22**, 1129-1131 (1997).

34. S. M. Spillane, T. J. Kippenberg, O. J. Painter, and K. J. Vahala, "Ideality in a fiber-taper-coupled microresonator system for application to cavity quantum electrodynamics," Physical Review Letters **91**, 043902 (2003).

35. S. T. Chu, B. E. Little, W. G. Pan, T. Kaneko, S. Sato, and Y. Kokubun, "An eight-channel add-drop filter using vertically coupled microring resonators over a cross grid," IEEE Photonics Technology Letters **11**, 691-693 (1999).

36. B. E. Little, S. T. Chu, H. A. Haus, J. Foresi, and J. P. Laine, "Microring resonator channel dropping filters," Journal of Lightwave Technology **15**, 998-1005 (1997).

37. D. Rafizadeh, J. P. Zhang, S. C. Hagness, A. Taflove, K. A. Stair, S. T. Ho, and R. C. Tiberio, "Waveguide-coupled AlGaAs/GaAs microcavity ring and disk resonators with high finesse and Z1.6-nm free spectral range," Optics Letters **22**, 1244-1246 (1997).

38. J. M. Gerard, D. Barrier, J. Y. Marzin, R. Kuszelewicz, L. Manin, E. Costard, V. ThierryMieg, and T. Rivera, "Quantum boxes as active probes for photonic microstructures: The pillar microcavity case," Applied Physics Letters **69**, 449-451 (1996).

39. J. M. Gerard, B. Sermage, B. Gayral, B. Legrand, E. Costard, and V. Thierry-Mieg, "Enhanced spontaneous emission by quantum boxes in a monolithic optical microcavity," Physical Review Letters **81**, 1110-1113 (1998).

40. O. Painter, R. K. Lee, A. Scherer, A. Yariv, J. D. O'Brien, P. D. Dapkus, and I. Kim, "Two-dimensional photonic band-gap defect mode laser," Science **284**, 1819-1821 (1999).

41. K. Djordjev, S. J. Choi, S. J. Choi, and P. D. Dapkus, "Microdisk tunable resonant filters and switches," Ieee Photonics Technology Letters **14**, 828-830 (2002).

42. J. R. Buck, and H. J. Kimble, "Optimal sizes of dielectric microspheres for cavity QED with strong coupling," Physical Review A **67**, 033806 (2003).

43. D. W. Vernooy, V. S. Ilchenko, H. Mabuchi, E. W. Streed, and H. J. Kimble, "High-Q measurements of fused-silica microspheres in the near infrared," Optics Letters **23**, 247-249 (1998).

44. X. S. Jiang, L. M. Tong, G. Vienne, X. Guo, A. Tsao, Q. Yang, and D. R. Yang, "Demonstration of optical microfiber knot resonators," Applied Physics Letters **88**, 223501 (2006).

45. M. Sumetsky, "Demonstration of a multi-turn microfiber coil resonator," in *Optical Fiber Communication Conference*(San Diego, USA, 2007).

46. F. Xu, and G. Brambilla, "Manufacture of 3-D Microfiber Coil Resonators," IEEE Photonics Technology Letters **19**, 1481-1483 (2007).

47. F. Xu, and G. Brambilla, "Embedding optical microfiber coil resonators in Teflon," Optics Letters **32**, 2164-2166 (2007).

48. F. Xu, P. Horak, and G. Brambilla, "Optical microfiber coil resonator refractometric sensor," Optics Express **15**, 7888-7893 (2007).

49. F. Xu, V. Pruneri, V. Finazzi, and G. Brambilla, "An embedded optical nanowire loop resonator refractometric sensor," Optics Express **16**, 1062-1067 (2008).

50. F. Xu, P. Horak, and G. Brambilla, "Optical microfiber coil resonator refractometric sensor," Optics Express **15**, 7888-7893 (2007).

Chapter 2

Manufacture of Fibre Tapers and Nanowires

An essential precondition for practical applications of fibre tapers is the ability to manufacture smooth, low-loss and arbitrary-profile fibre tapers and nanowires. In this chapter, several methods of manufacturing tapers are reviewed. In my thesis, the flame brushing technique is used to manufacture fibre tapers and nanowires, and a pipette puller to manufacture fibre tips. Hence these two methods are discussed in detail. In addition, the theory on the design of the fibre taper shape is also reviewed.

2.1 Methods of Manufacturing Fibre Tapers

In the last few years optical fibre tapers and nanowires have been manufactured using just a few different methods:

The first technique is based on a two step process by Tong et al. [1] as shown in Fig. 2.1: first, a fibre is pre-tapered to a diameter of several micrometers using conventional flame techniques; then, the pre-tapered fibre is wound on a sapphire tip, which is heated by a flame at a distance from the fibre, and drawn further to a submicron diameter. It is believed that the sapphire tip confines the heating to a small volume and helps to maintain a stable temperature distribution. This method has been used to manufacture extremely small-diameter wires: nanowires with radii in the region of 10nm have been fabricated. On the other hand, it presents drawbacks such as complex fabrication procedure and a relatively high loss (~0.1 dB/mm at r~430 nm and λ~1.55 μm).

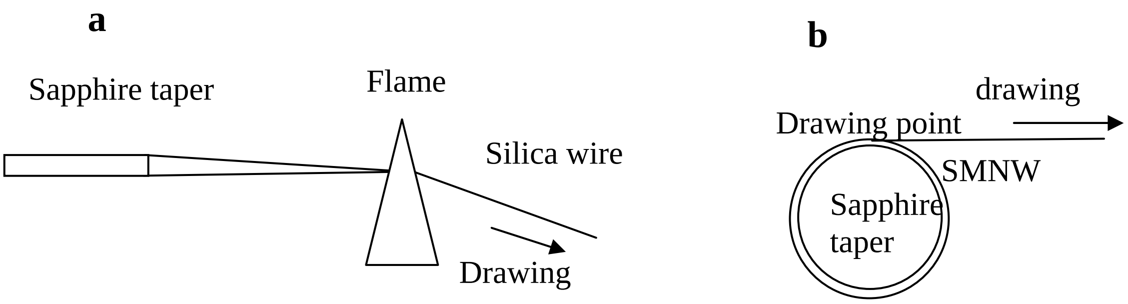

Fig. 2.1: **a**, Schematic diagram of the drawing of the wire from a coil of micrometre-diameter silica wire wound around the tip of a sapphire taper [1]: a fibre was pre-tapered to micrometer-diameter and then broken and wrapped on the tip of the sapphire taper. The sapphire taper is heated with a C_2H_2 torch with a nozzle of about 6 mm in diameter; the task of the sapphire taper is to convey heat from the flame to the silica microwire in a controlled way. The softened silica wire is drawn in a direction perpendicular to the sapphire taper. **b**, Magnified view of the drawing process. The sapphire taper ensures that the temperature distribution in the drawing region remains steady while the silica wire is being drawn.

The second technique was developed by M. Sumetsky at OFS Inc. [2] and involves inserting an optical fibre into a sapphire capillary tube (microfurnace), which is heated by a CO_2 laser beam, as shown in Fig 2.2.

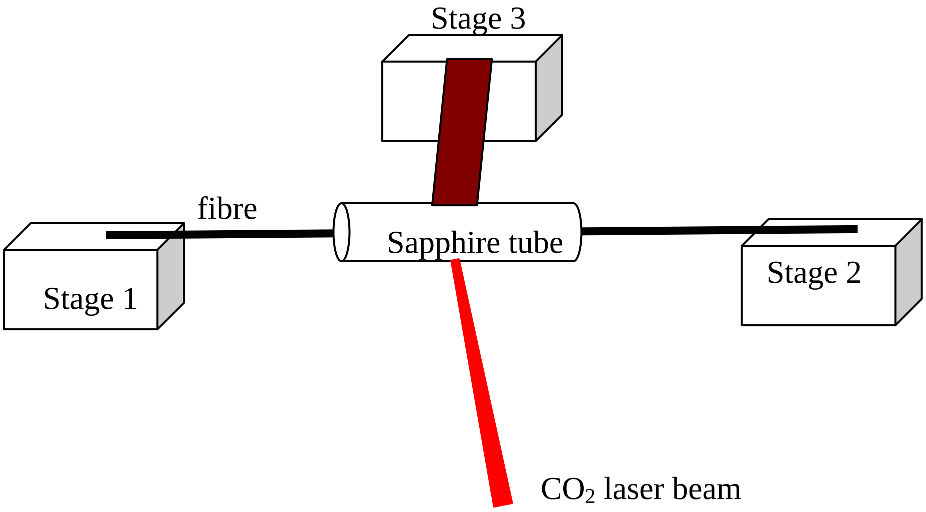

Fig. 2.2: Illustration of the setup for drawing NMOF using a sapphire tube heated with a CO_2 laser [2].

The beam size along the tube is controlled by moving the focal point of the lens. The various parts of the set-up are mounted on stages and the relative motion can be controlled by a computer. The final profile can be tailored to a given desired shape. This method is very fast and provides nanowires with very short tapers. Drawbacks of this process include high loss (0.1 dB/mm) and the short length of the drawn nanowires.

The third method is the so-called "flame-brushing technique", which was developed for the manufacture of conventional fibre tapers and couplers and it is based on a small flame moving under an optical fibre which is being stretched [3-5]. The control of the flame movement and the fibre tension can be used to define the taper shape to an extremely high degree of accuracy. Nanowires with radii as small as 30 nm have been demonstrated [6]. This methodology provides the longest and most uniform nanowires [5] with the lowest measured loss to date (0.001 dB/mm) [7, 8]. Moreover, it provides access to the nanowires from both the pigtailed ends, unlike other nanowires. This method was used in our research and will be discussed in more detail in Section 2.2.

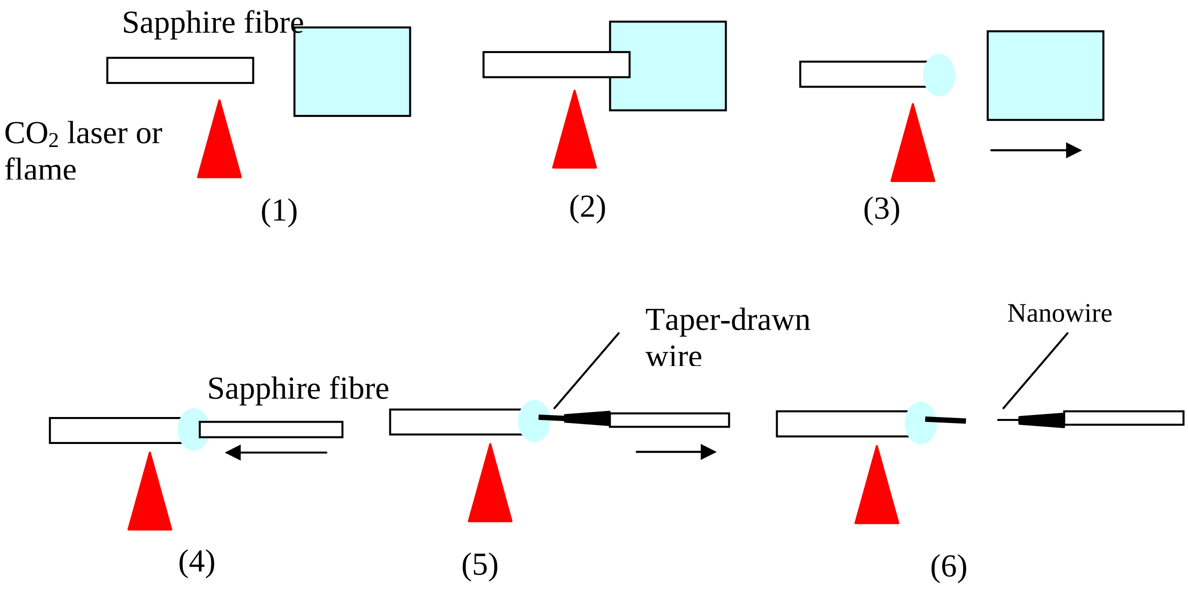

Fig. 2.3: Schematic diagram illustrating the direct draw of nanowires from bulk glasses. (1) A glass is moved towards a sapphire fibre heated by a CO$_2$ laser or flame. (2) The fibre end is immersed into the glass through local melting. (3) A portion of molten glass is left on the end of the fibre when the glass is withdrawn. (4) A second sapphire fibre is brought into contact with the molten-glass-coated end of the first sapphire fibre. (5) The heating power is reduced and the second sapphire fibre is withdrawn. (6) A nanowire is formed at the freestanding side of the taper drawn wire[9].

The fourth method is a direct drawing technique from bulk glass [9], as shown in Fig. 2.3. A sapphire fibre is heated and put in contact with a bulk glass. A small amount of the bulk glass melt and is removed on the sapphire fibre. The nanowire is then drawn placing another sapphire fibre in contact with the molten glass and then pulling the two sapphire fibres apart. Although the fabrication methodology is simple, the reproducibility and uniformity are not great. The typical loss is 0.1 dB/mm.

2.2 The Flame Brushing Technique

The flame brushing technique is the process most commonly used to manufacture couplers and tapers for optical fibre devices. Fig. 2.4 shows a simplified diagram of the “Flame Brushing” fabrication set-up: a millimeter sized flame heats a small fraction of fibre which is pulled by two translation stages. The small flame is scanned along the fibre over lengths of several tens of mm to produce tapers with an extremely uniform waist diameter and taper transitions of well defined length and shape [4]. The control of the flame movement and fibre stretch can control the taper shape to an extremely high degree of accuracy. This method provides the longest (~110 mm) and most uniform nanowires [5] with the lowest measured loss (~10^{-3} dB/mm) [7, 8].

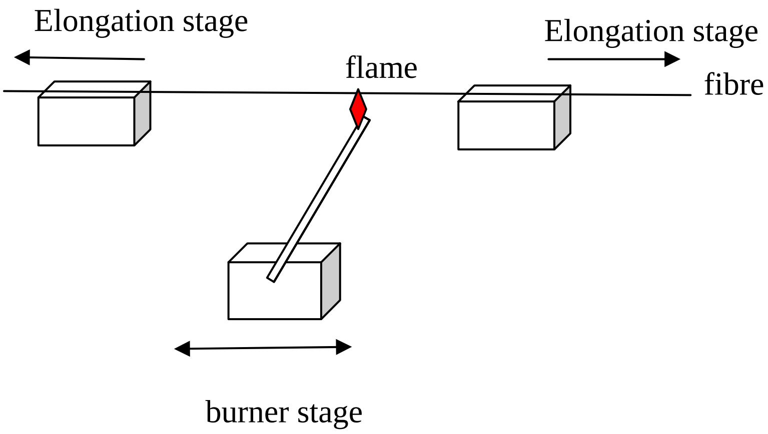

Fig. 2.4: Schematic of the flame brushing manufacturing rig.

At the ORC, a modified version of the flame brushing technique was developed replacing the flame with a microheater to work at lower temperatures and handle low-softening-temperature glasses, as shown in Fig. 2.5. The microheater is manufactured by NTT-AT from Japan. The whole fabrication rig is enclosed in a Perspex box to avoid air turbulence.

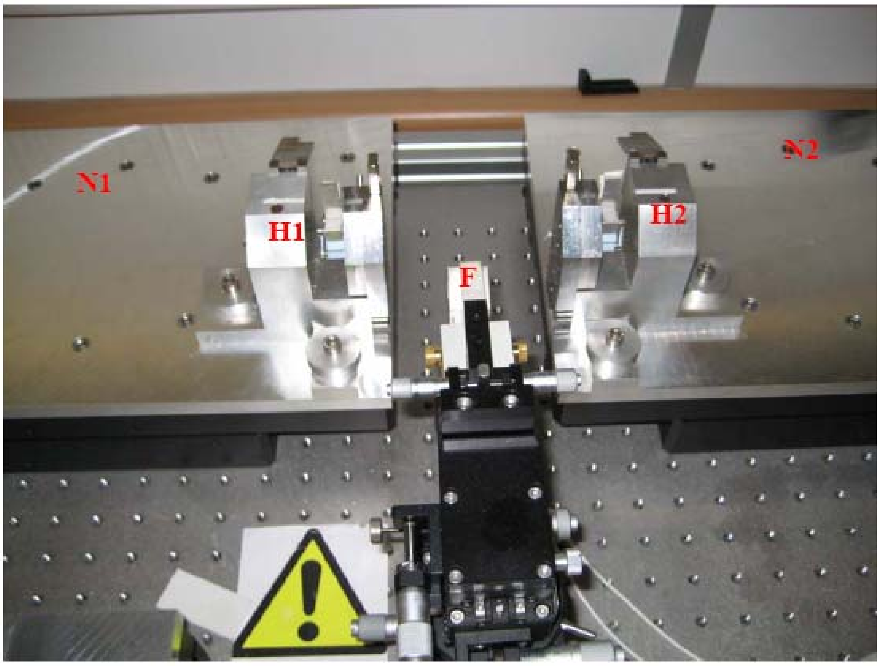

Fig. 2.5: Picture of our experimental set-up with a microheater. N1 and N2 are the translation stages, H1 and H2 are the fibre holders, F is the microheater.

Fig. 2.6 shows an example of the waist of a tapered fibre created from a 125 µm-diameter standard single mode fibre. The waist is ~5 µm; the waist length is ~3 mm.

Fig. 2.6: Picture of a tapered fibre from the standard single mode fibre.

2.3 Manufacture of Fibre Tips by Pipette Puller

Having discussed the fabrication of fibre tapers, now the fabrication of fibre tips is discussed. A fibre tip is an optical micro-component sculpted on the end of an optical fibre. Fibre tips have a number of medical and industrial applications. A tapered fibre tip is a type of tip with a continuously decreasing diameter at one end. There are several methods to manufacture tapered fibre tips:

The first method is to cut a fibre taper, but it is difficult to get very sharp tip.

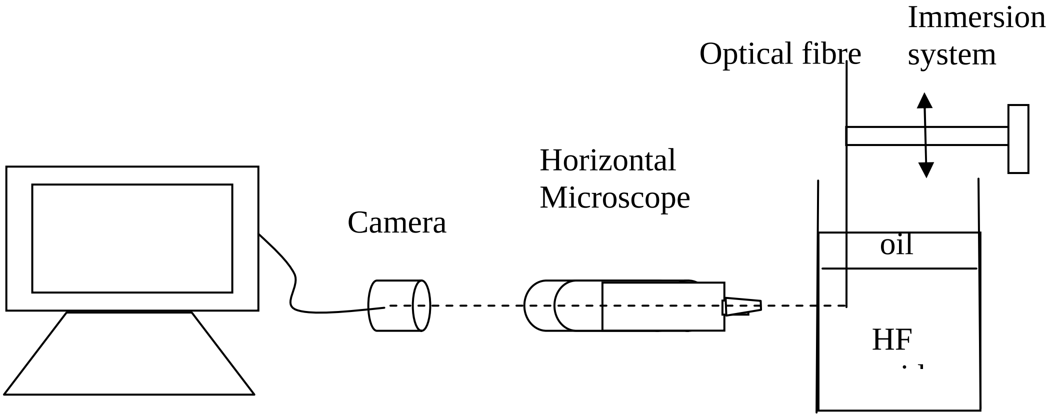

Fig. 2.7: Experimental set-up for etching [10].

The second method is to do it via chemical etching as shown in Fig. 2.7. The fibre is inserted into HF solution in a controlled way by the immersion system. The end of the fibre is watched using a microscope, a camera and a computer during etching. The procedure is time and energy consuming [10].

The quickest and simplest way to manufacture fibre tip relies on using a commercially available pipette puller. But the reproducibility is poor. This method is often used to manufacture fibre tips for optical sneezers and scanning near-field optical microscopy (SNOM) tips and will be discussed in details. It will be used in Chapter 4.

In this research, a commercially available pipette puller (P-2000) was used to manufacture very short sharp fibre tips. The P-2000 is a microprocessorcontrolled CO_2 laser-based micropipette puller as shown in Fig. 2.8. The bare fibre is held on two puller stages. The default configuration of the P-2000 allows the fabrication of micropipettes for intracellular recording, patch-clamping, microinjection and microperfusion. The primary advantage of using the CO_2 laser as a heat source is the ability to work with fused silica glass, a much stronger and more pure glass formulation than standard glass capillary tubing. The P-2000 can also be used to pull tubing and optical fibres to exceedingly small diameters for research applications such as SNOM.

The pipette puller has five following parameters which can be adjusted to achieve the wanted profile [11]:

- **HEAT** Range: 0 to 999. HEAT specifies the output power of the laser, and consequently the amount of energy supplied to the glass.

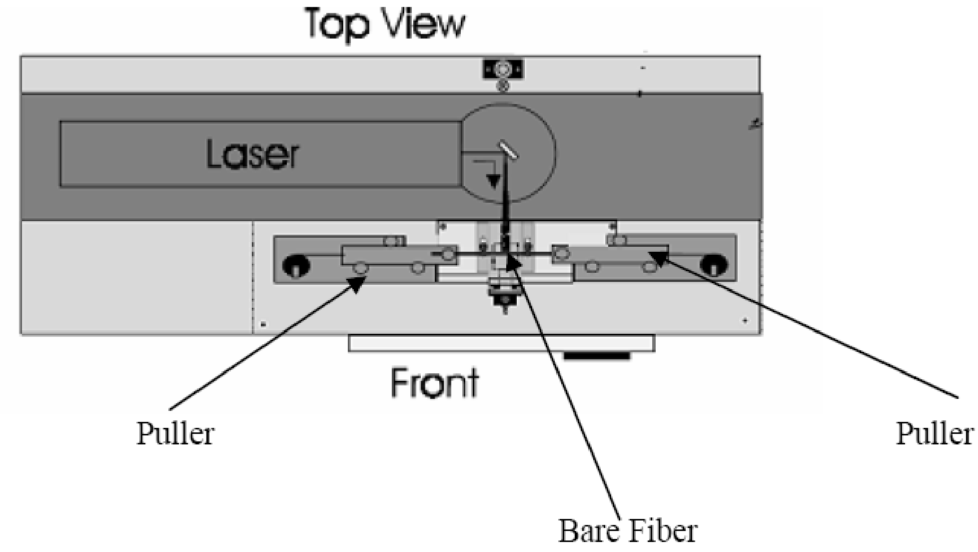

Fig. 2.8: Top view of P-2000[11].

- **FILAMENT** Range: 0 to 15. FILAMENT (FIL) specifies the scanning pattern of the laser beam that is used to supply HEAT to the glass. The P-2000 is pre-programmed with 16 different scanning patterns, each of which defines the longitudinal length and the rate of the scan. FILAMENTS also define the distribution of heat within the scanning length.

- **VELOCITY** Range: 0 to 255. The VELOCITY (VEL) parameter specifies the velocity at which the glass carriage must be moving before the hard pull is executed. The velocity of the glass carriages during the initial pull is dependent on the viscosity of the glass and the viscosity of the glass is dependent on its temperature. The velocity of the glass carriages, then, is an indirect way of measuring the glass temperature.

- **DELAY** Range: 0 to 255. The DELAY (DEL) parameter controls the timing of the start of the hard pull relative to the deactivation of the laser.

- **PULL** Range: 0 to 255. The PULL parameter controls the force of the hard pull.

The main problem of the P-2000 is the reproducibility; it is very difficult to obtain the same tip even when the same parameters are used. The setup is sensitive to the surrounding environment and to the position of the bare fibre. Yet, it is a very efficient method to fabricate short sharp fibre tips.

As an example, Fig. 2.9 shows the picture of a fibre tip fabricated using the P-2000. The tip end is less than 2μm, and it is very sharp. The parameters for fabrication were: HEAT=410; FILAMENT=0; VELOCITY=25; DELAY=115; PULL=60;

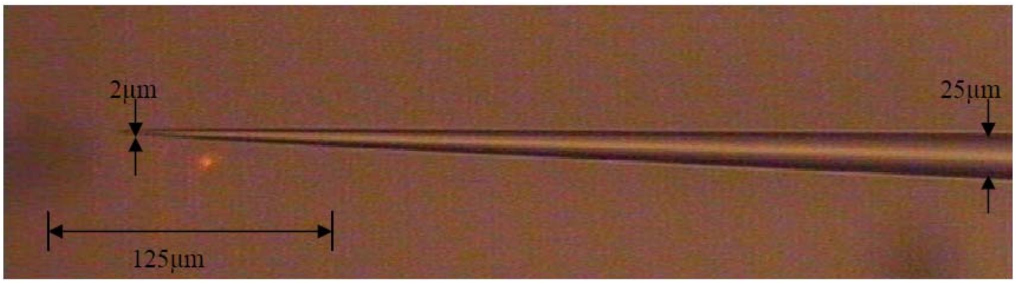

Fig. 2.9: Picture of a tapered fibre tip by P-2000.

2.4 The Shape of Fibre Taper

Before designing and manufacturing tapers using the flame brushing technique, it is necessary to understand how the flame brushing movement effects the fibre taper shape [4]. The aim of the section is to introduce the theory on the shape of fibre tapers [4] and describe how a desired taper profile *r*(z) can be produced by designing *L*(*t*) (which is the scanned length by the flame) and *x*(*t*) (the elongated length of the fibre at time *t*). Fig. 2.10 illustrates the quantities used to describe the shape of a complete fibre taper.

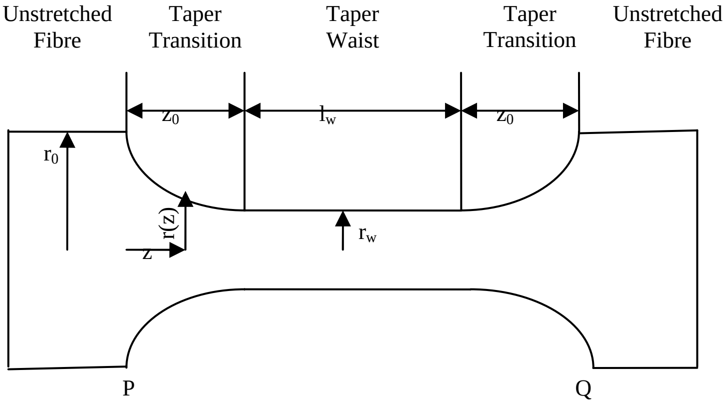

Fig. 2.10: The structure of a fibre taper.

There are some assumptions about the taper geometry: the taper is supposed to be formed symmetrically (i.e., the ends of the taper are pulled apart at equal and opposite speeds relative to the centre of the heat source) so that the two taper transitions are identical; the volume of the taper is assumed to be constant during tapering; the cross-section is assumed to be circular; the waist is assumed to be uniform and the diameter change is supposed unidirectional (constant decrease or constant increase).

The radius of the untapered fibre is r_0, and the uniform taper waist has length l_w and radius r_w. Each identical taper transition has a length z_0, and a shape described by a decreasing local radius function $r(z)$, where z is the longitudinal coordinate. The origin of z is at the beginning of each taper transition (point *P* for the representative left-hand transition in Fig. 2.10); hence $r(0) = r_0$, and $r(z_0) = r_w$,. In this section, the design of a desired taper profile $r(z)$ is discussed; the goal is to find a relation between the speed $v(t)$ of the translation stages and the taper profile $r(z)$, where t is the time.

The taper extension x is the amount of stretch which the taper has experienced, equal to the distance PQ (at time t) minus the distance PQ before tapering (time t=0), as shown in Fig.2.11. L is the length of taper waist (the heated hot-zone AB at time t), while L_0 is the length of hot-zone at time t=0. Simple mathematical considerations allow to deduce a “distance law” from the length of PQ at time t=0 and time t[4],

Time t=0 $\quad$ PQ=L_0

Time t $\quad PQ = x + L_0 = 2z_0 + L \qquad$ (2.4.1)

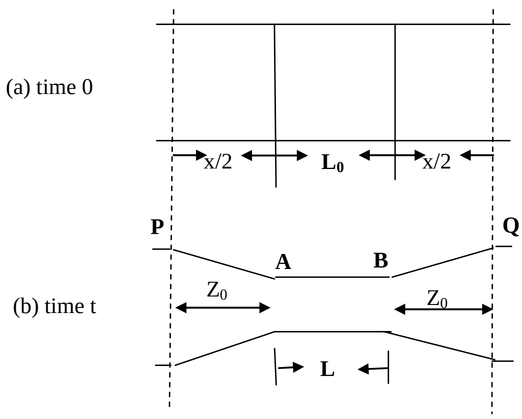

Fig. 2.11: (a) A fibre at time t=0 at initial status of tapering. A section PQ of length L_0 is heated. (b) The fibre at time t during tapering, PQ is extended x and also equal to $2z_0+L$ [4].

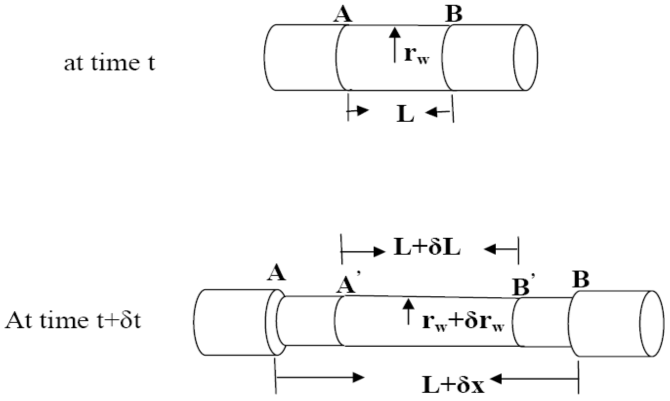

Fig. 2.12: Schematic diagrams [4] of a cylindrical taper waist at time t and $t+\delta t$. A part of AB is uniformly heated at time t; and the same glass elements at a slightly later time $t+\delta t$, AB has been stretched through a distance δx to form a narrower cylindrical taper waist, a part $A'B'$ of which is still heated.

As shown in Fig. 2.12, at any instant t during the taper elongation, a symmetrically placed length L of the taper waist is uniformly heated and is a deformable cylinder of low viscosity glass. The particular temperature and viscosity values are not important, though the hot glass is assumed always to be soft enough to be stretched, while not being so soft that the taper sags under its own weight. Outside the hot-zone the glass is cold and solid. The ends of the taper are steadily pulled apart, so that at time $t + dt$ the hot glass cylinder stretches to form a narrower cylinder of length $L + dx$, where dx is the increase in extension during the interval dt . The hot-zone A'B' length is changed to $L + dL$ in the same time. As the taper is also elongated, the extremities of the stretched heated cylinder leave the hot-zone and solidify, forming new elements of the taper transitions.

Mathematically, the relationship between the shape of the tapered fibre (expressed by r_w, l_w, r(z), and z_0) and the elongation conditions which produce it (expressed by $L(x)$, and x_0) is entirely determined by 3 equations [4]:

The first equation is the distance law Eq. (2.4.1).

Secondly, it is reasonable to assume that the instantaneous length l_w, of the taper waist at time t is equal to the hot-zone length at that time[4]

$$l_w(t) = L(t) \tag{2.4.2}$$

And $L_0=L(0)$ is defined as the hot-zone length at the begin of tapering.

Mass conservation implies that the volume of the fibre does not change during the tapering, the volume of cylinder AB at time $t+\delta t$ must equal the volume of the heated glass cylinder AB at time t and so [4]

$$\pi(r_w + \delta r_w)^2 (L + \delta x) = \pi r_w^2 L \tag{2.4.3}$$

Then,

$$r_w^2 L + 2r_w \delta r_w L + r_w^2 \delta x + (\delta r_w)^2 (L + \delta x) + 2r_w \delta r_w \delta x = r_w^2 L \tag{2.4.4}$$

So the third equation (called the "volume law") can be obtained, ignoring the high order items $(\delta r_w)^2 (L + \delta x) + \delta r_w \delta x$ on the left [4]:

$$\frac{dr_w}{r_w} = -\frac{dx}{2L} \tag{2.4.5}$$

Theoretically, Eqs. (2.4.1)-(2.4.4) provide a procedure by which any taper shape can be made. For example, a desired taper shape (defined by l_w, r_w,z_0, and $r(z)$, where $r(0)=r_0$ and $r(z_0)=r_w$) is known, and $L(x)$ and the final extension x_0 are required. The volume law can be arranged to give[4]

$$\frac{dr}{dx} = -\frac{r}{2L} \tag{2.4.6}$$

From Eq.(2.4.4) and (2.4.6), a first-order linear differential equation for L as a function of r, with dz/dr a known function since $r(z)$ is known, can be given [4]

$$\frac{dL}{dr} + \frac{2}{r}L + 2\frac{dz}{dr} = 0 \tag{2.4.7}$$

With initial conditions $r=r_0$ and $L=L_0$ for $z=0$, this equation integrates to[4]

$$L(z) = \frac{r_0^2}{r^2}L_0 - \frac{2}{r^2}\int_{r_0}^{r} r^2 \frac{dz}{dr}dr \tag{2.4.8}$$

i.e.,

$$L(z) = \frac{r_0^2}{r^2}L_0 - \frac{2}{r^2(z)}\int_0^{z} r^2(z')dz' \tag{2.4.9}$$

Where $L(z)$ is the hot-zone length as point z was pulled out of the hot-zone. L_0 is as yet unknown, but can be determined by evaluating Eq. (2.4.8) at $z=z_0$, since $L(z_0)=l_w$ is given,

$$l_{\omega} = L_0 - \frac{2}{r_0^2}\int_0^{z_0} r^2(z')dz' \tag{2.4.10}$$

hence Eq. (2.4.9) becomes[4]

$$L(z) = \frac{r_w^2}{r^2(z)} l_w + \frac{2}{r^2(z)} \int_z^{z_0} r^2(z^{'}) dz^{'} \qquad (2.4.11)$$

The distance law gives x as a known function of z [4]

$$x(z) = 2z + L(z) - L_0 \qquad (2.4.12)$$

The function $L(x)$ can be determined. In fact, x is the function of time $x(t)$ which describes the movement of stages at time t, $L(x(t))$ is the hot-zone length at time t. If $x(t)$ is chose , $L(t)$ is known.

2.5 Summary

In this chapter, we reviewed the different methods of manufacturing fibre tapers and tips. As major methods in our research, the flame brush technique and pipette puller are introduced in details. The theory of fibre taper shape was also reviewed.

2.6 References

1. L. M. Tong, R. R. Gattass, J. B. Ashcom, S. L. He, J. Y. Lou, M. Y. Shen, I. Maxwell, and E. Mazur, "Subwavelength-diameter silica wires for low-loss optical wave guiding," Nature **426**, 816-819 (2003).
2. M. Sumetsky, Y. Dulashko, and A. Hale, "Fabrication and study of bent and coiled free silica nanowires: Self-coupling microloop optical interferometer," Optics Express **12**, 3521-3531 (2004).
3. F. Bilodeau, K. O. Hill, S. Faucher, and D. C. Johnson, "Low-Loss Highly Overcoupled Fused Couplers - Fabrication and Sensitivity to External-Pressure," Journal of Lightwave Technology **6**, 1476-1482 (1988).
4. T. A. Birks, and Y. W. Li, "The Shape of Fiber Tapers," Journal of Lightwave Technology **10**, 432-438 (1992).

5. G. Brambilla, V. Finazzi, and D. J. Richardson, "Ultra-low-loss optical fiber nanotapers," Optics Express **12**, 2258-2263 (2004).

6. G. Brambilla, F. Xu, and X. Feng, "Fabrication of optical fibre nanowires and their optical and mechanical characterisation," Electronics Letters **42**, 517-519 (2006).

7. S. G. Leon-Saval, T. A. Birks, W. J. Wadsworth, P. S. J. Russell, and M. W. Mason, "Supercontinuum generation in submicron fibre waveguides," Optics Express **12**, 2864-2869 (2004).

8. A. M. Clohessy, N. Healy, D. F. Murphy, and C. D. Hussey, "Short low-loss nanowire tapers on singlemode fibres," Electronics Letters **41**, 954-955 (2005).

9. L. Tong, L. Hu, J. Zhang, J. Qiu, Q. Yang, J. Lou, Y. Shen, J. He, and Z. Ye, "Photonic nanowires directly drawn from bulk glasses," Optics Express **14**, 82-87 (2006).

10. N. E. Demagh, A. Guessoum, and H. Aissat, "Chemical etching of concave cone fibre ends for core fibre alignment," Measurement Science & Technology **17**, 119-122 (2006).

11. "Manual of P-2000." Sutter Instrument Company, U.S.A. http://www.sutter.com

Chapter 3

Theoretical Characteristics of Fibre Taper Nanowires

Understanding the electromagnetic wave propagation in optical fibre nanowires is necessary to design optical fibre nanowire devices. In this chapter, the fundamental properties of tapered fibres are obtained by solving Maxwell's equations; some basic modal and bend characteristics and dispersion are then discussed. In particular, in Section 3.1, the waveguide theory is discussed, including two-layer and three-layer models of fibre tapers; in Section 3.2, the mode and bend characteristics of nanowires are calculated.

3.1 Basic Waveguide Theory of Fibre Tapers

Like all electromagnetic phenomena, the propagation of light in an optical fibre is governed by Maxwell's Equations. In a linear isotropic, non-magnetic, homogeneous medium without free charges, these equations are written in terms of the electric field **e** and magnetic field **h** as[1]

$$\begin{cases} \nabla \times \mathbf{e} = -\mu \dfrac{\partial \mathbf{h}}{\partial t} \\ \nabla \times \mathbf{h} = \varepsilon \dfrac{\partial \mathbf{e}}{\partial t} \\ \nabla \cdot \mathbf{e} = \mathbf{0} \\ \nabla \cdot \mathbf{h} = \mathbf{0} \end{cases} \tag{3.1.1}$$

Where ε and μ denote the permittivity and permeability of the medium, respectively, ε and μ are related to their respective values in a vacuum (ε_0=8.854×10 $^{-12}$[F/m] and μ_0=4π×10^{-7}[F/m]) by

$$\begin{cases} \varepsilon = \varepsilon_0 n^2 \\ \mu = \mu_0 \end{cases} \tag{3.1.2}$$

where n is the refractive index.

In this thesis, common single mode fibres and tapers are discussed. A schematic of the waveguide structure of these fibres, without coating, is shown in Fig. 3.1. It is a three layer waveguide: core, cladding and air, with refractive indices n_1, n_2, and n_3 (n_3=1 for air), respectively and $n_1>n_2>n_3$. Optical nanowires, drawn from standard single mode fibres, have the same structure but different diameters. To describe a position along the fibre, cylindrical coordinates (z,ρ,θ) are used; r_1 and r_2 are the core and cladding radii, respectively.

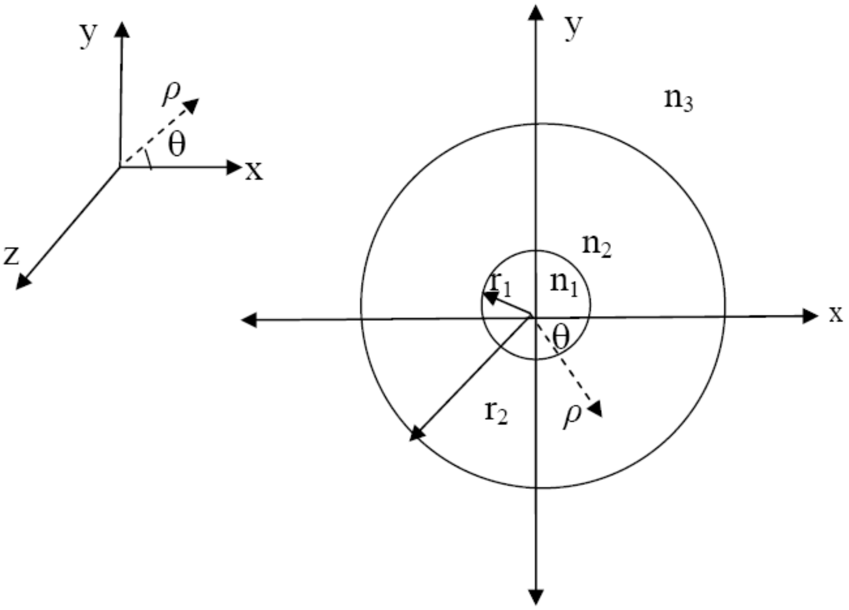

Fig. 3.1: Local cross section of a step-index fibre

Like all waveguide problems light propagation in optical fibres is described in term of modes. An optical mode refers to the pattern of light which is invariant along the propagation direction. When we consider light having angular frequency ω and propagating in the z direction, the electromagnetic mode field **e** and **h** can be expressed in cylindrical coordinates as

$$\mathbf{e} = \overline{E}(\rho,\theta)e^{j(\omega t-\beta z)} \tag{3.1.3}$$

$$\mathbf{h} = \overline{H}(\rho,\theta)e^{j(\omega t-\beta z)} \tag{3.1.4}$$

where β is the propagation constant.

If the frequency of the electromagnetic wave is f (=ω/2π) [Hz], the wavelength in vacuum is obtained by

$$\lambda = \frac{c}{f} \tag{3.1.5}$$

Note that the wavenumber k in vacuum is related to the angular frequency ω by

$$k = \omega\sqrt{\varepsilon_0\mu_0} = \frac{\omega}{c} = \frac{2\pi}{\lambda} \tag{3.1.6}$$

where c is the light velocity in a vacuum, given by $c=2.998\times10^8$[m/s]. The effective index of the mode can be defined as $n_{eff} = \frac{\beta}{k}$. For modes in tapers, the mode is classified as a cladding mode for $n_2>n_{eff}>n_3$, and as a core mode for $n_{eff}>n_2$.

For theoretical design and practical applications of optical fibre tapers and related devices, it is very important to calculate the mode properties, effective refractive index and dispersion; this requires solving the set of vectorial Maxwell's equations for the given local index profile.

In this research, only light with wavelengths from several hundred of nanometres to several micrometers is considered. When the cladding diameter is large ($r_2>>r_1$ and $r_2>>\lambda$), the mode is confined near the core, the cladding can be assumed to be infinite and the fibre can be simplified as two layer model. For smaller cladding diameters, the mode is no longer confined near the core and the fibre should be taken as a three layer waveguide with a finite cladding.

Substituting Eqs. (3.1.3) and (3.1.4) into Maxwell equations (3.1.1), two equations for the longitudinal component of the mode can be obtained [2]

$$\begin{cases} \dfrac{\partial^2 E_z}{\partial \rho^2}+\dfrac{1}{\rho}\dfrac{\partial E_z}{\partial \rho}+\dfrac{1}{\rho}\dfrac{\partial^2 E_z}{\partial \theta^2}+[k^2 n^2(\rho,\theta)-\beta^2]E_z=0 \\ \dfrac{\partial^2 H_z}{\partial \rho^2}+\dfrac{1}{\rho}\dfrac{\partial H_z}{\partial \rho}+\dfrac{1}{\rho}\dfrac{\partial^2 H_z}{\partial \theta^2}+[k^2 n^2(\rho,\theta)-\beta^2]H_z=0 \end{cases} \tag{3.1.7}$$

where $n(\rho,\theta)$ is the refractive index.

The transverse components of the electromagnetic fields are related to E_z and H_z as follows:

$$\begin{cases} E_\rho=\dfrac{j}{[k^2 n^2(\rho)-\beta^2]}(\beta\dfrac{\partial E_z}{\partial \rho}+\dfrac{\omega\mu_0}{\rho}\dfrac{\partial H_z}{\partial \theta}) \\ E_\theta=\dfrac{j}{[k^2 n^2(\rho)-\beta^2]}(\dfrac{\beta}{r}\dfrac{\partial E_z}{\partial \theta}-\omega\mu_0\dfrac{\partial H_z}{\partial \rho}) \\ H_\rho=\dfrac{j}{[k^2 n^2(\rho)-\beta^2]}(\beta\dfrac{\partial H_z}{\partial \rho}+\dfrac{\omega\varepsilon_0 n^2(\rho)}{\rho}\dfrac{\partial E_z}{\partial \theta}) \\ H_\theta=\dfrac{j}{[k^2 n^2(\rho)-\beta^2]}(\dfrac{\beta}{\rho}\dfrac{\partial H_z}{\partial \theta}+\omega\varepsilon_0 n^2(\rho)\dfrac{\partial E_z}{\partial \rho}) \end{cases} \tag{3.1.8}$$

For the three layers circular symmetric structure, $n(\rho)$ is given by:

$$n(\rho)=\begin{cases} n_1 & when\quad 0<\rho<r_1 \\ n_2 & when\quad r_1<\rho<r_2 \\ n_3 & when\quad r_2<\rho \end{cases} \tag{3.1.9}$$

Modes correspond to the solutions of Eq. (3.1.7) and the appropriate boundary conditions [the continuity of E_z (H_z) and $\dfrac{dE_z}{d\rho}$ ($\dfrac{dH_z}{d\rho}$)], and can be classified as either TE modes (E_z=0), TM modes (H_z=0), or hybrid modes ($E_z\neq$0, $H_z\neq$0), respectively.

The solutions of Eqs. (3.1.7) and (3.1.8) in each region of the fibre depend on the magnitude of n_{eff} with respect to the refractive index n. If $n_{eff}<n$, the two independent solutions are the v^{th}-order Bessel functions of the first and second kinds J_v and Y_v(where ν is integer), while if $n_{eff}> n$, the two independent solutions are the v^{th}-order modified Bessel functions of the first and second kinds I_v, and K_v, respectively.

In the core, $n_{eff}< n_1$ and the solution is

$$\begin{Bmatrix} E_z \\ H_z \end{Bmatrix} = \begin{Bmatrix} A \\ A' \end{Bmatrix} J_n(U\frac{\rho}{r_1}) \begin{bmatrix} \cos(v\theta) \\ \sin(v\theta) \end{bmatrix} \tag{3.1.10}$$

In the cladding, if $n_2<n_{eff}< n_1$, then

$$\begin{Bmatrix} E_z \\ H_z \end{Bmatrix} = [\begin{Bmatrix} B \\ B' \end{Bmatrix} I_v(W\frac{\rho}{r_1}) + \begin{Bmatrix} C \\ C' \end{Bmatrix} K_v(W\frac{\rho}{r_1})] \begin{bmatrix} \cos(v\theta) \\ \sin(v\theta) \end{bmatrix} \tag{3.1.11}$$

if $n_3<n_{efff}< n_2$:

$$\begin{Bmatrix} E_z \\ H_z \end{Bmatrix} = [\begin{Bmatrix} B \\ B' \end{Bmatrix} J_v(Q\frac{\rho}{r_1}) + \begin{Bmatrix} C \\ C' \end{Bmatrix} Y_v(Q\frac{\rho}{r_1})] \begin{bmatrix} \cos(v\theta) \\ \sin(v\theta) \end{bmatrix} \tag{3.1.12}$$

In the air, $n_3<n_{efff}$, the solution is

$$\begin{Bmatrix} E_z \\ H_z \end{Bmatrix} = \begin{Bmatrix} D \\ D' \end{Bmatrix} K_n(T\frac{\rho}{r_1}) \begin{bmatrix} \cos(v\theta) \\ \sin(v\theta) \end{bmatrix} \tag{3.1.13}$$

where the fibre parameters and normalised modal parameters *V, U, Q, W* and *T* for the three regions of the fibre, i.e. core, cladding and air, are defined by [3]

$$\begin{cases} V = r_1 k(n_1 - n_2)^{1/2} \\ U = r_1 k(n_1^2 - n_{eff}^2)^{1/2} \\ Q = r_1 k(n_2^2 - n_{eff}^2)^{1/2} \\ W = r_1 k(n_{eff}^2 - n_2^2)^{1/2} \\ T = r_1 k(n_{eff}^2 - n_3^2)^{1/2} \end{cases} \tag{3.1.14}$$

Where *A, A', B, B', C, C', D* and *D'* are constants. In order to find the propagation constants or effective indices, the continuity conditions at the core-cladding and cladding-air interfaces should be considered. J.D. Love presented some solutions in ref. 3. He considers the continuity of $E_z\,(H_z)$ and $\frac{dE_z}{d\rho}\,(\frac{dH_z}{d\rho})$ and sets $\boldsymbol{v}$=1 for the HE_{1m} modes, which leads to a set of homogeneous, linear equations which relate the values of *A-D* and provide an eigenvalue equation for β from the consistency condition. The algebraic form of the eigenvalue equation can be derived, but it is a transcendental equation for the propagation constant and must be solved numerically.

When the diameter of the taper is very small or the cladding is very large ($r_1 << \lambda$, $r_2 \sim \lambda$), the core can be ignored and a two-layer model applies:

$$n(\rho) = \begin{cases} n_1 \; 0 < \rho < r_1 \\ n_2 \; r_1 \leq \rho < \infty \end{cases} \tag{3.1.15}$$

In most cases the taper is in air and therefore $n_2=1$.

In this case, the eigenvalue equations obtained from Eqs. (3.1.7) and (3.1.8) for various modes are as follows:

for HE_{vm} and EH_{vm} modes[4] :

$$\left\{ \frac{J_v^{'}(U)}{UJ_v(U)} + \frac{K_v^{'}(W)}{WK_v(W)} \right\} \left\{ \frac{J_v^{'}}{UJ_v(U)} + \frac{n_2^2}{n_1^2} \frac{K_v^{'}(W)}{WK_v(W)} \right\} = \left(\frac{v\beta}{kn_1} \right)^2 \left(\frac{V}{UW} \right)^4 \tag{3.1.16}$$

for TE_{0m} modes[4]:

$$\frac{J_1(U)}{UJ_0(U)} + \frac{K_1(W)}{WK_0(W)} = 0 \tag{3.1.17}$$

for TM_{0m} modes[4]:

$$\frac{n_1^2 J_1(U)}{UJ_0(U)} + \frac{n_2^2 K_1(W)}{WK_0(W)} = 0 \tag{3.1.18}$$

In this thesis, only the fundamental mode [4] is considered;

for $0 < \rho < r_1$:

$$\begin{cases} E_\rho = -\dfrac{a_1 J_0(U\frac{\rho}{r_1}) + a_2 J_2(U\frac{\rho}{r_1})}{J_1(U)}\cos(v\theta) \\ E_\phi = -\dfrac{a_1 J_0(U\frac{\rho}{r_1}) - a_2 J_2(U\frac{\rho}{r_1})}{J_1(U)}\sin(v\theta) \\ E_z = -i\dfrac{UJ_1(U\frac{\rho}{r_1})}{J_1(U)}\cos(v\theta) \end{cases} \tag{3.1.19}$$

When $a \le r < \infty$

$$\begin{cases} E_\rho = -\dfrac{U}{W}\dfrac{a_1 K_0(W\frac{\rho}{r_1}) - a_2 K_2(W\frac{\rho}{r_1})}{K_1(W)}\cos(v\theta) \\ E_\phi = -\dfrac{U}{W}\dfrac{a_1 K_0(W\frac{\rho}{r_1}) + a_2 K_2(W\frac{\rho}{r_1})}{K_1(W)}\sin(v\theta) \\ E_z = -i\dfrac{UK_1(W\frac{\rho}{r_1})}{\alpha\beta K_1(W)}\cos(v\theta) \end{cases} \tag{3.1.20}$$

where

$$a_1 = \frac{F_2 - 1}{2},\ a_2 = \frac{F_2 + 1}{2},$$

$$F_1 = \left(\frac{UW}{V}\right)\left[b_1 + (1-2\Delta)b_2\right],\ F_2 = \left(\frac{UW}{V}\right)\frac{1}{b_1 + b_2},$$

$$b_1 = \frac{1}{2U}\left\{\frac{J_0(U)}{J_1(U)} - \frac{J_2(U)}{J_1(U)}\right\},\ b_2 = -\frac{1}{2W}\left\{\frac{K_0(U)}{K_1(U)} + \frac{K_2(U)}{K_1(U)}\right\}$$

As an example, Fig. 3.2 shows a schematic of the intensity profiles of E_x in the first two *HE* modes.

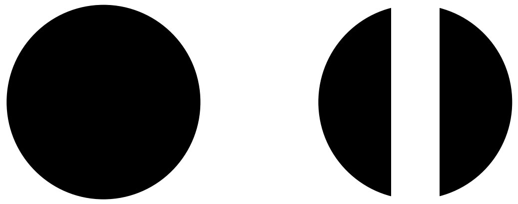

Fig. 3.2: Schematic of the intensity profiles of E_x in first two *HE* modes.

In practical applications it is important to know the profile of the power distribution across the waveguide. For the fibre mode considered here, the average energy flows in the radial (r) and azimuthal (θ) directions are zero, so we only consider the energy flow in z-direction. The z-components of Poynting vectors are obtained as

$$S_z = \frac{1}{2}(\overline{E} \times \overline{H^*}) \cdot \overline{u_z} = \frac{1}{2}(E_\rho H_\theta^* - E_\theta H_\rho^*) \qquad (3.1.21)$$

where u_z is a unit vector in the z-direction.

The power fraction carried in the optical core for the two-layer model can be defined as:

$$\eta = \frac{\int_0^{2\pi} \int_0^a S_z dA}{\int_0^{2\pi} \int_0^a S_z dA + \int_0^{2\pi} \int_a^\infty S_z dA} \qquad (3.1.22)$$

where $dA = rdrd\phi$,

As an example, the effective index in fibres with different diameters has been calculated by applying the Eqs. (3.1.12)-(3.1.15) to tapered standard telecom single mode fibres, which have a core diameter of 10μm, a cladding with diameter of 125 μm and index of 1.4443 and a numerical aperture (NA) of $\sqrt{n_{co}^2 - n_{cl}^2} = 0.11$ at 1550 nm. Here the ratio of cladding and core is a constant. The results for the first two *HE* modes are shown in Fig. 3.2(a).

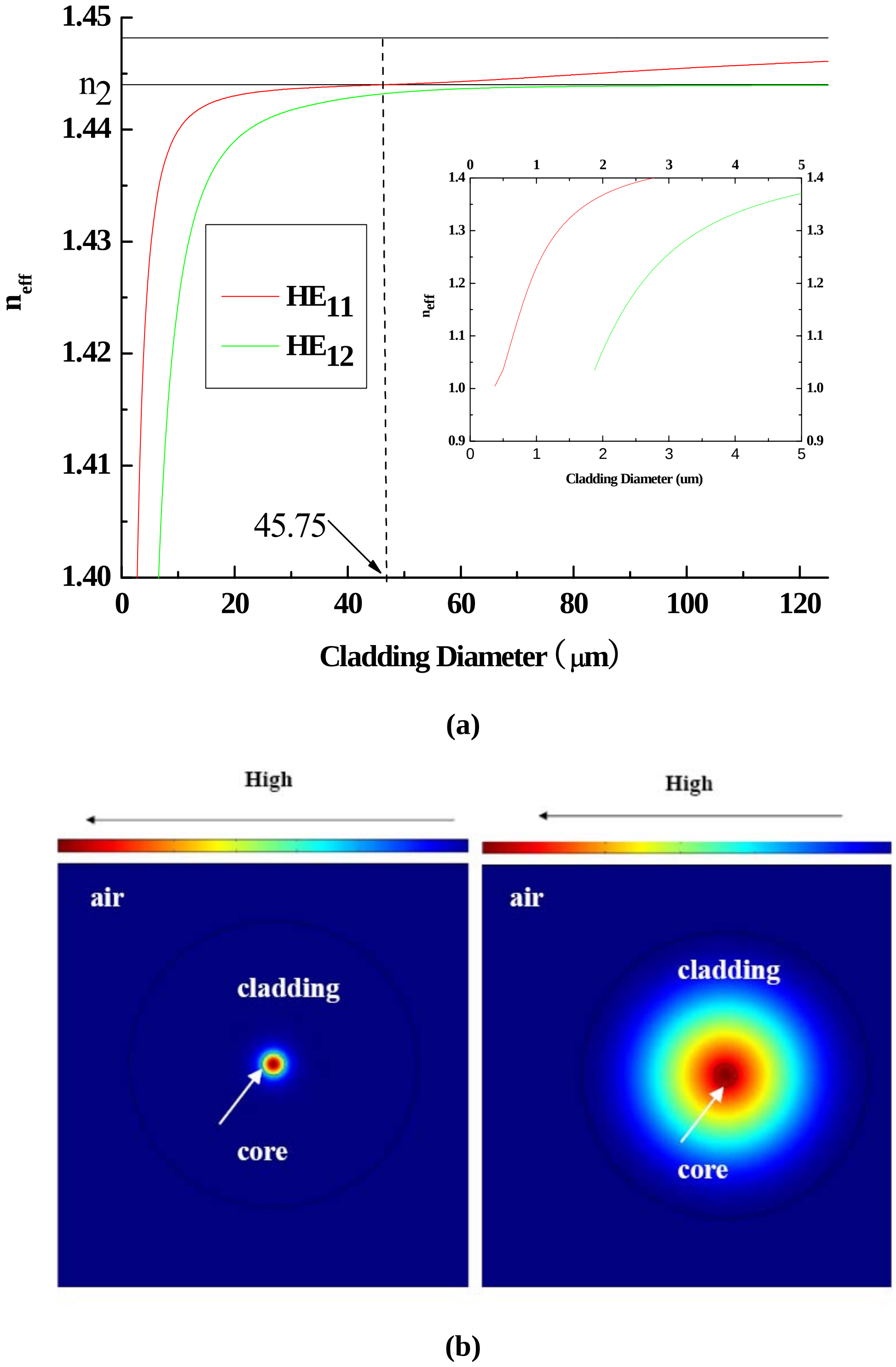

Fig. 3.3: (a) Effective index values for the first two *HE*$_{1m}$ modes propagating in a step-index profile fibre with finite cladding, as a function of the cladding diameter calculated according and the exact solution of Maxwell equations. (b) Intensity distribution of fundamental *HE*$_{11}$ modes at cladding diameter 80 μm (left) and at cladding diameter 20 μm (right).

It can be seen that, when the cladding diameter is above 45.75μm, there is a single mode operation in the core, while when the cladding diameter is below 45.75 μm the cladding mode dominates; there are no core modes. As an example, the mode profiles of HE_{11} at cladding diameter 80 μm and at cladding diameter 20 μm are shown on the left and right of Fig. 3.3(b), respectively.

In practical nanowires the waist is less than 10 μm, thus the fibre taper diameter in the transition regions has to cross the critical value 45.75 μm, where the propagating mode is not confined in the core but in the cladding. This point can be described as core mode cut-off point [5].

3.2 Mode Characteristics and Bend Loss Characteristics of Nanowire Drawn From Single-Mode-Fibre

Most common nanowires drawn from single-mode-fibres can be assumed as an air-cladding step-index fibre with the two layer model when the diameter d is very small (~1 μm). Here n_1=1.4443 at 1.55 μm wavelength for pure silica and n_2=1 for air. Here some of fundamental characteristics (i.e. effective index, fractional power and bend loss) are calculated for a microfibre.

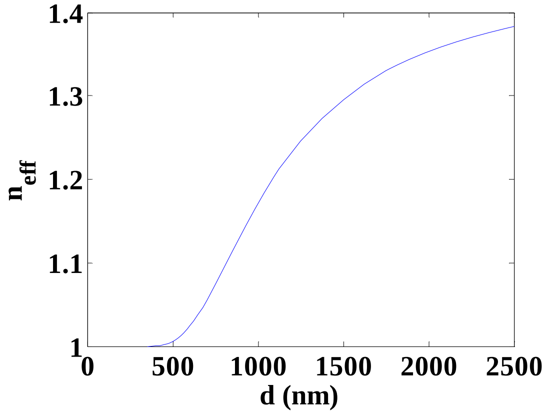

Fig. 3.4: Effective index as a function of diameter at 1.55 μm.

Fig 3.4 shows the calculated effective index of a step index fibre in air as a function of the diameter at wavelength of 1.55 μm. The effective index is nearly 1 when d<400 nm because most of the field is in air.

Fig 3.5 shows the fractional power η as a function of d: η is less than 5% when d<400 nm, while it is more than 90% when d>1500 nm.

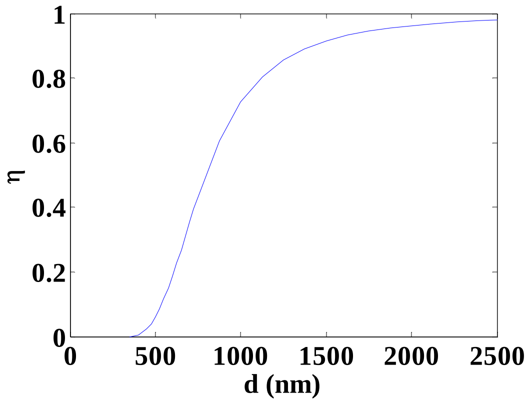

Fig. 3.5: Fraction of power in the core η as a function of the taper diameter d.

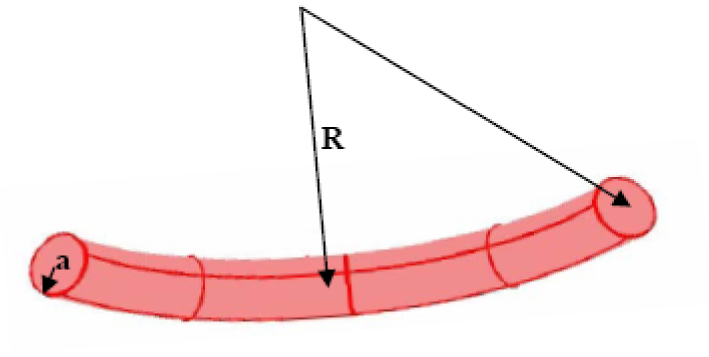

Fig. 3.6: Illustration of a piece of bend nanowire.

Since nanowires in many applications will be coiled, as, for example, in loop resonators or microcoil resonators, it is very important to investigate the bend loss α. The loss of the fundamental mode can be evaluated by the following formula [6]:

$$\alpha(\lambda) = \frac{U^2}{2V^2W^{1.5}K_1^2(W)}\left(\frac{\pi}{aR}\right)^{0.5}\exp\left[-\frac{4W^3}{3V^2}\left(1-\frac{n_1^2}{n_2^2}\right)\frac{R}{a}\right] \tag{3.2.1}$$

where V ,U , and W are defined as Eq. (3.1.11), R is the bend curvature radius and a is the fibre radius, as shown in Fig 3.6.

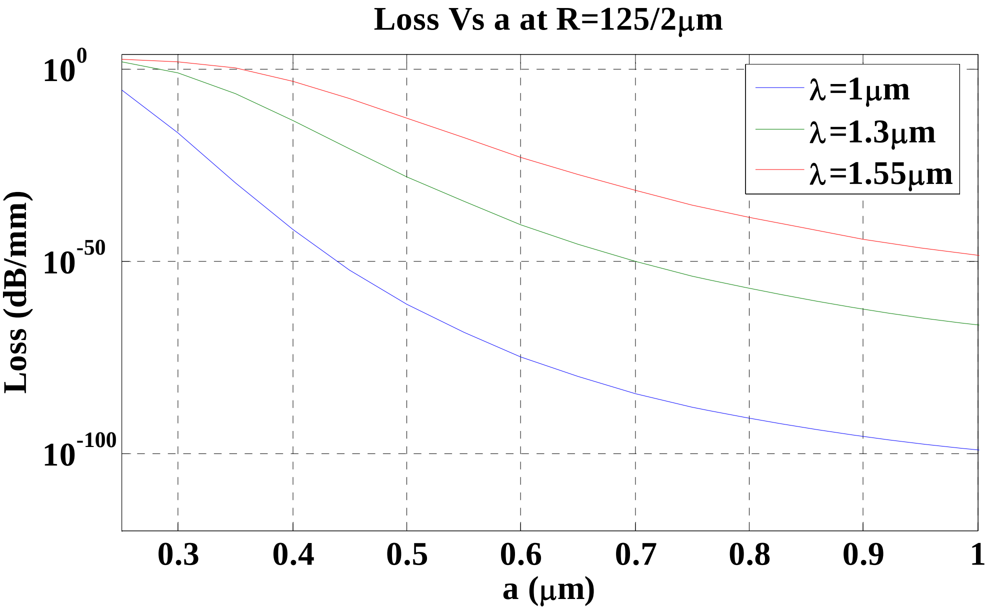

Fig. 3.7: Dependence of the nanowire bend loss on its radius *a* at three wavelengths (1 μm, 1.3 μm, and 1.55 μm).

As an example, Fig. 3.7 shows the dependence of the nanowire bend loss on its radius *a* at three wavelengths (1 μm, 1.3 μm, and 1.55 μm). The loss increases for increasing wavelengths and decreasing *a* for small radius nanowires (a<1 μm).

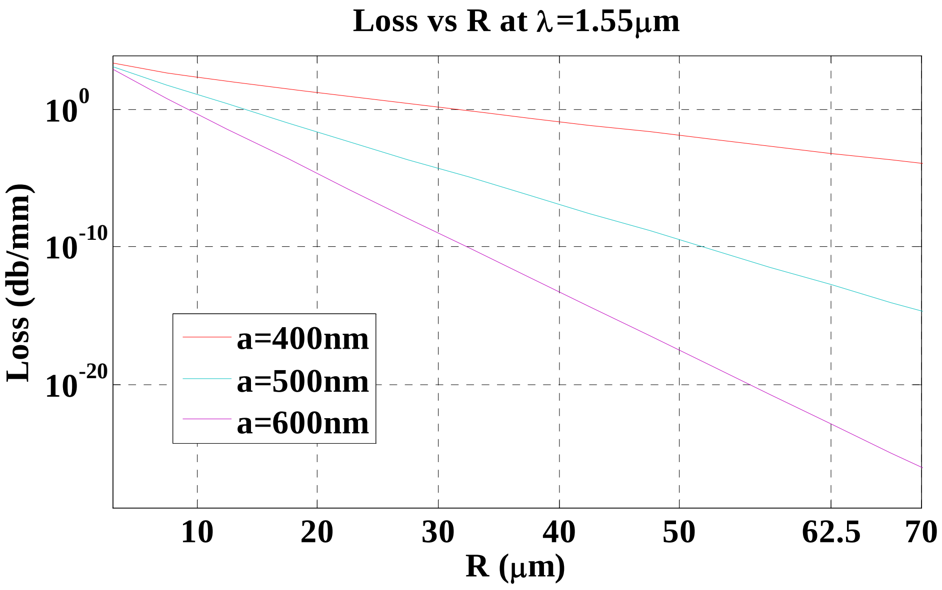

Fig. 3.8: Dependence of the nanowire bend loss on the bending radius R for three different nanowire radii *a*.

Fig. 3.8 shows the dependence of the nanowire bending loss on the curvature radius R for *a*=400 nm, 500 nm and 600 nm. It can be seen that the bend loss is insignificant for ~1μm-diameter-nanowires at R>50 μm and λ=1.55 μm, which is suitable for most practical nanowire resonators. Comparing the loss at R=62.5 μm and λ=1.550 μm, Figs.3.7 and 3.8 agree well.

3.3 Summary

In summary, the fundamental theory of tapered fibre was discussed; some important parameters were introduced and calculated. In the next chapter the adiabatic transition in optical fibre tapers will be discussed, with particular attention to its application in optical trapping.

3.4 References

1. G. P. Agrawal, *Fiber-optic communication systems* (Wiley-Interscience,

New York, 2002).

2. K. Okamoto, *Fundamentals of optical waveguides* (Elsevier, Amsterdam ; Boston, 2006).

3. J. D. Love, W. M. Henry, W. J. Stewart, R. J. Black, S. Lacroix, and F. Gonthier, "Tapered Single-Mode Fibers and Devices .1. Adiabaticity Criteria," IEE Proceedings-J Optoelectronics **138**, 343-354 (1991).

4. L. M. Tong, J. Y. Lou, and E. Mazur, "Single-mode guiding properties of subwavelength-diameter silica and silicon wire waveguides," Optics Express **12**, 1025-1035 (2004).

5. R. J. Black, and R. Bourbonnais, "Core-Mode Cutoff for Finite-Cladding Lightguides," IEE Proceedings-J Optoelectronics **133**, 377-384 (1986).

6. A. W. Snyder, and J. D. Love, *Optical waveguide theory* (Chapman and Hall, London ; New York, 1983).

Chapter 4

Loss of Optical Fibre Nanowires

In previous chapters the propagation characteristics of nanowires were introduced; in this chapter another very important characteristic is considered: i.e. loss. First, different loss mechanisms are discussed, next the loss of different–diameter nanowires is analysed; finally, a method to avoid unrecoverable loss by embedding the nanowire in a low index material is demonstrated.

4.1 Loss Mechanisms of Nanowires

Loss in optical fibres or in OFN is a major limiting factor, because it decreases device performance and reduces the signal power reaching the device output. Under quite general conditions, changes in the average optical power P of light propagating inside an optical fibre along the coordinate z are governed by Lambert-Beer's law [1]:

$$dP / dz = -\alpha P \tag{4.1.1}$$

where α is the attenuation coefficient.

If P_{in} is the power launched at the input end of a fibre of length L(mm), the output power P_{out} given by the solution of Eq. (4.1.1) is

$$P_{out} = P_{in} \exp(-\alpha L) \tag{4.1.2}$$

We express α in units of dB/mm by using the relationship

$$\alpha(\text{dB/mm}) = -\frac{10}{\text{L}}\log_{10}(\frac{P_{out}}{P_{in}}) \simeq 4.343\alpha\ (\text{mm}^{-1}) \tag{4.1.3}$$

and refer to it in this thesis as the optical fibre nanowire loss.

The transmission loss of an OFN depends on the wavelength of the transmitted light. Standard fibres have a loss as small as 2×10^{-7} dB/mm at wavelengths in the region of 1.55 μm. The taper-drawing technique (discussed in Chapter 2) allows the fibre diameter to change smoothly and the loss of an OFN can be as low as 10^{-3} dB/mm, which is better than the loss of the planar waveguide with sub-micrometric diameters, but still not as good as the loss measured in standard telecom fibres.

There are two main reasons for the loss in OFN and standard telecom fibres:

1. Material absorption: All materials absorb at specific wavelengths corresponding to the electronic and vibration resonances associated with specific molecules. It consists of intrinsic and extrinsic absorptions. Intrinsic absorption losses correspond to absorption by fused silica (material used to make fibres) whereas extrinsic absorption is related to losses caused by impurities within silica. Extrinsic absorption arises generally from the presence of transition metal ions impurities and OH groups in glass. All of them have strong absorption in the visible and near infrared region.

Rayleigh scattering: It arises from local microscopic fluctuations in density. These density fluctuations arise as silica molecules move randomly in the molten state and then freeze in place during fibre fabrication. These density fluctuations lead to random fluctuations of the refractive index on a scale smaller than the optical wavelength λ. Light scattering in such a medium is known as *Rayleigh scattering* [2], which is the elastic scattering of light or other electromagnetic radiation by particles much smaller than the wavelength of the light. The scattering cross section varies as λ^{-4}.

The main reasons for the increased loss of OFN compared with standard telecom fibres are surface roughness and mode loss, discussed below:

1. Surface roughness: An ideal OFN guides an optical mode without energy leakage into the surrounding layer. In practice, imperfections on the surface (e.g., random radius variations) can lead to additional losses. The

physical process behind such losses is *Mie scattering* [2], which is the general theory of scattering of light from particles and it is used in the description of scattering from particles with size comparable to the wavelength. Rayleigh scattering can indeed be seen an approximation of Mie scattering for particles sizes considerably smaller than the wavelength. For OFNs, the importance of the imperfections on the surface is larger than for standard fibres because the small diameter means that more of the field interacts with the surface.

2. Mode loss: tapering of an optical fibre leads to a loss of power from the fundamental core mode because of the departure from the translational invariance of the uniform fibre. As the mode propagates along the taper transition, the field is unable to change its distribution rapidly enough to keep up with the variation of the local fundamental mode whose shape is determined by the local taper cross-section. The power loss from the core mode is associated with bending of the phase front coming from coupling of the fundamental mode with higher order modes. This coupled power then radiates away in a finite-clad fibre. This loss can be decreased when the profile of the taper is slow enough: we call this an adiabatic transition [3].

Additionally, some of the applications for OFN use bare OFN in air and, because of their small diameter; the OFNs are strongly affected by the surrounding environment. Of particularly importance is the OFN temporal stability. In reference [4] the optical and mechanical degradation of OFN was investigated and the optical spectra showed that an increasing unrecoverable loss was observed after fabrication. The optical loss was proportional to the mechanical degradation and it was attributed to the formation of cracks on the OFN surface exposed to air.

4.2 Nanowire Loss with Different Radii

In this section, the loss of different diameter nanowires manufactured by the flame brushing technique is investigated.

The total loss of the taper (fibre input facet to fibre output facet) was measured both during and at the end of the fabrication process. Light at 1.55μm from a laser diode was launched into the fibre and the transmitted signal was measured by connecting the output fibre to an InGaAs detector using a bare fibre adaptor. The temporal power stability of this measuring system was checked by analysing the transmission in an untapered fibre fixed on the fabrication rig for more than one hour prior to the taper manufacture. Power fluctuations of less than 0.1% over one hour were recorded.

22 tapers were fabricated from standard telecom fibres for this experiment. Fig. 4.1 shows the loss measurement on tapers with radii of 100-500nm at the end of their fabrication process. It should be noted that the values reported in Fig. 4.1 are overestimations since the measured loss also includes contributions from the taper transitions. Several different tapers with the same radius were measured. The loss is very high (>0.1 dB/mm) at small radii (<200 nm), which is not good for practical applications. The loss decreases to acceptable limits (~0.01 dB/mm) when the radius >300 nm. This allows them to be used in high-Q microfibre resonators or sensors. As expected, the average loss decreases with increasing diameters; the loss measurements are scattered around an average value because of a degree of instability in the environment cleanness and in the flame geometry.

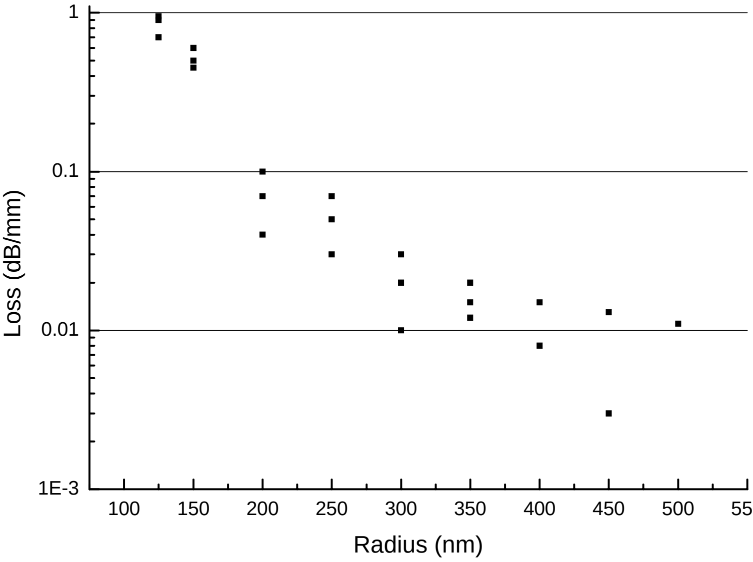

Fig. 4.1: The loss of nanowires as function of radius.

4.3 Embedding: a Method to avoid Unrecoverable induced Losses in Nanowires

Bare OFNs are strongly affected by the surrounding environment; there is an increasing unrecoverable loss after fabrication. This optical loss is attributed to the formation of cracks on the OFN surface exposed to air [4]. A practical solution for the fabrication of durable devices consists in coating OFNs with a low refractive index and low loss material such as Teflon which, in addition to protect the device, increases its robustness and portability. In this section, the aging of OFNs coated with Teflon is investigated and their loss is compared to the loss of bare OFNs in air.

Two OFNs used in these experiments were fabricated with the flame brushing technology, using the set-up presented in Section 2.2 and a microheater (NTT-AT, Japan). The taper profiles were analyzed with an optical microscope; Fig. 4.2 shows the profile of a typical bare taper. The length of the taper and the radius of the uniform waist region of the fabricated nanowires were 40 mm and ~450 nm respectively.

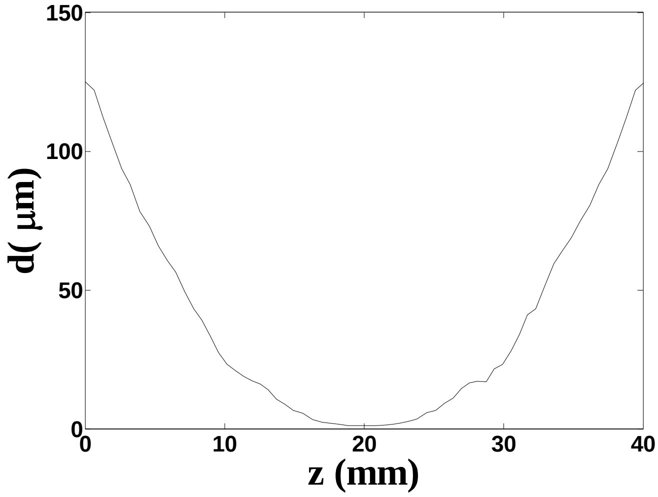

Fig. 4.2: Profile of the bare optical fibre nanowire (N1).

One of the samples was coated with Teflon, using a Teflon amorphous fluoropolymer resin in solution with 6% solid and T_g~160° C (Teflon AF, Dupont, US). The relevant product attributes are: high thermal, chemical, mechanical, and electrical stability; high creep resistance; low thermal conductivity; optical transparency over wide wavelength range; lowest index of refraction of any known polymer (1.31 at 1.55 μm wavelength); soluble in selected perfluorinated solvents (3M Company FC75 or FC40) and 6% solids.

The coating was carried out by first positioning the nanowires on a 100% Teflon substrate and then dropping Teflon solution on top of it. The sample was left to dry in air for a period ranging from several minutes to tens of minutes depending on the quantity of solution. A smooth uniform layer of Teflon covered the OFN after the solvent evaporation.

The power transmission was measured at 1.55 μm by connecting the fibre pigtails to an optical light source (FLS-2100, EXFO) and a power meter (The IQS-500 Intelligent Test System, EXFO).

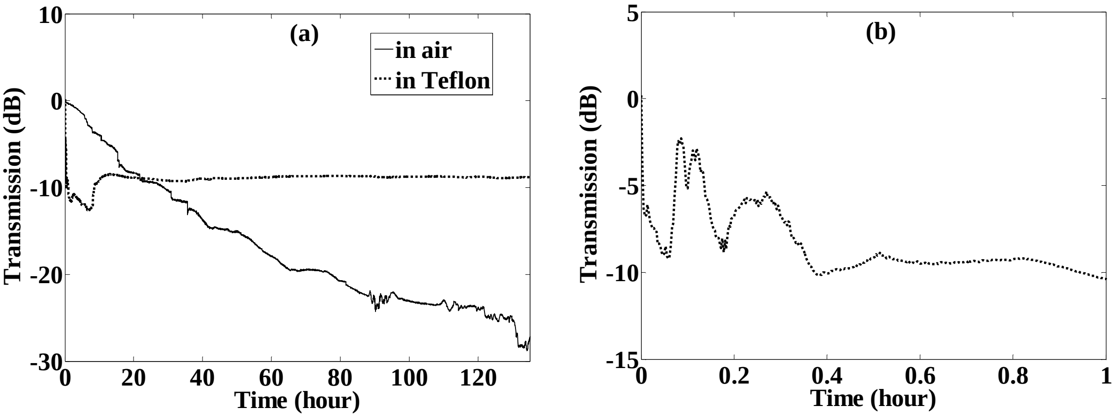

Fig. 4.3: (a) Power transmission over a period of 140 hours for bare (N1) and Teflon-coated (N2) OFN; (b): zoom of Fig. 4.3a for the sample N2.

Fig. 4.3 shows the varying power transmission during a period of about 140 hours for bare (N1) and coated (N2) OFN. Fig. 4.3(b) shows the early time evolution of the graph of N2 recorded during the coating process. In N1 the power transmission decreases with time at a rate of ~0.2 dB/hour, reaching ~30 dB after six days. The cleaning of the nanowire with conventional chemical compounds (acetone, isopropanol, methanol, and water) produced only a partial recovery of the induced loss. Although the loss can be completely recovered with a flame-brushing pass [4], this approach is not possible in practical devices and applications

The power transmission of N2 shows three different regions: in the first region (up to 0.4 hours), associated with embedding in the Teflon solution, the power transmission varies quickly, mainly because the solvent in the solution volatilizes rapidly. During the coating process the particles of Teflon move in the solution and the nanowire experiences a medium with continuously changing refractive index, therefore its transmission properties change. In the second temporal region (0.4-10 hours) a slow transmission variation was observed and attributed to the slow elimination of minute quantities of solvent left in the small interstices between Teflon particles. Finally, in the third region (at times longer than 10 hours) T2 is totally dry and its transmission properties are stable with time.

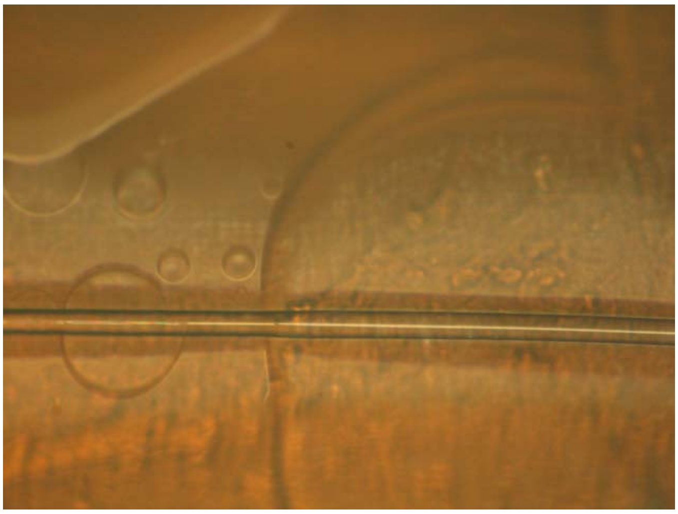

Fig. 4.4: Microscope picture of a Teflon-coated OFN.

Teflon is one kind of ultra-low loss material, for example, for water-core Teflon waveguides losses of 1 dB/m have been reported [5, 6]. The induced loss of ~9 dB observed during the coating process can be ascribed to the presence of particles and bubbles in the Teflon. Fig. 4.4 shows the optical microscope picture of a piece of N2: the coating appears uneven and some bubbles are trapped in the Teflon. It should be noted that the power transmission spectrum of N2 in Fig. 4.3a has small undulations (about 0.5 dB); these have been attributed to environmental changes in the laboratory (mainly temperature). The contamination issue could be avoided by working in a cleanroom environment and by depositing several thin layers of Teflon.

4.4 Summary

In this chapter, the loss of OFNs was discussed and the loss of different diameter OFNs measured; the loss of bare OFN and OFN embedded in Teflon were measured and compared with time, a method to avoid uncoverable induced loss by embedding the nanowire in Teflon was presented, which is useful for practical OFN resonators and sensors. From the next chapter onwards, the fabrication of OFN devices will be discussed.

4.5 References

1. G. P. Agrawal, *Fiber-optic communication systems* (Wiley-Interscience, New York, 2002).
2. M. Born, and E. Wolf, *Principles of optics : electromagnetic theory of propagation, interference and diffraction of light* (Cambridge University Press, Cambridge ; New York, 1999).
3. J. D. Love, W. M. Henry, W. J. Stewart, R. J. Black, S. Lacroix, and F. Gonthier, "Tapered Single-Mode Fibers and Devices .1. Adiabaticity Criteria," IEE Proceedings-J Optoelectronics **138**, 343-354 (1991).
4. G. Brambilla, F. Xu, and X. Feng, "Fabrication of optical fibre nanowires and their optical and mechanical characterisation," Electronics Letters **42**, 517-519 (2006).

5. R. Altkorn, I. Koev, R. P. VanDuyne, and M. Litorja, "Low-loss liquid-core optical fiber for low-refractive-index liquids: fabrication, characterization, and application in Raman spectroscopy," Applied Optics **36**, 8992-8998 (1997).
6. P. Dress, M. Belz, K. F. Klein, K. T. V. Grattan, and H. Franke, "Physical analysis of teflon coated capillary waveguides," Sensors and Actuators B-Chemical **51**, 278-284 (1998).

Chapter 5

Short Adiabatic Tapers for Optical Tweezers

In the next chapters, some applications of fibre tapers will be discussed; in this chapter the first application is presented: optical trapping and optical tweezers.

The mechanical action of optical fields can be exploited to trap and manipulate neutral particles with an exceptional degree of control. Many optical manipulation techniques are derived from optical tweezers [1]. Optical tweezers use forces exerted by a strongly focused beam of light to trap small objects. The force relies on the transfer of momentum between the beam of radiation and the object that it is passing through. Specifically, it is based on the transfer of momentum from the photons of the beam to the particle being trapped, a result of the refraction of the photons themselves as they pass between the boundary separating the object and medium. This refraction results in a force that effectively traps the particle in a 3D environment. Metallic probes with a sharp tip have also been proposed to trap small particles [2, 3]. The near field close to the sharp tip mainly consists of evanescent components which decay rapidly with distance from the tip, and it can generate a trapping potential deep enough to overcome Brownian motion and capture a nanometre size particle [2]. Alternatively, a combination of evanescent illumination from the substrate and light scattering at a tungsten probe apex is used to shape the optical field into a localized, 3D optical trap[3]. All these approaches require high powers for the illumination (well above 1 W).

Tapered fibre tips are very useful as optical tweezers, allowing for small probe size, submicron spots and could potentially reduce the trapping power by orders of magnitude. The main challenge is to manufacture short adiabatic tapers [4, 5]. As we mentioned in Chapter 2, when light propagates along the diameter-increasing or diameter-decreasing taper, there is a loss of the power from the fundamental core mode because the field is unable to change its distribution rapidly enough to keep up with the variation of the fundamental local mode whose shape is determined by the local taper cross-section. J. D. Love proposed criteria for an adiabatic taper: a taper is approximately adiabatic if the diameter at each point of the taper transition regions varies slowly enough to ensure that there is a negligible loss of power from the fundamental mode as it propagates along the length of the taper [5].

In this chapter, the optimum profile for minimum length adiabatic fibre tapers is calculated and short adiabatic tips which can be used to trap particles with low powers (~10 mW) are fabricated.

5.1 Theory of Short Adiabatic Tapers

Mathematically, any taper shape can be made using the shape model shown in Chapter 2; in this paragraph, the minimization of adiabatic taper length is discussed. Tapering optical fibres leads to a loss of power from the fundamental core mode because it couples to higher order modes [5]. A precise analysis of the loss along a tapered fibre or device is complicated and requires extensive numerical computation [4, 6]. Furthermore, such an analysis provides little insight into the controlling aspects of loss and its dependence on the local taper angle. Still, guidelines to the design of relatively short, low-loss, tapered fibres have been presented [4].

If the tapers are assumed axisymmetric, as is usually the case with a single fibre taper, then the fundamental HE_{11} local mode can couple only to modes with the same azimuthal-symmetry cladding-local-modes (i.e. to the higher order HE_{12}, HE_{13}, …), the reason is that the coupling is zero between HE_{11} and other modes [5]. For the fundamental mode, it is clear that the coupling will be predominantly to the higher order mode with a propagation constant closest to that of the fundamental mode, i.e. to the HE_{12} mode. Therefore, in order to minimise the loss it is necessary to minimise this coupling by optimizing the shape of the taper transition region.

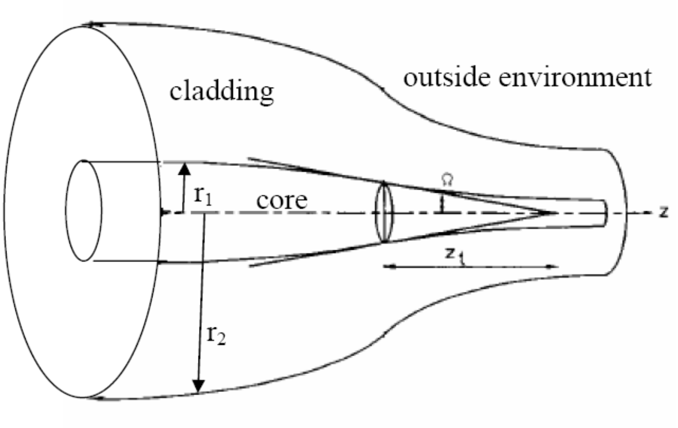

Fig. 5.1: Illustration of taper transition region [5].

The shape r_2(z) of the optimal taper is first calculated from the adiabatic criterion [5], which is derived from the physical argument that the local taper length-scale must be much larger than the coupling length between the fundamental mode and the dominant coupling mode for the power loss to be small. The local taper length-scale is defined as

$$z_a = r_1 / \tan(\Omega) \tag{5.1.1}$$

where Ω is the local angle and $\tan(\Omega)=dr_1/dz$, r_1 and r_2 are core and cladding radii, as shown in Fig 5.1. The local coupling length between the two modes is the beat length between the fundamental (HE_{11}) and local modes (HE_{21})

$$z_b = \frac{2\pi}{\beta_1(r_2) - \beta_2(r_2)} \tag{5.1.2}$$

where $\beta_1(r_2)$ and $\beta_2(r_2)$ are the respective propagation constants. The adiabatic criteria can then be written as

$$z_a \geq z_b \tag{5.1.3}$$

Using Eqs. (5.1.1) and (5.1.2), this can be written as

$$\left|\frac{dr_1}{dz}\right| \leq \frac{r_1[\beta_1(r_2)-\beta_2(r_2)]}{2\pi} \tag{5.1.4}$$

Assuming $\frac{r_2}{r_1}$ is constant during tapering, then $\frac{dr_1}{dz}=\frac{dr_2}{dz}$, and so we can obtain

$$\left|\frac{dr_2}{dz}\right| \leq \frac{r_2[\beta_1(r_2)-\beta_2(r_2)]}{2\pi} \tag{5.1.5}$$

Typically, $\beta_1(r_2)$ and $\beta_2(r_2)$ are calculated (numerically) as functions of r_2, as described in Chapter 2. The inequality (5.1.5) is converted into a differential equation by introducing a factor f, which specifies how much less the left-hand side of Eq. (5.1.5) should be than the right-hand side [5], and $\left|\frac{dr_2}{dz}\right|=-\frac{dr_2}{dz}$, since $r_2(z)$ is a decreasing function of z. This yields to:

$$\frac{dr_2}{dz}=-\frac{fr_2[\beta_1(r_2)-\beta_2(r_2)]}{2\pi} \tag{5.1.6}$$

With the initial condition $r_2 = r_0$ at $z = 0$, the solution to this equation is:

$$z(r_2)=-\frac{2\pi}{f}\int_{r_0}^{r_2}\frac{dr_2}{r_2[\beta_1(r_2)-\beta_2(r_2)]} \tag{5.1.7}$$

from which the inverse function $r_2(z)$ can be calculated numerically.

5.2 Simulations of Adiabatic Optical Tapers

For the standard telecom single mode fibre considered in Chapter 2.2, the optimal adiabatic taper transition profile $d(z)=2r_2(z)$ is drawn for $f=1$ and $r_0=62.5$ μm in Fig 5.2. When the taper waist is 1μm, the taper transition length is 2.8 mm.

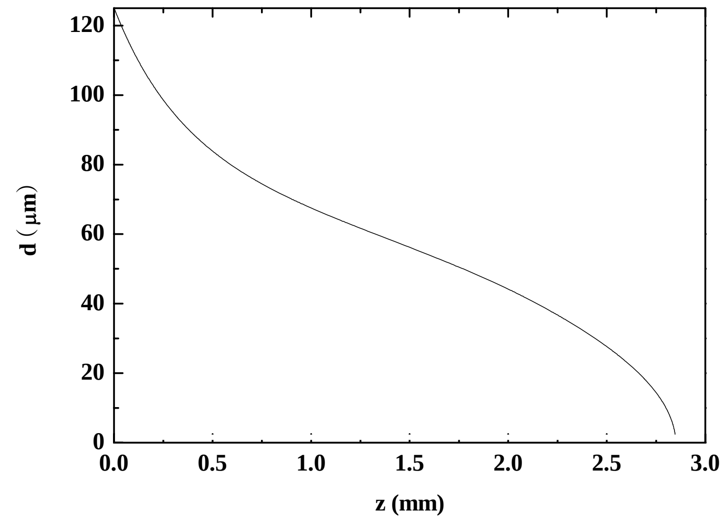

Fig. 5.2: The optimal f=1 adiabatic profile for 1550 μm in a standard single mode fibre.

The profile is drawn from $r_2=r_0$ to $r_2=0.01r_0$.

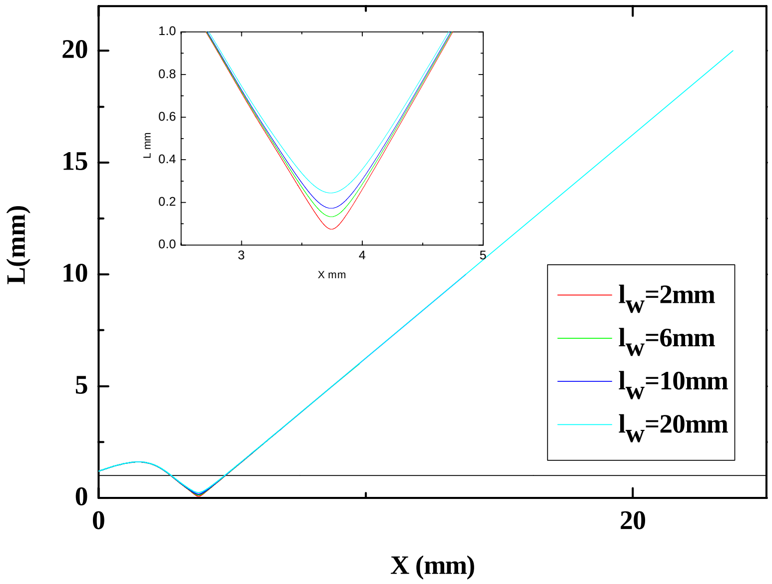

Fig. 5.3: A selection of hot-zone variations *L(x),* which will form the optimal adiabatic taper profile drawn in Fig. 5.2 with different taper waist lengths.

Having found the $d(z)$, the hot-zone variation $L(x)$ can be found with Eqs. (2.1.5)-(2.1.6) with l_w=2 mm, 6 mm, 10 mm, and 20 mm. Since for our set-up the stages pull at the velocity of 2 μm/s, $x=2\mu m/s\times t$ and we can get $L(t)$, the function of burner movement with time.

Fig. 5.3 shows the dependence of $L(x)$ for the taper profile drawn in Fig. 5.2 with the uniform waist $r_w=0.01r_0, f=1$, and for a range of final waist lengths l_w. Since the minimum L is less than 1mm, in practical set-ups the ideal shortest adiabatic taper shape is practically impossible to draw. In order to work with practical set-ups, we have to revise some parameters. From Eqs. (5.1.5) and (5.1.6), it is easy to understand that changing l_w has little benefit with the minimum L, so the best way is to modulate f as a function of z between 0 and 1.

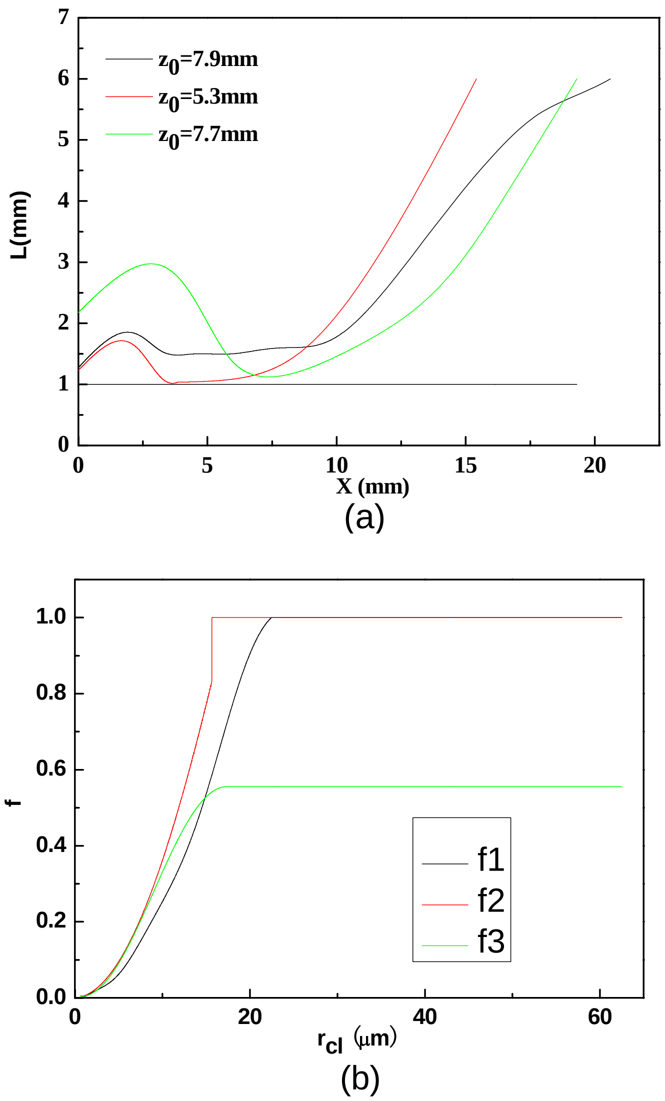

Fig. 5.4: (a) Three examples of practical hot-zone variations $L(x)$ versus fibre stretching and (b) the related f as functions of the cladding radius.

Fig. 5.4 presents results obtained with modulating *f*(*z*), for a taper waist length of 6 mm. Since *L* is always above 1mm, it is possible to draw the tapers with a very short taper transition region of about 5-8 mm. The adiabatic profiles for different wavelengths were also calculated. Fig. 5.5 shows the optimal *f*=1 adiabatic profile when λ=800 nm, 1000 nm, 1330 nm and 1550 nm. As expected, the length of adiabatic taper decreases with wavelength. Hence it is better to design the taper with the longest wavelength because the taper will be still adiabatic for shorter wavelengths.

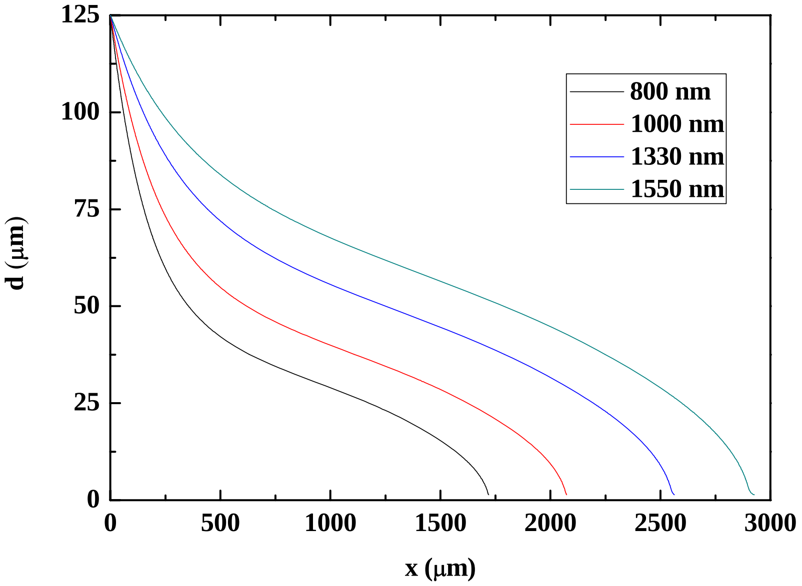

Fig. 5.5: The optimal *f*=1 adiabatic profile when λ=800 nm, 1000 nm, 1330 nm and 1550 nm.

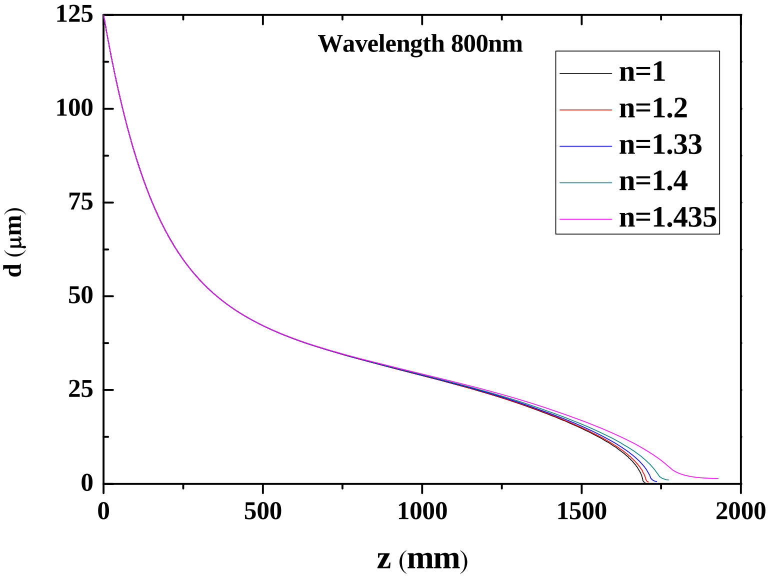

Fig. 5.6: The optimal adiabatic profile (*f*=1) when the index of environment n=1,1.2,1.33,1.4,1.435 for the wavelength λ=800 nm.

Also, for optical trapping it is important to know how the taper length changes with the surrounding environment. Fig. 5.6 shows the optimal $f=1$ adiabatic profile when the index of environment $n=1$, 1.2, 1.33, 1.4, 1.435 for wavelength $\lambda=800$ nm. There is not much difference except at the ends, because the effect of the surrounding medium is small when the diameter of the taper is thick and the mode is confined far from the surface.

5.3 Short Adiabatic Fibre Tip Fabrication

Section 5.1-5.2 calculated the optimum profiles of adiabatic tapers. Using a taper manufacturing rig it is theoretically possible to tailor the taper shape to the ideal "adiabatic" profile and to achieve insertion losses smaller than 0.05 dB (~1%) [7, 8]. In practice however, it is still difficult to fabricate very short tapers such as a 3mm taper from 125 μm to 1 μm because of the size of the microheater or microflame. A simple and quick alternative to the manufacture of very short tapers, is to use a commercially available pipette puller (model P2000), in a similar way to the manufacture of standard SNOM tips.

As introduced in Section 2.3, there are four parameters which can be adjusted to control the taper profile. Unfortunately however, the repeatability was not very good. In our experiments, these fabrication parameters were tuned in order to achieve an adiabatic profile. Some tapers were manufactured and their profile was checked with a high-magnification optical microscope. It is impossible to fabricate the same profile as the optimum profile in simulations. The closer the profiles to the theoretical adiabatic profiles, the better: the shortest adiabatic profile occurs at f=1. Fig. 5.7 shows the profiles of several tapers having similar profiles with the theoretical short optimal adiabatic profiles at four wavelengths (800 nm, 1000 nm, 1330 nm and 1550 nm). In (a) and (b) longer adiabatic profiles (f=0.7 or 0.8) are also shown together. Note that all the manufactured fibre tapers had a long pigtail to allow a ready connection to other optical fibre components. Different tapers were manufactured for different wavelengths, respectively. (800 nm: four tapers; 1000 nm: three tapers; 1330 nm: five tapers; 1550 nm: two tapers). The profiles of the experimental results are very different because of the poor repeatability. The central part is the most important because it represents the place where the mode moves from propagating into the core into propagating into the cladding and where conversion to higher order modes are most likely to happen. In Fig. 5.7 the best matches are Measured 4 in (a), Measured 2 in (b), Measured 3 in (c), Measured 2 in (d), respectively.

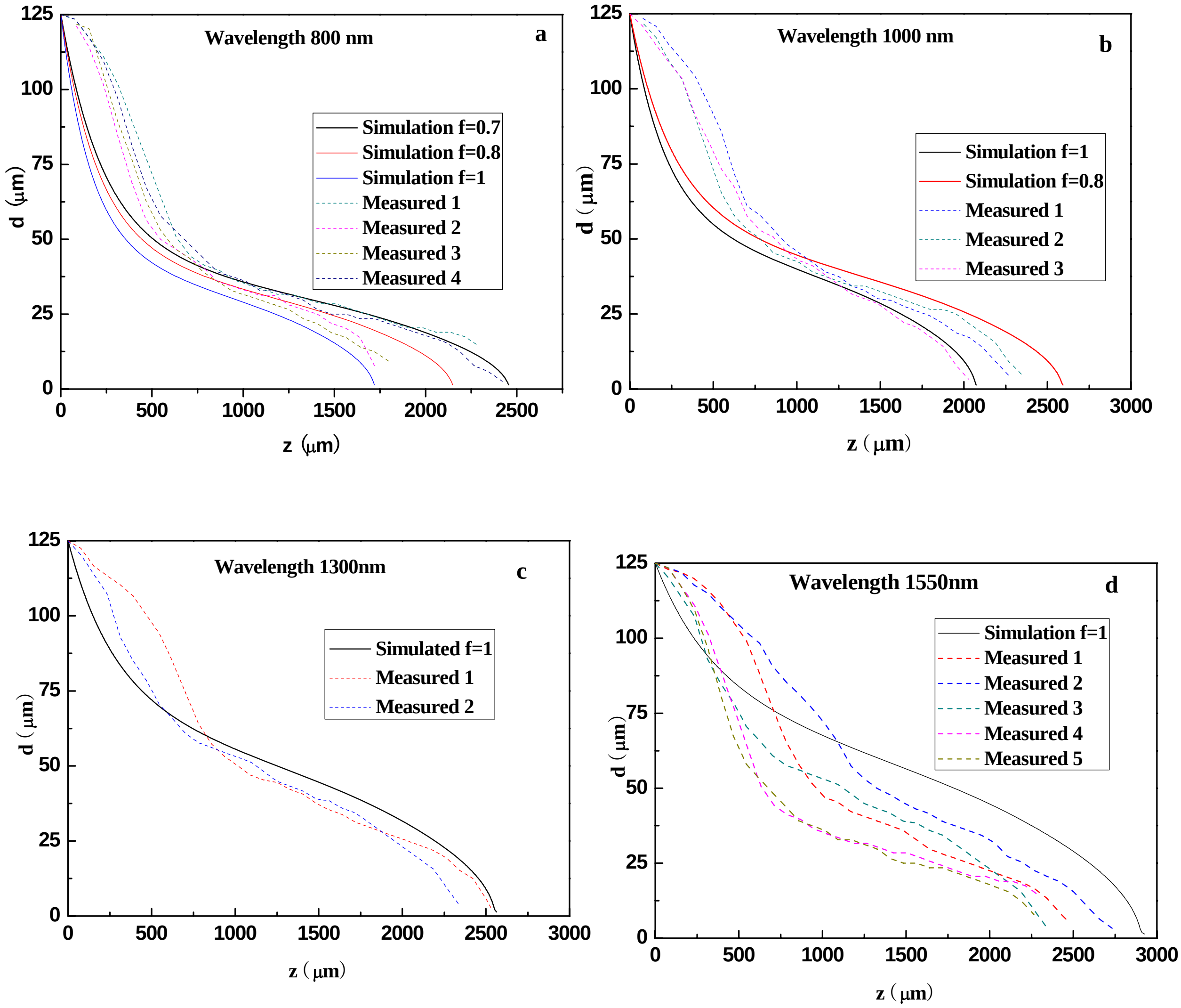

Fig. 5.7: Measured profiles of short taper compared with theoretical optimal profile when wavelength is 800 nm (a), 1000 nm (b), 1330 nm(c), 1550 nm (d).

5.4 Optical Trapping

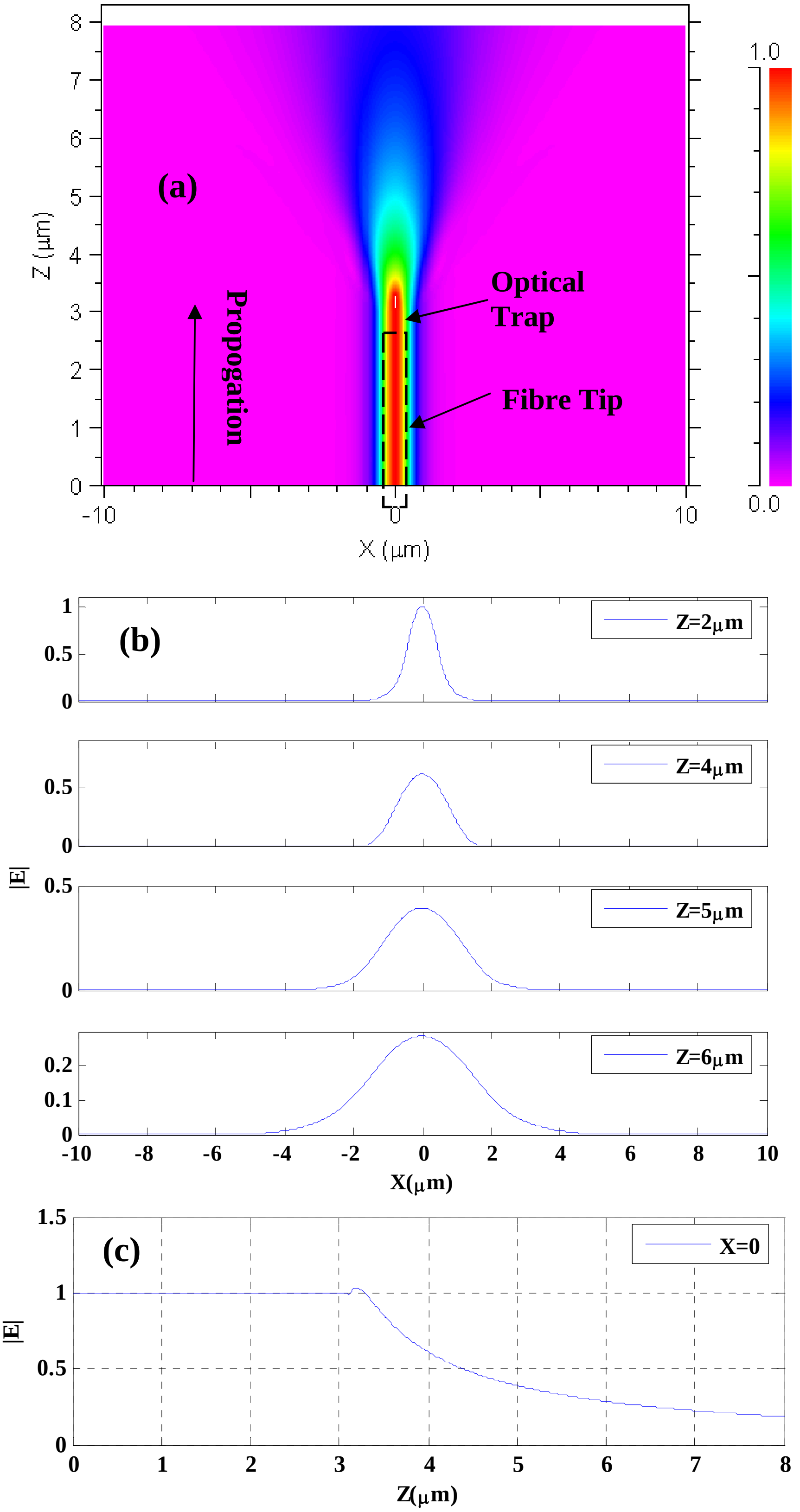

Fig. 5.8: Field distribution at fibre taper end. (a) Contourmap; (b) Cross-section of the field |*E*| at Z=2 μm, 4 μm, 5 μm, and 6 μm; (c) Cross-section of the field |*E*| at X=0.

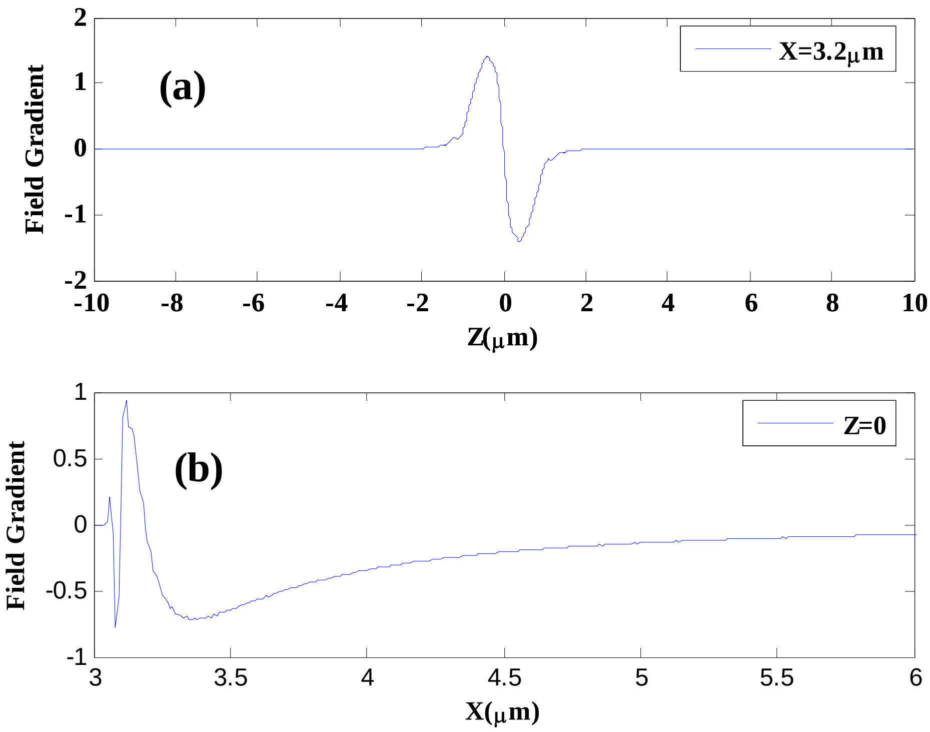

Fig. 5.9: Normalized field gradient at x=3.2 μm (a) and z=0 (b).

In the optical trapping experiments, the sample "measured 4" in Fig. 5.7(c) was used. The field distribution inside the optical fibre taper and at its output has been simulated using a commercial beam propagation method (Beamprop, Rsoft Inc.). Fig. 5.8(a) shows the result of the simulations at a wavelength 1.55 μm for a silica taper with radius r=500 nm and refractive index 1.44 in air (n=1), Fig. 5.8 (b) and (c) shows the cross-sections of the electrical field at *Z*=2 μm, 4 μm, 5 μm, and 6 μm, Fig. 5.8 (c) shows the cross-sections of the electrical field at X=0, the maxmum is at x=3.2 μm. As expected the beam leaves the fibre divergent and there is a maximum in the field (and therefore in the intensity) close to the fibre surface. The trapping force consists with the gradient and the scatting forces, the scattering force is due to absorbsion and reradiation of light by the dipole, and the gradient force arises from the interaction of the induced dipole with the inhomogeneous field. The gradient force is proportional the intensity gradient and points up to the gradient when the index of particle is larger than the medium[9].

$$F_{grad} = \frac{2\pi a^3}{c}\frac{(n_p/n_m)^2-1}{(n_p/n_m)^2+2}\nabla I_0 \tag{5.1.8}$$

Where a is the radii of the particle, n_p and n_m are the index of the particle and the medium, respectively.

Fig. 5.9 shows the normalized field gradient at z=0 and x=3.2µm: for the direction of x, the gradient is zero at z=0, when the particle is not at z=0, the gradient force will force the particle to move to the point at z=0; for the direction of z, the gradient is zero at x=3.2µm, when the particle is x>3.2um, the gradient force will force the particle to move to the point at x=3.2 um. As a example, we estimated the gradient force is 1pN per W at z=0 and x=4 um for a=500 nm by Eqa.(5.1.8)

Additionally, the gradient is proportional to the intensity and the size of the particle. However, if the size is larger, the center of the particle is farer from the focal point and the averaged force is smaller. That is why high power is necessary for large particle.

Experiments were carried out connecting the fibre taper by means of a bare fibre adapter to an Er-doped fibre amplifier (EDFA) capable of delivering 0.2 W of average power at ~1.55 µm, as shown in Fig. 5.10. The fibre taper was immersed in a solution containing silica microspheres with 1µm diameter and analyzed using an optical microscope connected to a PC using a TV card. The EDFA power was increased in steps of 0.1 mW and pictures were taken every ~1 s. Because of Brownian motion and other environmental factors the microparticles move quickly in water and no trapping was observed initially at the end of the tip. Once powers increase to the order of 10 dBm, particles were trapped at the taper tip.

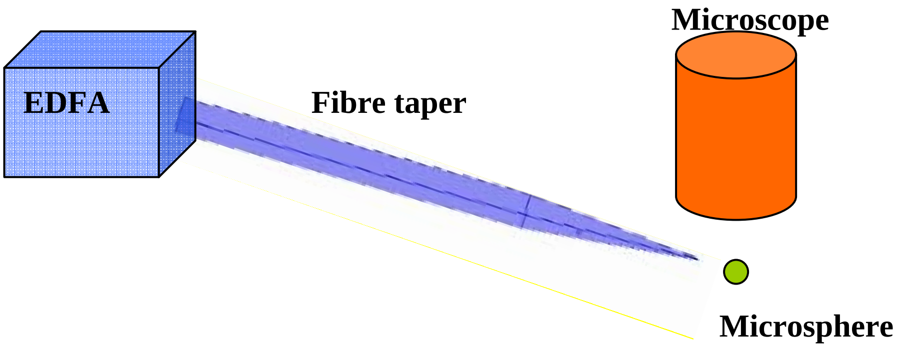

Fig. 5.10: Experimental set-up of optical trapping.

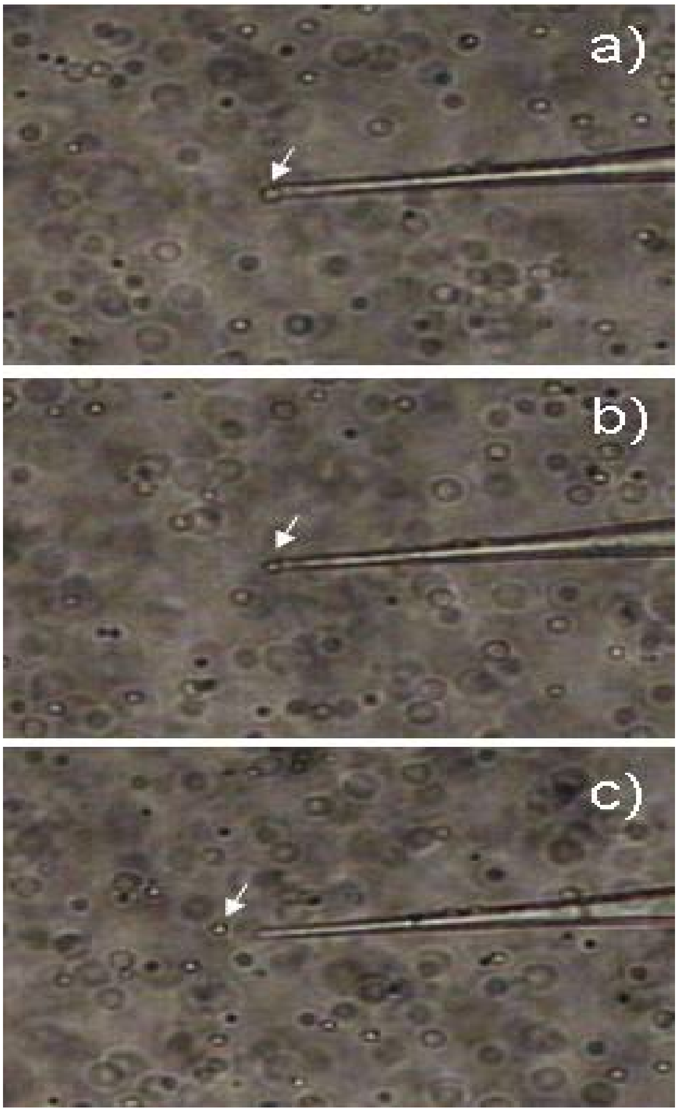

Fig. 5.11: Optical microscope pictures of a fibre taper tip in a solution of silica microspheres (diameter d=1 μm). In pictures (a) and (b) the laser output is in the order of 10 mW and a particle (indicated by an arrow) is trapped at the fibre tip. In picture (c) the laser is switched off and the particle is released.

Fig. 5.10a and 5.10b presents photos taken at ~1 s interval where it is clearly visible that a particle has been trapped at the fibre tip while the others move within the liquid. When the power was reduced (Fig. 5.11c), the particle was released from the optical trap at the fibre tip.

The experiment demonstrated that an adiabatic fibre taper is a good device for optical trapping: it uses low intensities ~10 mW, compared with ~1 W in Ref [10] and 22 mW in Ref [11]) and it has fibre pigtails compatible with fiberised components. Still, it has a major drawback: the tip needs to be positioned next to the particle.

The low trapping power is due to the low loss of this profile: most of power was transferred lossless from the pigtail to the end; in other kind of fibre tips, such as the fibre tip with a lens on the tip, the loss is very high because of the sharp profile, which is not adiabatic.

5.5 Summary

In this chapter, very short adiabatic tapers were designed and fabricated. Experimentally, the optical trapping of 1 μm microspheres was demonstrated using short tapers with low powers (10 mW). It is a new inexpensive method. In the future, shorter adiabatic tip could be manufactured from special fibres.

5.6 References

1. A. Ashkin, J. M. Dziedzic, J. E. Bjorkholm, and S. Chu, "Observation of a Single-Beam Gradient Force Optical Trap for Dielectric Particles," Optics Letters **11**, 288-290 (1986).

2. L. Novotny, R. X. Bian, and X. S. Xie, "Theory of nanometric optical tweezers," Physical Review Letters **79**, 645-648 (1997).

3. P. C. Chaumet, A. Rahmani, and M. Nieto-Vesperinas, "Optical trapping and manipulation of nano-objects with an apertureless probe," Physical Review Letters **88**, 123601 (2002).

4. J. D. Love, and W. M. Henry, "Quantifying Loss Minimization in Single-Mode Fiber Tapers," Electronics Letters **22**, 912-914 (1986).

5. J. D. Love, W. M. Henry, W. J. Stewart, R. J. Black, S. Lacroix, and F. Gonthier, "Tapered Single-Mode Fibers and Devices .1. Adiabaticity Criteria," IEE Proceedings-J Optoelectronics **138**, 343-354 (1991).

6. R. J. Black, S. Lacroix, F. Gonthier, and J. D. Love, "Tapered Single-Mode Fibers and Devices .2. Experimental and Theoretical Quantification," IEE Proceedings-J Optoelectronics **138**, 355-364 (1991).

7. S. G. Leon-Saval, T. A. Birks, W. J. Wadsworth, P. S. J. Russell, and M. W. Mason, "Supercontinuum generation in submicron fibre waveguides," Optics Express **12**, 2864-2869 (2004).

8. G. Brambilla, V. Finazzi, and D. J. Richardson, "Ultra-low-loss optical fiber nanotapers," Optics Express **12**, 2258-2263 (2004).

9. K. C. Neuman, and S. M. Block, "Optical trapping," Review of Scientific Instruments **75**, 2787-2809 (2004).

10. A. Ashkin, "Optical trapping and manipulation of neutral particles using lasers," BIOPHYSICS **94**, 4853 - 4860 (1997).

11. M.-T. Wei, K.-T. Yang, A. Karmenyan, and A. Chiou, "Three-dimensional optical force field on a Chinese hamster ovary cell in a fiber-optical dual-beam trap," Optics Express **14**, 3056-3064 (2006).

Chapter 6

Optical Nanowire Loop Resonator

The simplest nanowire device, which can be considered as a basic functional element of the microphotonic circuit, is the self-coupling nanowire loop resonator [1-3]. This resonator can be realized by wrapping a nanowire on a dielectric rod with smaller refractive index or by coiling directly in air. In the next sections, results on manufacturing coils with optical fibre nanowires are presented.

6.1 Theory of the Micro-resonator

In recent years, research interest in optical micro resonators has grown dramatically. This is due to the perception of their great potential in optical communications [4, 5], and sensing [6, 7]. An optical microresonator (with a size less than several millimeters) confines light to small volumes by resonant recirculation and has a size-dependent resonant-frequency spectrum. The microscopic volume ensures that the resonant frequencies are more sparsely distributed throughout this spectrum than they are in a corresponding ‘macroscale’ resonator. Microresonators have been achieved via a range of different designs, including whispering gallery resonators [8-11], microring resonators [12-14], micropost (or micropillar) cavities [15,16], photonic crystal defect microcavities [17], microdisk [18], Fabry-Perot bulk optical cavity [19], microsphere [20] and optical nanowire loop resonators (ONLRs) [1-3].

The ONLR is a miniature version of a fibre loop resonator, which was first made in 1982 from a conventional single-mode fibre and a directional coupler [21]. Due to the bending losses of the weakly guiding single mode optical fibre and to the dimensions of the fibre coupler, the maximum value of the free spectral range of the fibre resonator was limited to the order of a gigahertz. Later, a 2 mm diameter self-coupling fibre loop resonator was fabricated from a 8.5 μm diameter optical fibre taper [22]; the fibre diameter was too large to ensure sufficient self coupling, therefore the MLR was embedded into a silicone-rubber having a refractive index close to the index of the fibre in order to enhance the coupling efficiency. Recently, ONLRs in air [1-3] were manufactured from optical fibre nanowires with a 650nm diameter. Fig.6.1. shows the general shape of a nanowire loop with the input and output ends touching each other. The touching was maintainable due to surface attraction forces (Van der Waals and electrostatic), which kept the ends together and overcoming the elastic forces that would tend to straighten out the nanowire. Note that all the shapes of ONLRs are similar to the one in Fig. 6.1.

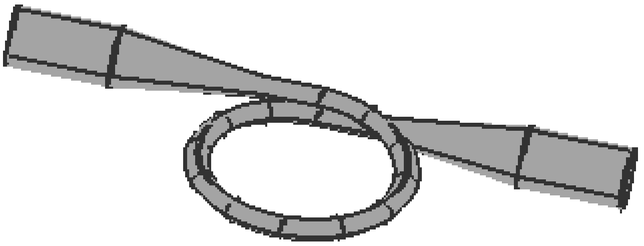

Fig. 6.1: Illustration of the ONLR.

Next, the theory of the two-port loop resonator is discussed.

For a two-port loop resonator (with input and output ports) as shown in Fig. 6.2, the length of the loop is L, the power coupling parameter is K, and the transmission is defined as the ratio of complex input and output field amplitude

$$T = \frac{A_{out}}{A_{in}} = |T| e^{i\theta} \tag{6.1.1}$$

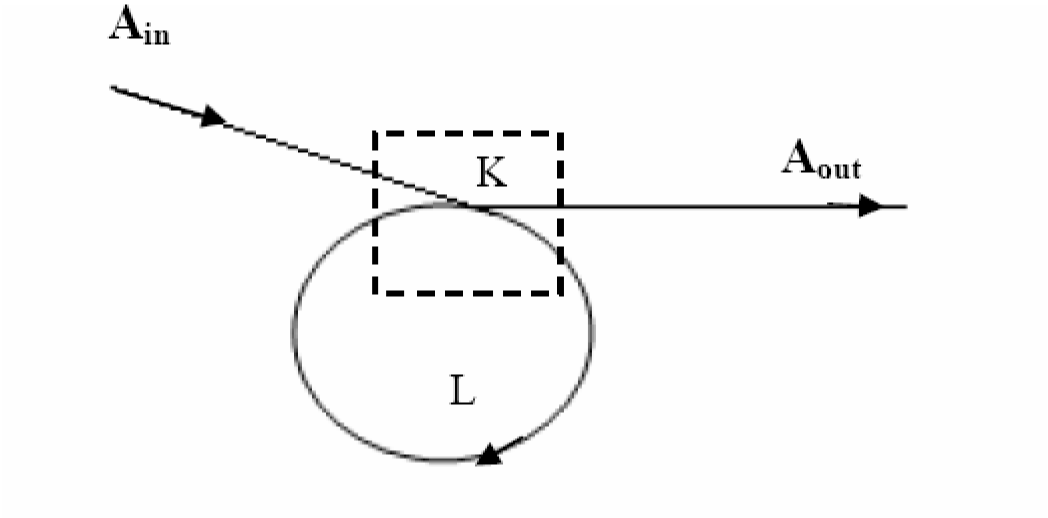

Fig. 6.2: Illustration of two-port optical loop resonator.

An ideal lossless cavity would confine light indefinitely and would have resonant frequencies at precise values. In this case $|T|=1$ but the phase (θ) is a function of the angular frequency ω.

As the resonator performs as an all pass filter [13] the resonances of transmission coefficient appear in the group delay, t_d, only. The group delay is a measure of the time delay experienced by narrow-band light pulses in an optical device, and is defined as the rate of change of the total phase shift with respect to angular frequency:

$$t_d = \frac{d\theta}{d\omega} \tag{6.1.2}$$

For the lossless loop resonator of Fig. 6.2, t_d is equal to the derivative of the phase of T with respect to the propagation constant β [23]:

$$t_d = \frac{n_l}{c}\frac{d\ln T}{d\beta} \tag{6.1.3}$$

where n_l is the index of the loop resonator.

There are several important parameters for describing loop resonators: quality factor (Q factor), free spectral range (FSR) and finesse f. The Q factor is proportional to the confinement time in units of the optical period, and also can be expressed as [24]

$$Q = \frac{\lambda}{FWHM} \tag{6.1.4}$$

where FWHM is the full width of half maximum of the transmission spectrum. Fig. 6.3 shows a typical periodical output intensity spectrum of a lossy loop resonator against wavelength. The typical Q-factor of ONLRs is in the range 1500-120000. In many potential applications, operation often involves monitoring the parameters of the resonance lines in the optical field. Since the quality factors are very high, even small scattering, coupling, or absorption out of the resonator mode set can be detected.

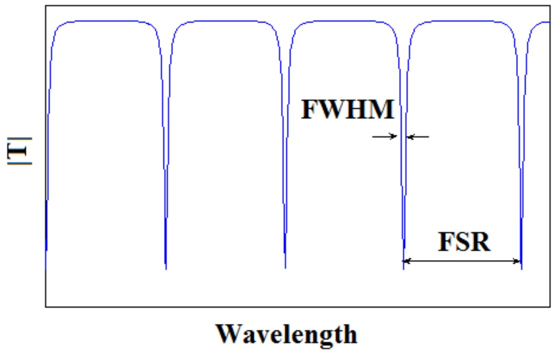

Fig. 6.3: Illustration of FSR and FWHM in typical output intensity spectrum of a lossy loop resonator.

In the loop resonator spectrum, the FSR is the wavelength or frequency period of peaks as shown in Fig. 6.3. Mathematically, FSR is the inverse of the round-trip time (round-trip group delay) of an optical pulse, it can be expressed as [24]:

$$FSR(Hz) = \frac{c}{2n_{eff}L} \tag{6.1.5}$$

It also can be expressed as the difference, $\Delta\lambda$, of two adjacent resonator wavelengths near wavelength λ:

$$FSR \approx \Delta\lambda \approx \frac{\lambda^2}{4\pi n_{eff} L} \tag{6.1.6}$$

The FSR is important in a number of areas. For example, in a laser resonator, the free spectral range determines the minimum spacing of lines in the optical spectrum of the laser output. For a wavelength-tunable single-frequency laser, it often (but not always) limits the achievable tuning range.

Finesse f is defined as FSR divided by the FWHM width of resonances of an optical resonator [24]:

$$Finesse = \frac{FSR}{FWHM} \tag{6.1.7}$$

A high finesse can be useful for optical spectrum analysis, because it allows the combination of a large FSR with a small resonator bandwidth. Therefore, a high spectral resolution in a wide spectral range is possible.

6.2 Fabrication and Transmission Spectra of the Optical Nanowire Loop Resonator

The fabrication of an ONLR consists in drawing the optical fibre nanowire and then bending it into a self-coupling loop. The method of drawing is illustrated in Chapter 2. The characteristic diameters of a nanowire used for the fabrication of an ONLR are in the range 600-1000 nm, which is approximately uniform along 2 mm of its length.

The setup for the ONLR fabrication is illustrated in Fig. 6.4. It consists of two XYZ translation stages, which can move the optical fibre nanowire ends in 3 directions. The nanowire loop is created by twisting the nanowire by hand and then manipulating the translation stages. With the aid of the stages and a stereo optical microscope, the nanowire can be coiled into a self-touching loop.

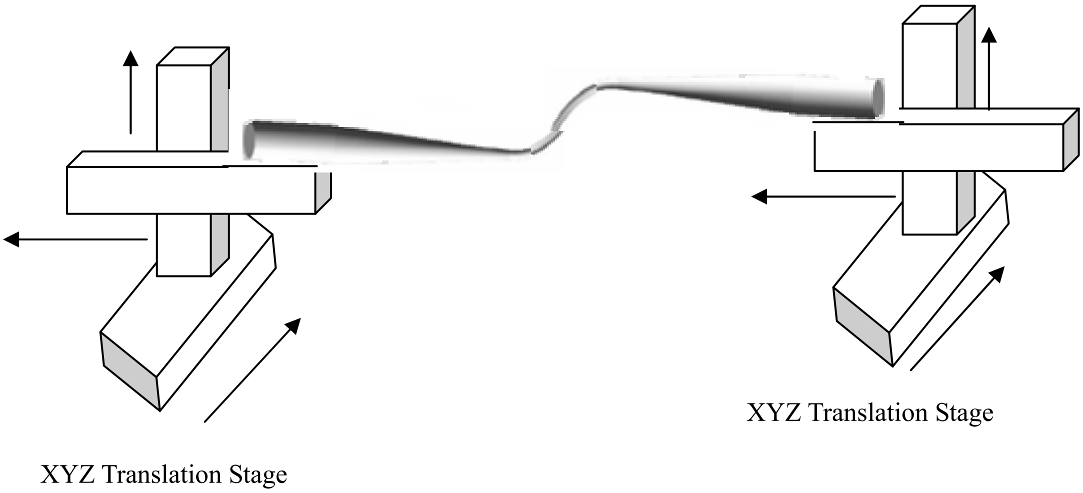

Fig. 6.4: Illustration of the nanowire bending and looping in free space using XYZ translation stages.

The spectrum of unpolarized light transmitted through several ONLRs were measured with an optical spectrum analyzer (OSA) as shown in Fig. 6.5. The spectra are presented in Fig. 6.6.

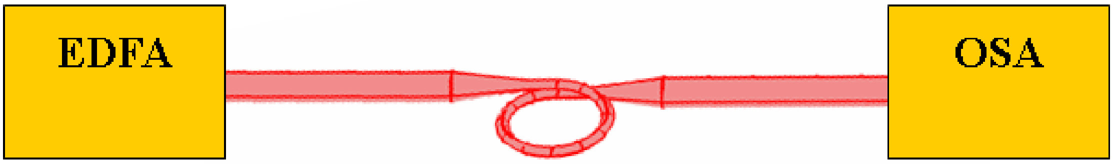

Fig. 6.5: Illustration of the spectrum measurement of an ONLR.

Fig. 6.6 shows the transmission spectrum of an ONLR, obtained by coiling a 750nm-diameter nanowire. The FSR is about 4nm, the resonator attenuation about 7 dB, and FWHM about 0.2 nm. According to Eq. (6.1.4), the Q-factor is 7800 and the finesse 20. The profile of the spectrum is not flat; it changes with wavelength, which mirrors the output spectrum of the EDFA.

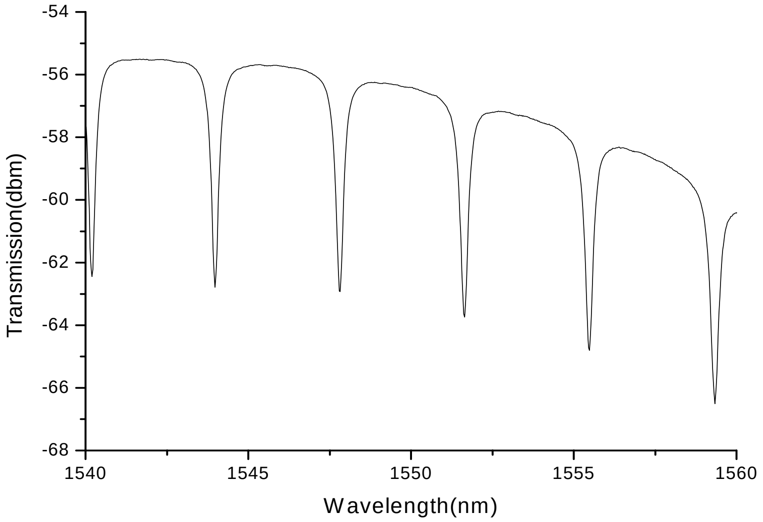

Fig. 6.6: Transmission spectra of a 750nm-diameter nanowire coil resonators.

FSR=4 nm.

The analytical formulation of the transmitted power *T* has been obtained by solving coupled wave formulas, which will be discussed in the next chapter. Here only the results are reported:

$$T = \frac{e^{i(\beta+i\alpha)L} - i\sin(K)}{e^{-i(\beta+i\alpha)L} + i\sin(K)} \tag{6.2.1}$$

where *K* is coupling parameters which depends on the coupling length and coupling coefficient, α is the loss. The nanowire is assumed uniform, and *β* independent on position. The resonator condition where |*T*| is the minimum and FSR are

$$\beta 2\pi R_0 = 2\nu\pi + \frac{\pi}{2} \tag{6.2.2}$$

$$\text{FSR} \approx \frac{\lambda^2}{n_{eff}L} \tag{6.2.3}$$

where ν is an integer, and R_0 is the radius of the loop.

The loop length $L=2\pi R_0$ of the resonator is estimated to be ~552 μm using Eq.(6.2.3).

Additionally, Eq. (6.2.1) was used to fit the spectra in Fig. 6.6 and the results are presented in Fig. 6.7. The peak at 1544nm was selected. Two parameters (coupling parameter K and loss α) are important for the profile, and were found with the following procedure: the output profile was calculated in steps of 0.05 for K (0-2) and 0.02 for α (0-1 dB/mm); the deviation between the simulation result and the experimental result was evaluated and the minimum tolerance was chosen. The possible coupling parameter K and loss α were 1 and ~0.3 dB/mm. As mentioned in Chapter 4, the general loss of nanowires with 750 nm-diameters is less than 0.1 dB/mm. The large loss observed in the loop resonator can be ascribed to some dirt on the surface of the nanowire when handling it in air. The bend loss can be ignored for $R_0\approx0.1$ mm and $r\approx375$ nm from Fig. 3.8 in Chapter 3.

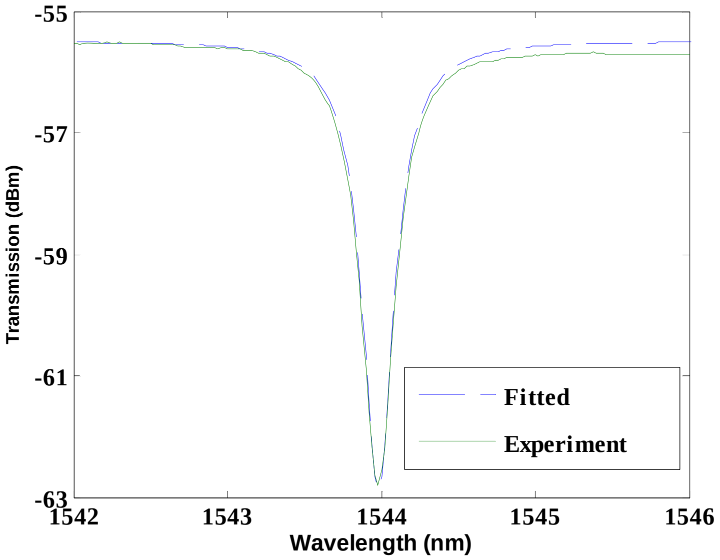

Fig. 6.7: Expanded view of the spectra presented in Fig. 6.6. The fit was carried out using Eq. (6.2.1).

6.3 Stability of ONLRs

Although ONLRs are very simple and useful microphotonic devices, before they can be used as building blocks for integrated microphotonic devices, an important challenge has to be overcome: the poor temporal stability. The ONLR is so light that it sways in air and the self-coupling strength changes quickly and irregularly, thus the resonator frequency shifts unexpectedly. This problem was addressed using aerogel as a substrate. Aerogel is a very light, extremely low density material with excellent thermal insulating properties and a refractive index close to 1. Also known as "frozen smoke", aerogel in its solid form has a texture similar to that of foamed polystyrene, and has a transparent optical spectral range similar to that of silica. As aerogel is mostly air, it has a refractive index very close to that of air, and a very small loss. It has been previously [25] used to fabricate linear waveguides, waveguide bends, and branch couplers.

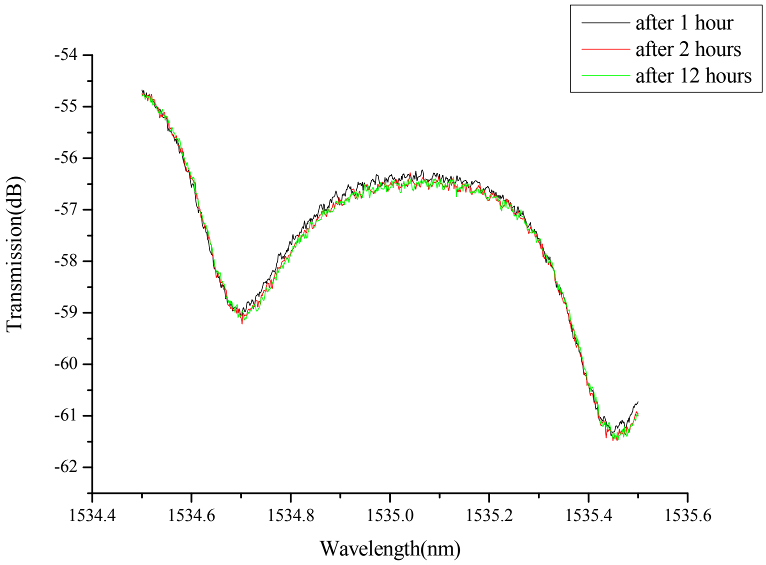

Fig. 6.8: The transmission spectrums of the 800 nm-diamaeter nanowire coil resonator on an aerogel after one hour, two hours and twelve hours.

Fig. 6.8 shows the transmission spectra of an ONLR sandwiched between two pieces of aerogel after one hour, two hours and one day. Even after one day, there are no considerable changes in the spectral profiles. This shows that aerogel is a very good substrate material on which to assemble ONLRs into functional microphotonics devices. Yet, aerogel is not strong and it is not a good packing material to protect the device. In the next chapters the use of polymeric compounds (Teflon) to coat the device will be investigated.

6.4 Cascaded ONLRs

As fundamental microphotonics devices, ONLRs can be combined to fabricate complex devices such as filters, one of the key components in modern optical communication. A simple and low cost way to manufacture complex response filters is to cascade multiple resonators of dissimilar diameters.

Here the simplest case is demonstrated by cascading two ONLRs with different loop radii. After two ONLRs I and II are put on the aerogel substrate, their transmission spectra are measured firstly separately (I and II), and then after cascading (I+II). The transmission spectra of the two filters are shown in Fig. 6.9.

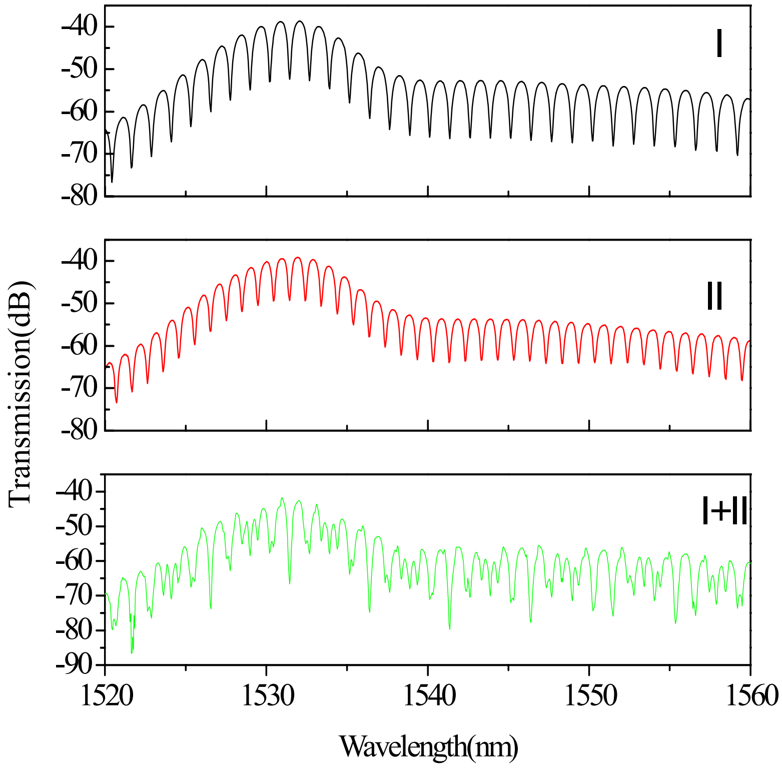

Fig. 6.9: Comparison between the transmission spectra of two separated ONLRs and of the structure obtained cascading them. The nanowire diameters were (a) 800 nm-and (b) 700 nm respectively.

The two ONLRs were fabricated from optical fibre nanowires which had the same diameter of 700 nm. The maximum attenuation near 1542 nm was 13 dB for I, 14 dB for II and 28 dB for I+II.

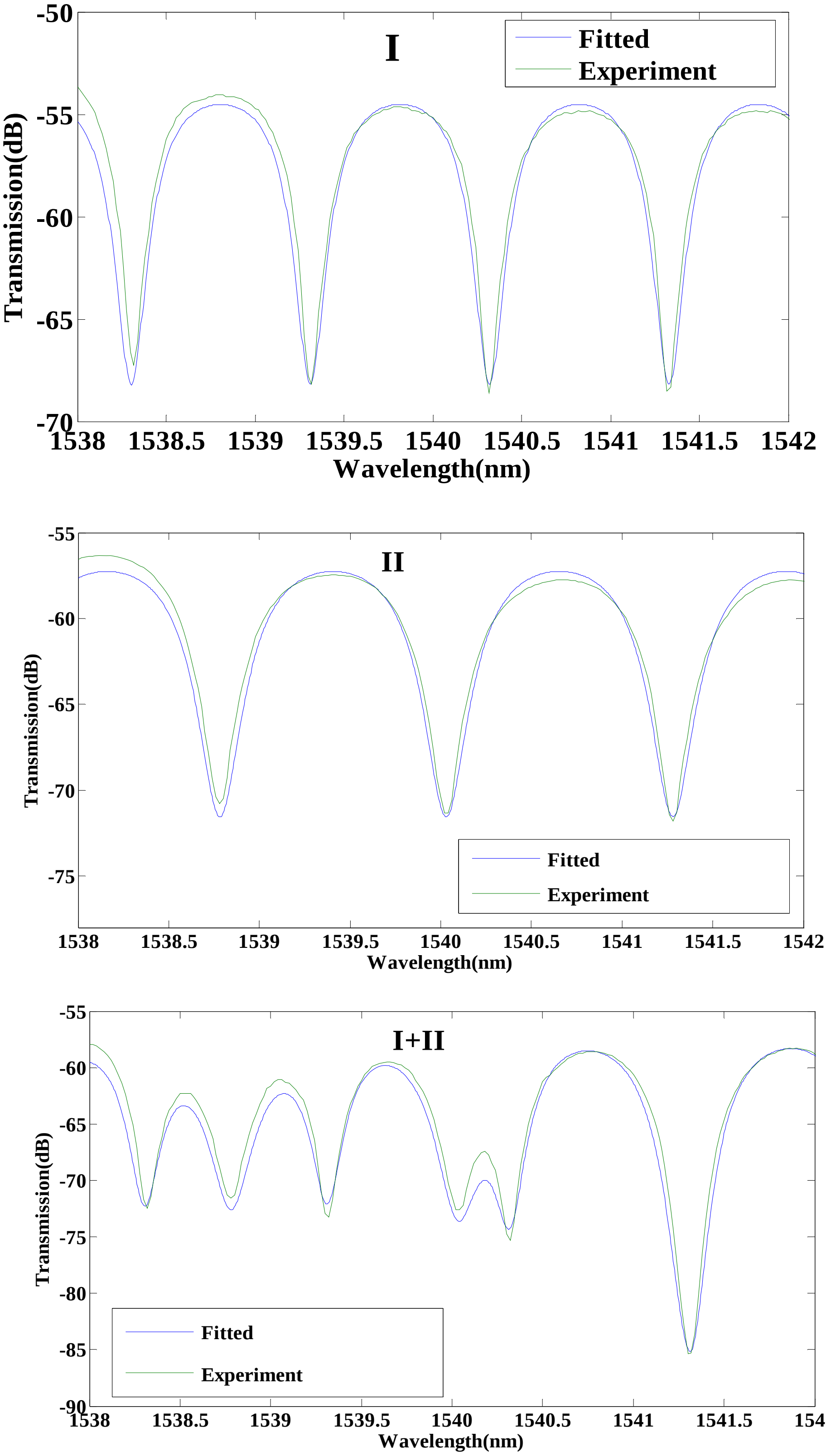

Fig. 6.10: Fitted results for I, II and I+II in Fig. 6.9.

The maximum attenuation of I+II is close to the sum of I and II, in line with expectations. The spectra can be fitted by Eq. (6.2.1). As shown in Fig. 6.10, I and II were fitted well, and the fitted result and experimental results of I+II are very similar. There is a little difference between fitted and experimental results because of the non-uniform diameters of the nanowires.

ONLRs also can be designed and manufactured as other components such as dispersion compensators and delay lines, which are the future prospects of ONLRs.

6.5 Summary

In this chapter, a high-Q resonator was introduced; the self-coupling loop resonator was demonstrated and discussed, its temporal stability was studied and solved by embedding it between aerogels; ONLRs cascading was demonstrated. The Q-factor of the loop resonator was about 7800, which is much smaller than the result reported by M. Sumetsky (120,000)[2]. This can be explained by the high loss. In the future, the loss should be reduced by manufacturing ONLRs in a cleanroom.

6.6 References

1. M. Sumetsky, Y. Dulashko, J. M. Fini, and A. Hale, "Optical microfiber loop resonator," Applied Physics Letters **86**, 161108 (2005).
2. M. Sumetsky, Y. Dulashko, J. M. Fini, A. Hale, and D. J. DiGiovanni, "The microfiber loop resonator: Theory, experiment, and application," Journal of Lightwave Technology **24**, 242-250 (2006).
3. M. Sumetsky, Y. Dulashko, and A. Hale, "Fabrication and study of bent and coiled free silica nanowires: Self-coupling microloop optical interferometer," Optics Express **12**, 3521-3531 (2004).
4. A. Yariv, Y. Xu, R. K. Lee, and A. Scherer, "Coupled-resonator optical

waveguide: a proposal and analysis," Optics Letters **24**, 711-713 (1999).

5. S. Mookherjea, and A. Yariv, "Coupled resonator optical waveguides," Ieee Journal of Selected Topics in Quantum Electronics **8**, 448-456 (2002).

6. M. Sumetsky, R. S. Windeler, Y. Dulashko, and X. Fan, "Optical liquid ring resonator sensor," Optics Express **15**, 14376-14381 (2007).

7. A. Schweinsberg, S. Hocde, N. N. Lepeshkin, R. W. Boyd, C. Chase, and J. E. Fajardo, "An environmental sensor based on an integrated optical whispering gallery mode disk resonator," Sensors and Actuators B-Chemical **123**, 727-732 (2007).

8. V. B. Braginsky, M. L. Gorodetsky, and V. S. Ilchenko, "Quality-Factor and Nonlinear Properties of Optical Whispering-Gallery Modes," Physics Letters A **137**, 393-397 (1989).

9. V. S. Ilchenko, A. A. Savchenkov, A. B. Matsko, and L. Maleki, "Dispersion compensation in whispering-gallery modes," Journal of the Optical Society of America a-Optics Image Science and Vision **20**, 157-162 (2003).

10. J. C. Knight, G. Cheung, F. Jacques, and T. A. Birks, "Phase-matched excitation of whispering-gallery-mode resonances by a fiber taper," Optics Letters **22**, 1129-1131 (1997).

11. S. M. Spillane, T. J. Kippenberg, O. J. Painter, and K. J. Vahala, "Ideality in a fiber-taper-coupled microresonator system for application to cavity quantum electrodynamics," Physical Review Letters **91**, 043902 (2003).

12. S. T. Chu, B. E. Little, W. G. Pan, T. Kaneko, S. Sato, and Y. Kokubun, "An eight-channel add-drop filter using vertically coupled microring resonators over a cross grid," IEEE Photonics Technology Letters **11**, 691-693 (1999).

13. B. E. Little, S. T. Chu, H. A. Haus, J. Foresi, and J. P. Laine, "Microring resonator channel dropping filters," Journal of Lightwave Technology **15**, 998-1005 (1997).

14. D. Rafizadeh, J. P. Zhang, S. C. Hagness, A. Taflove, K. A. Stair, S. T. Ho, and R. C. Tiberio, "Waveguide-coupled AlGaAs/GaAs microcavity ring and disk resonators with high finesse and Z1.6-nm free spectral range," Optics Letters **22**, 1244-1246 (1997).

15. J. M. Gerard, D. Barrier, J. Y. Marzin, R. Kuszelewicz, L. Manin, E. Costard, V. ThierryMieg, and T. Rivera, "Quantum boxes as active probes for photonic microstructures: The pillar microcavity case," Applied Physics Letters

69, 449-451 (1996).

16. J. M. Gerard, B. Sermage, B. Gayral, B. Legrand, E. Costard, and V. Thierry-Mieg, "Enhanced spontaneous emission by quantum boxes in a monolithic optical microcavity," Physical Review Letters **81**, 1110-1113 (1998).

17. O. Painter, R. K. Lee, A. Scherer, A. Yariv, J. D. O'Brien, P. D. Dapkus, and I. Kim, "Two-dimensional photonic band-gap defect mode laser," Science **284**, 1819-1821 (1999).

18. K. Djordjev, S. J. Choi, S. J. Choi, and P. D. Dapkus, "Microdisk tunable resonant filters and switches," Ieee Photonics Technology Letters **14**, 828-830 (2002).

19. J. R. Buck, and H. J. Kimble, "Optimal sizes of dielectric microspheres for cavity QED with strong coupling," Physical Review A **67**, 033806 (2003).

20. D. W. Vernooy, V. S. Ilchenko, H. Mabuchi, E. W. Streed, and H. J. Kimble, "High-Q measurements of fused-silica microspheres in the near infrared," Optics Letters **23**, 247-249 (1998).

21. L. F. Stokes, M. Chodorow, and H. J. Shaw, "All-Single-Mode Fiber Resonator," Optics Letters **7**, 288-290 (1982).

22. C. Caspar, and E. J. Bachus, " Fibre-optic microring-resonator with 2mm diameter," Electronnics Letters **25**, 1506–1508 (1989).

23. M. Sumetsky, "Optical fiber microcoil resonator," Optics Express **12**, 2303-2316 (2004).

24. O. Schwelb, "Transmission, group delay, and dispersion in single-ring optical resonators and add/drop filters - A tutorial overview," Journal of Lightwave Technology **22**, 1380-1394 (2004).

25. L. M. Tong, J. Y. Lou, R. R. Gattass, S. L. He, X. W. Chen, L. Liu, and E. Mazur, "Assembly of silica nanowires on silica aerogels for microphotonic devices," Nano Letters **5**, 259-262 (2005).

Chapter 7

Optical Fibre Nanowire Microcoil Resonator

After reviewing the resonator based on a simple loop (ONLR), introduced in Chapter 6, in this chapter the 3D Optical Nanowire Microcoil Resonator (ONMR) with self-coupling single mode fibre helical microcoils will be discussed. The 3D geometry can be created by wrapping an optical nanowire on a dielectric rod having a smaller refractive index, as illustrated in Fig. 7.1. The red and green arrows show two possible directions of light propagation. Resonances are formed by the interference of light going from one turn to another along the nanowire and returning back to the previous turn with the aid of weak coupling. Compared to the structures discussed in the last Chapter, their geometrical structures are more stable, making them suitable for stable applications.

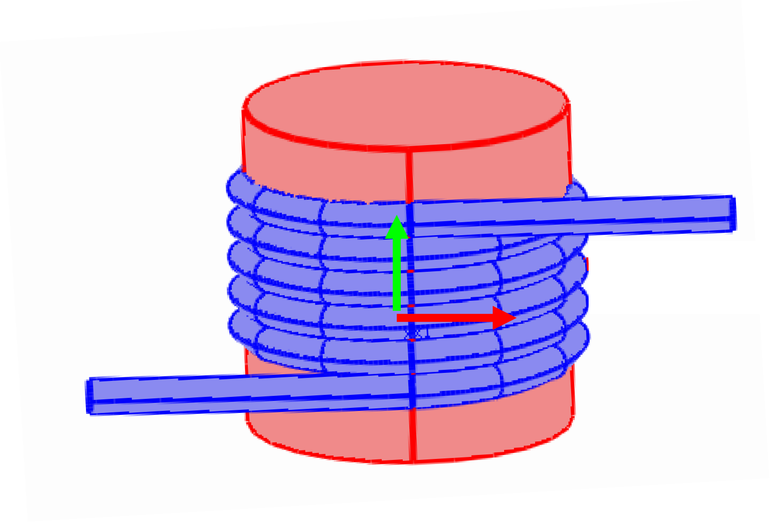

Fig. 7.1: Schematic of an ONMR; an optical fibre nanowire is coiled on a low refractive index support rod.

In practical manufacture, ONMRs with more turns longer nanowires are required, therefore they are much more difficult. In this thesis, only ONMRs with few turns are considered.

In this chapter ONMRs are investigated; the fundamental coupled mode theory is used to solve the transmission and three kinds of optimum method are presented to enhance the ease of manufacture of high-Q 3D microcoil resonators.

7.1 Coupled Wave Equations for ONMRs

Fig. 7.2 illustrates propagation of light along a single mode optical fibre nanowire wound on a dielectric rod having a lower refractive index smaller than the index of the fibre. The fibre diameter is taken to be smaller than or comparable to the wavelength of the radiation propagating in it. The local natural coordinate system (*x, y, s*) is introduced in Fig. 7.2, where *s* is the coordinate along the fibre axis and (*x, y*) are the coordinates along the normal, **n**, and binormal, **b**, of the resonator axis, respectively. If the characteristic transverse dimension of the propagating mode is much smaller than the characteristic bend radius, the propagation electric field can be written as [1]

$$E\ (x,y,s)=A(s)F_0(x,y)\exp\left\{i\int^{s}\beta(s)ds\right\}\exp(i\omega t)+\text{c.c.} \qquad (7.1.1)$$

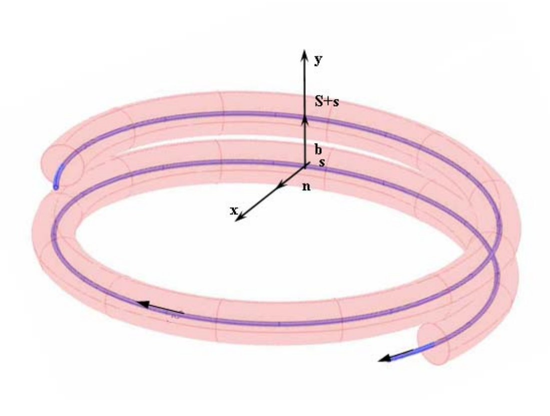

Fig. 7.2: Illustration of local natural coordinate system of an ONMR.

Here the vector function $F_0(x,y)$ defines the local eigen mode corresponding to the propagation constant $\beta(s)$, $A(s)$ is the amplitude at the position *s*, *t* is the time, and ω is the frequency. It is convenient to define the amplitude of the field at a turn *m* as $A_m(s)$ and to consider s as the common coordinate along turns, so that $0 < s < S_m$, where S_m is the length of the m^{th} turn. If every turn is taken as a round with a radius R_m, s can be expressed as $R_m\theta\,(0 \le \theta \le 2\pi)$ in polar coordinates as shown in Fig 7.3(a). Fig. 7.3(b) shows the cross-sections of p^{th} and q^{th} turns, where n_f is the index of the nanowire and n_c is the index of the environment.

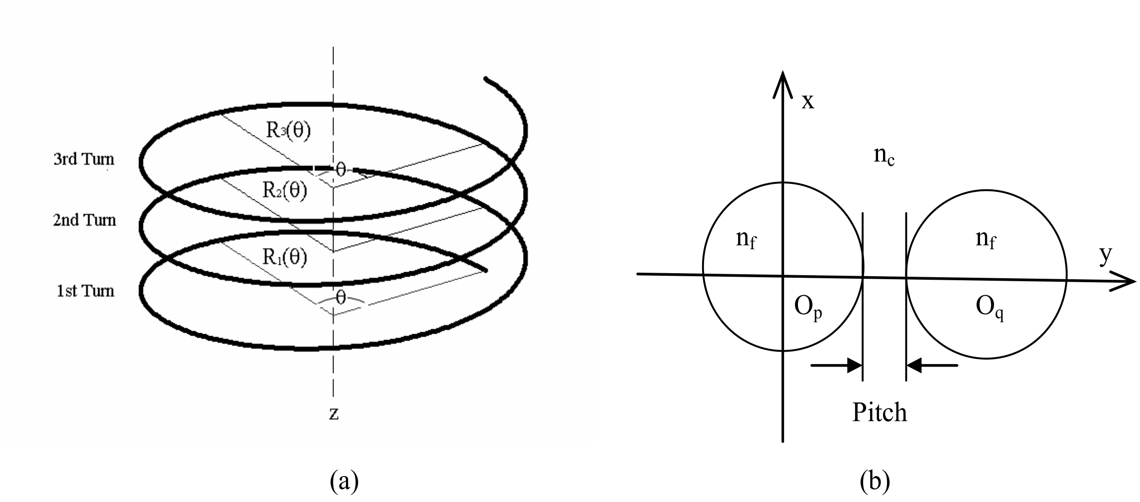

Fig. 7.3: (a) Illustration of an ONMR in cylindrical coordinates.
(b) The cross-sections of two nanowires;

The field in the m^{th} can be expressed as:

$$E_m(x, y, \theta) = A_m(\theta)F_0(x, y)\exp\{\beta R\theta\} \qquad (7.1.2)$$

Here we assume the nanowire is uniform and β is independent on s.

With the conventional coupled mode theory[2], the coupled equations for the coefficients $A_m(\theta)$ can be obtained on the condition of relatively slow variation of coefficients $A_m(\theta)$. As described in Refs. [1, 3], the propagation of light along the coil in a two-turn and three-turn ONMR are described by the coupled wave equations.

In the two-turn ONMR:

$$\frac{d}{d\theta}\begin{pmatrix} A_1 \\ A_2 \end{pmatrix} = i\begin{pmatrix} 0 & R_1(\theta)\chi_{12}(\theta) \\ R_2(\theta)\chi_{21}(\theta) & 0 \end{pmatrix}\begin{pmatrix} A_1 \\ A_2 \end{pmatrix} \qquad (7.1.3)$$

In the three-turn ONMR:

$$\frac{d}{d\theta}\begin{pmatrix} A_1 \\ A_2 \\ A_3 \end{pmatrix} = i\begin{pmatrix} 0 & R_1(\theta)\chi_{12}(\theta) & 0 \\ R_2(\theta)\chi_{21}(\theta) & 0 & R_2(\theta)\chi_{23}(\theta) \\ 0 & R_3(\theta)\chi_{32}(\theta) & 0 \end{pmatrix}\begin{pmatrix} A_1 \\ A_2 \\ A_3 \end{pmatrix} \qquad (7.1.4)$$

where $\chi_{pq}(\theta) = \kappa_{pq}(\theta)\exp\left\{ i\int_0^{2\pi}\beta_p(\theta)rd\theta - i\int_0^{2\pi}\beta_q(\theta)rd\theta \right\}$ and $\kappa_{pq}(\theta)$ is the coupling coefficient between the turns *p* and *q* (*p, q* =1, 2, 3, …)[2]:

$$k_{pq} = \frac{\omega\varepsilon_0 \iint\limits_{O_p} (n_f^2 - n_c^2) E_p^* \cdot E_q dxdy}{\int_{-\infty}^{\infty}\int_{-\infty}^{\infty} u_z \cdot (E_p^* \cdot H_p + H_p^* \cdot E_p) dxdy} \qquad (7.1.5)$$

and E_p (E_q) and H_p(H_q) are the electromagnetic mode fields when light is propagating in the nanowire *p*(*q*), as shown in Fig. 7.3(b).

In Eq. (7.1.4), the coupling between turns 1 and 3 is not considered, and it will be discussed later.

Generally, the propagation of light along the coil in a *M*-turn ONMR is described by the coupled wave equations, which takes into account coupling between adjacent turns:

$$\frac{d}{d\theta}\begin{pmatrix} A_1 \\ A_2 \\ \cdots \\ A_m \\ \cdots \\ A_{M-1} \\ A_M \end{pmatrix} = i\begin{pmatrix} 0 & R_1(\theta)\chi_{12}(\theta) & 0 & \cdots & 0 & 0 & 0 \\ R_2(\theta)\chi_{21}(\theta) & 0 & R_2(\theta)\chi_{23}(\theta) & \cdots & 0 & 0 & 0 \\ 0 & R_3(\theta)\chi_{32}(\theta) & 0 & \cdots & 0 & 0 & 0 \\ \cdots & \cdots & \cdots & \cdots & \cdots & \cdots & \cdots \\ 0 & 0 & 0 & \cdots & 0 & R_{M-2}(\theta)\chi_{M-1M-2}(\theta) & 0 \\ 0 & 0 & 0 & \cdots & R_{M-1}(\theta)\chi_{M-2M-1}(\theta) & 0 & R_{M-1}(\theta)\chi_{M-1M}(\theta) \\ 0 & 0 & 0 & \cdots & 0 & R_M(\theta)\chi_{MM-1}(\theta) & 0 \end{pmatrix}\begin{pmatrix} A_1 \\ A_2 \\ \cdots \\ A_m \\ \cdots \\ A_{M-1} \\ A_M \end{pmatrix}$$

(7.1.6)

where for a uniform-waist optical fibre nanowire all β_p are independent of θ (*p*=1,2,…,*M*). In this thesis, Eq.(7.1.6) is solved with MATLAB.

The coefficients satisfy the continuity conditions

$$R_{m+1}(0) = R_m(2\pi) \tag{7.1.7}$$

$$A_{m+1}(0) = A_m(2\pi)\exp\left\{ i\int_0^{2\pi} \beta(\theta)R_m d\theta \right\}, m = 1,2,\ldots M-1. \tag{7.1.8}$$

The equation can be simplified by introducing the average radius R_0, coupling parameter K_{pq} and transmission amplitude T:

$$R_0 = (\sum_{m=1}^{M}\int_0^{2\pi} R_m(\theta)d\theta) \Big/ 2\pi M \tag{7.1.9}$$

$$K_{pq} = 2\pi R_0 \kappa_{pq}(\theta) \tag{7.1.10}$$

Finally the transmission coefficient was defined as:

$$T = \frac{A_M(2\pi)}{A_1(0)}\exp\left\{ i\int_0^{2\pi} \beta R_M(\theta)d\theta \right\}. \tag{7.1.11}$$

When the loss or gain α is considered, β is replaced by a complex number $\beta+i\alpha$. If the propagation losses and gains are ignored, then the propagation constant, β is real α=0, and $|T| = 1$. In this case, the coil performs as an all pass filter and the resonances of transmission coefficient appear in the group delay (t_d) only. The group delay can be calculated by Eq. (6.1.3).

In order to simplify the formula, the optical fibre nanowire diameter and the pitch between adjacent turns are assumed uniform, so the coefficient κ and β are independent of θ. R is taken independent of θ, which implies that R_i is constant in each ith turn. In this case, the coupling parameter can be expressed as

$$K = 2\pi R_0 \kappa, \tag{7.1.12}$$

where

$$R_0 = \frac{1}{M}\sum_{m=1}^{M} R_m \tag{7.1.13}$$

is the average radius.

By applying the transformations

$$B_m(\theta) = A_m(\theta)\exp\left\{i\beta R_m\theta\right\}, m = 1,2,\ldots M-1. \tag{7.1.14}$$

the coupled wave equations can be written as

$$\frac{d}{d\theta}\begin{pmatrix} B_1 \\ B_2 \\ \cdots \\ B_m \\ \cdots \\ B_{M-1} \\ B_M \end{pmatrix} = i\begin{pmatrix} -R_1\beta & R_1\kappa & 0 & \cdots & 0 & 0 & 0 \\ R_2\kappa & -R_2\beta & R_2\kappa & \cdots & 0 & 0 & 0 \\ 0 & R_3\kappa & -R_3\beta & \cdots & 0 & 0 & 0 \\ \cdots & \cdots & \cdots & \cdots & \cdots & \cdots & \cdots \\ 0 & 0 & 0 & \cdots & -R_{M-2}\beta & R_{M-2}\kappa & 0 \\ 0 & 0 & 0 & \cdots & R_{M-1}\kappa & -R_{M-1}\beta & R_{M-1}\kappa \\ 0 & 0 & 0 & \cdots & 0 & R_M\kappa & -R_M\beta \end{pmatrix}\begin{pmatrix} B_1 \\ B_2 \\ \cdots \\ B_m \\ \cdots \\ B_{M-1} \\ B_M \end{pmatrix}$$

(7.1.15)

With the continuity conditions

$$B_{m+1}(0) = B_m(2\pi), m = 1,2,\ldots M-1. \tag{7.1.16}$$

The transmission amplitude is defined as:

$$T = \frac{B_M(2\pi)}{B_1(0)} \tag{7.1.17}$$

The simplest case is the uniform ONMR with the same radius and uniform pitches in all the *M* turns, $R_m = R_0$. Eq. (7.1.6) can be solved analytically for a lossless case by M. Sumetsky[1];

$$\begin{cases} B_m(\theta) = \sum_{n=1}^{M} b_{n1}B_{mn}(\theta)\exp(i\beta R_0\theta), \|b_{mn}\| = \|a_{mn}\|^{-1} \\ a_{mn} = \exp[i2\pi R_0(\beta + 2k\cos\frac{\pi n}{N+1})]\sin[\frac{\pi(m-1)n}{N+1}] - \sin[\frac{\pi mn}{N+1}], \quad (7.1.18) \\ B_{mn}(\theta) = \exp[4i\pi kR\cos\frac{\pi n}{N+1}]\sin[\frac{\pi mn}{N+1}], m,n = 1,2,\ldots,M \end{cases}$$

The transmission amplitude is

$$T = (A_1(0))^{-1} \sum_{n=1}^{M} b_{n1} B_{Nn}(2\pi) \qquad (7.1.19)$$

For a two-turn lossless uniform ONMR which is similar to a ring resonator [1]:

$$T = \frac{e^{i\beta 2\pi R_0} - i\sin(K)}{e^{-i\beta 2\pi R_0} + i\sin(K)} \qquad (7.1.20)$$

and the resonator conditions where the absolute of group delay $|t_d|$ is the maximum are:

$$K = K_u = (2u-1)\frac{\pi}{2} \qquad (7.1.21)$$

$$\beta 2\pi R_0 = 2v\pi + \frac{\pi}{2} \qquad (7.1.22)$$

where *u, v* are integers.

For a three-turn lossless uniform ONMR[1]:

$$T = \frac{e^{-i\beta 2\pi R_0} - \sqrt{2}i\sin(\sqrt{2}K) - e^{i\beta 2\pi R_0}\sin^2(\sqrt{2}K)}{e^{i\beta 2\pi R_0} + \sqrt{2}i\sin(\sqrt{2}K) - e^{-i\beta 2\pi R_0}\sin^2(\sqrt{2}K)} \qquad (7.1.23)$$

and the resonator conditions are[1]:

$$K = K_u^{(1)} = (2u-1)\frac{\pi}{\sqrt{2}}, \beta 2\pi R_0 = v\pi \qquad (7.1.24)$$

or $K = K_{u\varepsilon}^{(2)} = \sqrt{2}[\varepsilon \arcsin(\frac{1}{\sqrt{3}}) + u\pi], \beta 2\pi R_0 = (2v + \frac{\varepsilon}{2})\pi, \varepsilon = \pm 1$ (7.1.25)

As an example, the group delay was calculated against the wavelength near 1550 nm when *M*=2, 3 and 4, as shown in Fig. 7.4-7.6, for different *K*.

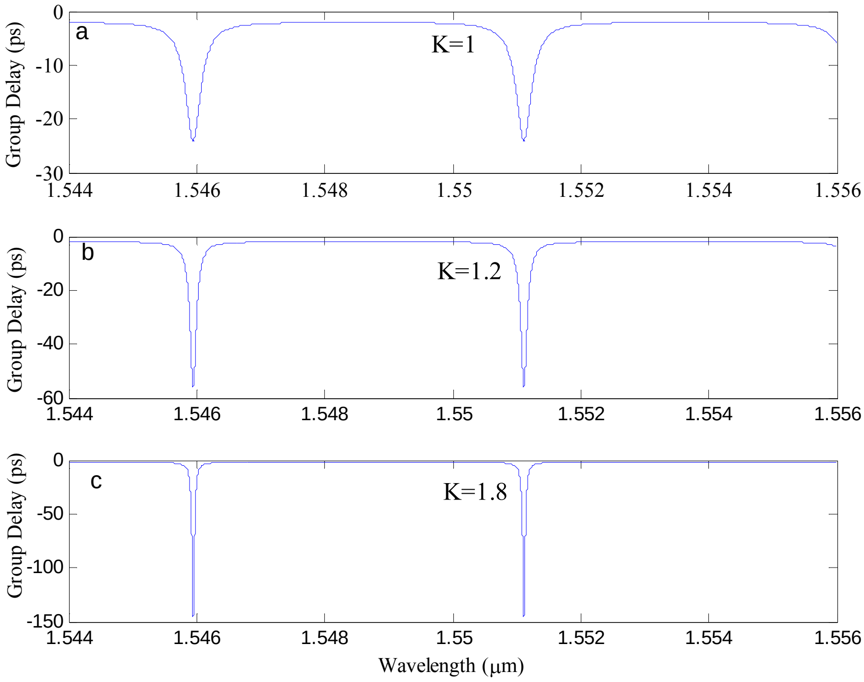

Fig. 7.4: Group delay dependencies on the wavelength in a two-turn uniform ONMR;

(a) *K*=1; (b) *K*=1.2; (c) *K*=1.8.

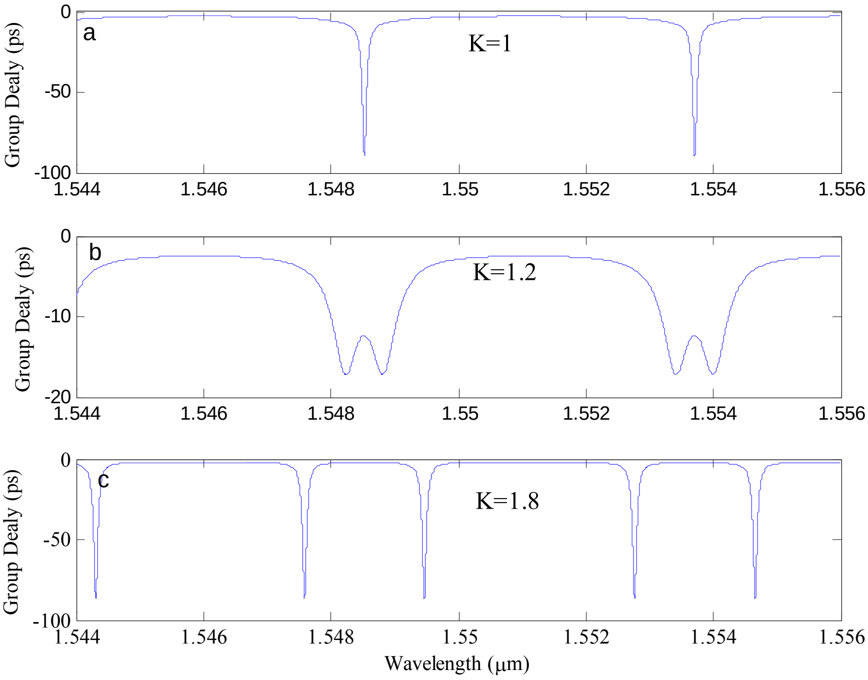

Fig. 7.5: Group delay dependency on the wavelength in a three-turn uniform ONMR; (a) *K*=1; (b) *K*=1.2; (c) *K*=1.8.

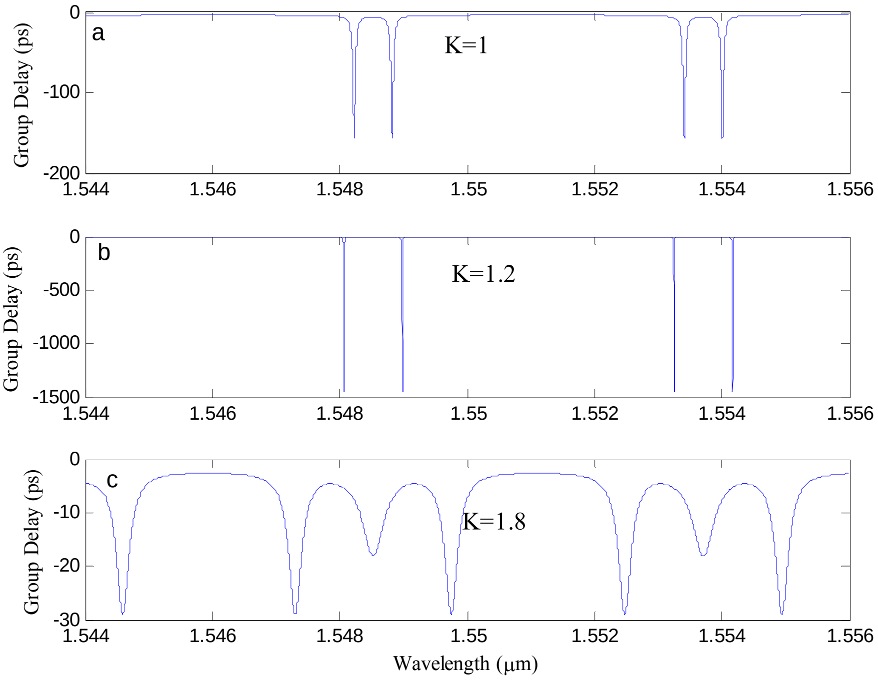

Fig. 7.6: Group delay dependencies on wavelength in a four-turn uniform ONMR;

(a) *K*=1; (b) *K*=1.2; (c) *K*=1.8.

Here $n_f = 1.45$, $R_m = R = 125/2\mu m$, $m = 1,2.......M$; propagation losses are neglected; $\beta R 2\pi$ is approximately 1500 and the coupling parameters *K* are 1, 1.2 and 1.8 respectively. The group delay of ONMRs has a complicated profile apart from the two-turn case which is similar to the ONLR presented in the previous chapter. The resonator peak width is very sensitive to *K*; in Fig7.4, the resonator peak is very narrow at *K*=1.2, similar to the cases *K*=1 and *K*=1.8; In Fig. 7.5, the resonator peak is very wide for *K*=1.2, narrow for *K*=1 and *K*=1.8; In Fig. 7.6, the resonator peak is very wide for *K*=1.8, narrow for *K*=1 and ultra-narrow for *K*=1.2. The relation between the resonator width and *K* will be discussed in details in the next sections.

7.2 Internal Field Distribution in ONMRs

While Section 7.1 discussed the output of uniform ONMRs, in this section the field behaviour inside the resonator is investigated. Non-uniform ONLR with different R_m will also be considered.

Here four simple fundamental profiles are considered (Fig. 7.7)

I: $R_m = R_0$

II: $R_m = R_0 + (\frac{M+1}{2} - m)dR$

III: $R_m = R_0 + \left|(\frac{M+1}{2} - m)\right|dR$

IV: $R_m = R_0 - (-1)^m dR$

$m = 1,2\ldots,M$ and $dR / R_0 << 1$

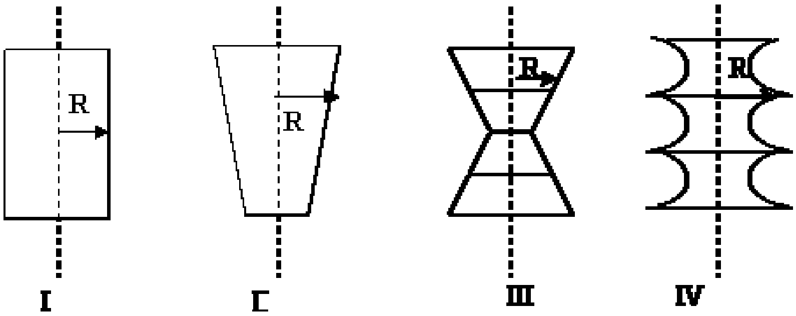

Fig. 7.7: Illustration of four fundamental profiles of ONMRs.

The parameter values used in this section are the same as in last section: the nanowire radius is 1 μm, the fibre index 1.457, the effective index at 1.55 μm $n_{eff} = 1.182$, $R_0 = 125/2\mu m$, $dR = 0.05\mu m$ and the loss 0.0004 dB/m. *K* varies in the range 0—20.

Fig. 7.8 shows the dependence of the normalized transmission for the five-turn ONMR of four kinds of profile on the wavelength. The spectra are complicated and nonperiodic. The resonator peaks have different FWHM. For example, the left peak and the right peak near 1550 nm are different for the profile I when *K*=2.15. In order to compare different profiles with different coupling strength, the minimum FWHM near 1550 nm is taken as the reference for the profile at the corresponding *K*.

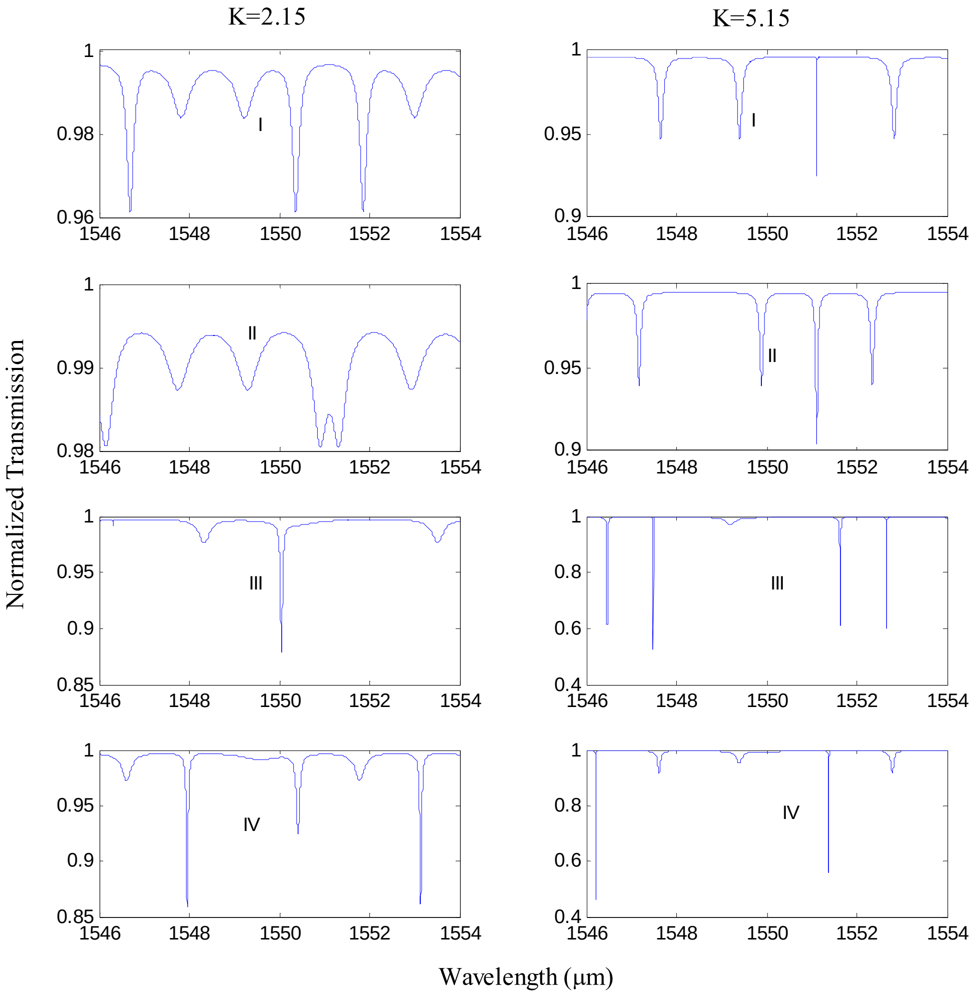

Fig. 7.8: Normalized transmission dependency on wavelength in five-turn ONMRs of four kinds of profiles: I, II, III and IV.

It is interesting to investigate the field behaviour inside the resonator. As an example, the field amplitudes $A_1(\theta), A_2(\theta)$ and $A_3(\theta)$ are calculated (when *M*=3) for the profiles I, II, and III, choosing the wavelength and K which maximize the field amplitude. Fig. 7.9 shows the dependence of the internal maximum field amplitudes distribution on angle (θ) in three coils. The internal field amplitude in I and III are much larger than II, which means more energy can be stored in I and III.

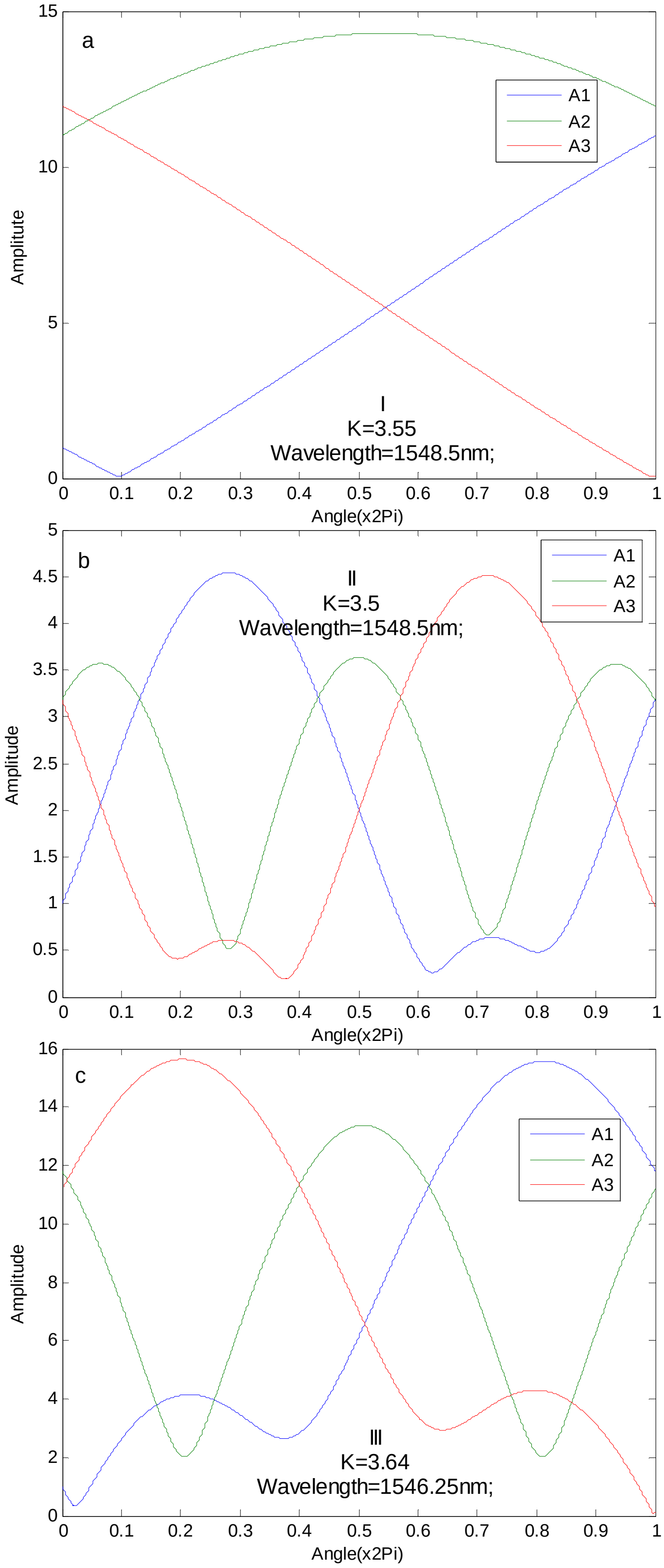

Fig. 7.9: the internal field amplitude in a three-turn ONMR forprofile I (a); profile II (b) and profile III (c). The three profiles are presented in Fig. 7.7.

7.3 Coupling Coefficient

In order to calculate the spectrum of the ONMR, the coupling parameters *K* need to be evaluated. The coupling strength between two turns of the microcoil depends on the nanowire diameter, the distance between the two coils (pitch), and on the choice of the surrounding material (index n_c) which modifies the evanescent field decay length.

So far, microcoil resonators have only been discussed in air (n_c=1). While this is ideal for proof-of-principle demonstrations, the resulting structure is not stable against vibrations and high Q-factors are unlikely to be maintained over long times. Moreover, optical fibre nanowires are known to degrade rapidly in air due to surface contamination/deterioration [4, 5], which introduces large propagation losses over the course of a few days. A far better solution is therefore to embed the microcoil into a low-refractive-index material to provide long-term stability and low loss.

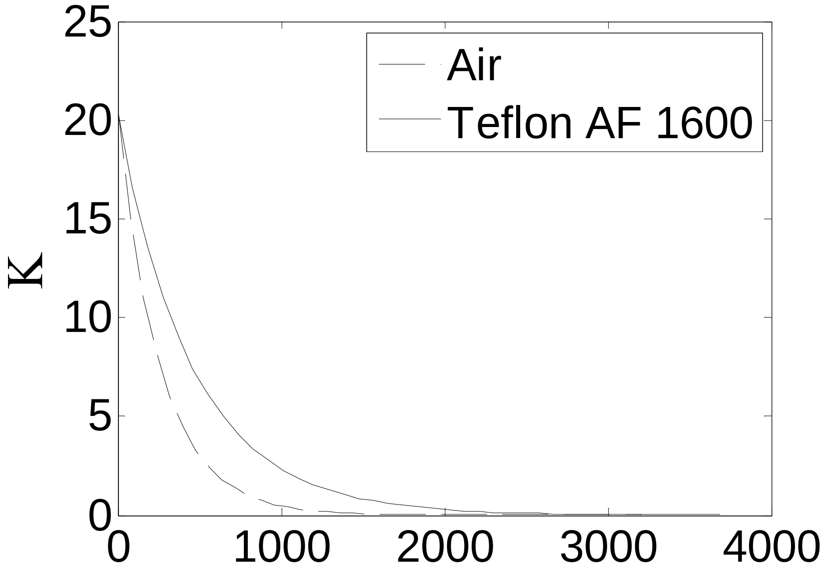

Fig. 7.10: Coupling parameter versus distance between two adjacent nanowires in air and Teflon

The coupling coefficient k_{pq} can be calculated by Eq. (7.1.5). Assuming the diameter of the coil to be 125 μm, the coupling coefficient can be normalized as the coupling parameter K (=125μm×$\kappa_{pq}\pi$). Fig. 7.10 shows the coupling parameter K, at wavelength λ=1550 nm, versus the pitch between two adjacent nanowire coils, for two embedding materials, air (refractive index 1) and Teflon AF1600 (refractive index ~1.3). The nanowire radius here is assumed to be 800 nm for the case of air and 920 nm for Teflon AF1600 in order to achieve the same maximum coupling, of K_{Max}=20, for touching nanowires in the coil. As expected, in the case of a higher refractive index of the surrounding material, the evanescent fields decay more slowly and therefore coupling between nanowires occurs over larger distances.

However, even in the case of an embedding material with a refractive index of 1.3, the coupling is strongly dependent on the nanowire separation which, as already outlined above, renders the fabrication of high-Q ONMRs extremely difficult. Therefore, in the following sections various geometric options will be investigated to attempt to enhance the tolerance of ONMR fabrication to minor fluctuations of the pitch. It has to be emphasized that all results apply equally to all embedding materials, since the calculations only depend on the value of the coupling parameter K.

Additionally, for an ONMR with a nanowire radius of a = 800 nm, as shown in Fig. 7.3, the pitch between the first turn and third turn is larger than 2a. At this distance K_{13} is very small (<0.05) compared to K_{12} because it decreases quickly when the pitch increases, as shown in Fig. 7.10. Hence we can ignore the high order coupling when solving the problems. For example, only the coupling between adjacent turns is considered in Eqs.(7.1.1)-(7.1.10).

7.4 Q-factor and Tolerance Ratio

The Q-factor is one of the most important parameters of a resonator. With K at resonant conditions and no transmission loss, the Q-factor is potentially unlimited, and the FWHM can be arbitrarily small. For the practical case of a nanowire with finite loss, this is evidently not possible. The FWHM has a non-zero minimum and it is related to K and the profile of the ONMR.

The ONMR is a potential high-Q factor device because of the low loss and strong coupling. Hence they are studied here in more details. The Q factor near resonance of a two-turn lossless uniform ONMR can be solved from Eq. (7.2.14) as [1]:

$$Q = \frac{\beta 2\pi R}{(K - K_m)^2} \tag{7.4.1}$$

Generally, the Q-factor for a lossy multi-turn ONMR depends on loss and coupling, similar with Eqs. (7.4.1) and (7.4.2):

$$\text{FWHM} \propto 1/Q \propto \alpha + (K\text{-}K_m)^2, \tag{7.4.2}$$

The response of complicated ONMRs has been solved by numerical simulations in MATLAB. Fig. 7.11 shows the minimum FWHM near 1550 nm at different K for a 3-turn and a 4-turn ONMR with constant diameter $R_m(\theta)=R_0$ and constant coupling. Throughout the discussions of this and the following sections, the average microcoil radius is assumed to be R_0=125/2 μm, propagation loss ~0.02 dB/mm, coupling values in the range K=0...20 and wavelength near 1.55μm. For the figures, it can be seen that the FWHM decreases monotonically with K when K is small (K<1), but fluctuates widely for larger values of K. Thus, in general high Q-factors cannot be obtained simply by increasing K, i.e. by bringing adjacent turns closer together. For M=3 the FWHM profile is nearly periodic in K and close to the minimum at $K=K_{Max}$. For M=4, on the other hand, the FWHM fluctuates in an irregular way and is relatively large at $K=K_{Max}$. More specifically, at $K=K_{Max}$ simulations predict $\Delta\lambda$=0.02 nm for M=3 and 0.25 nm for M=4, respectively. The minimum of the FWHM is ~0.004 nm (as shown in Fig. 7.11) because of the finite propagation loss in the nanowire.

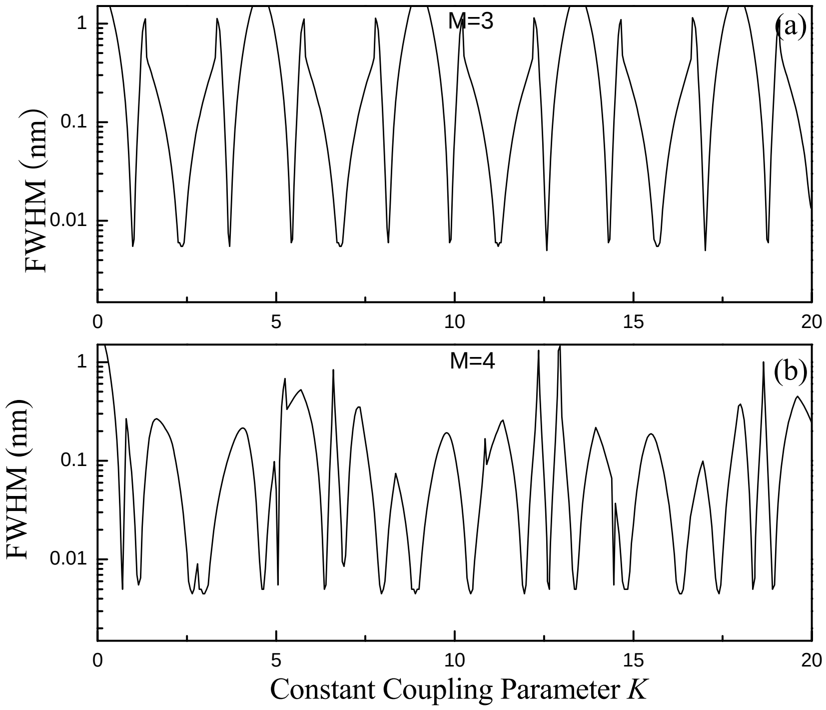

Fig. 7.11: FWHM near 1550 nm at different *K* for a 3-turn and a 4-turn ONMR with constant diameter $R_m(\theta)=R_0$ and constant coupling.

7.5 Optimisation

At present, the lowest resonator losses and thus the highest Q-factors (10^{12}) are achieved with whispering gallery resonators [6]. Recent progress in fabrication technology has led to a significant reduction of nanowire losses [4, 5, 7, 8], such that ONMRs can now potentially reach similar Q-factors. While this is true in theory under ideal conditions, problems arise in practice because of the uncertainty of fabrication conditions, e.g., fluctuations in fiber diameter or spacing. Since the resonant field enhancement in ONMRs happens by the coupling of different rings via their evanescent fields and since these evanescent fields vary strongly with distance, maintaining ideal coupling throughout the entire microcoil requires nanometer fabrication precision.

This section presents a detailed review of various options to enhance the fabrication tolerance of ONMRs by modifying the resonator geometry. In particular, the dependence of the Q-factor of ONMRs on the coupling parameter with variable diameter of turns [9, 10], variable coupling between adjacent turns [10], and variable coupling with the input and output pigtails[10], is investigated.

7.5.1 ONMRs with Nonuniform Diameter

In this section, the effect of different geometries on the FWHM and on the Q-factor of ONMRs is investigated. The coupling coefficient κ is supposed to be independent of θ, i.e., that the pitch between adjacent turns of the coil is constant and thus the coupling parameter K is constant. The radii of the individual turns, on the other hand, are assumed to vary with angle θ and turn index m.

The three simple geometries illustrated in Fig. 7.12 are considered:

- profile H (cylindrical) with constant radius R;

- profile V (conical) with R increasing from bottom to top by dR per turn; and

- profile X (biconical) with increasing R from centre to both ends by dR per turn

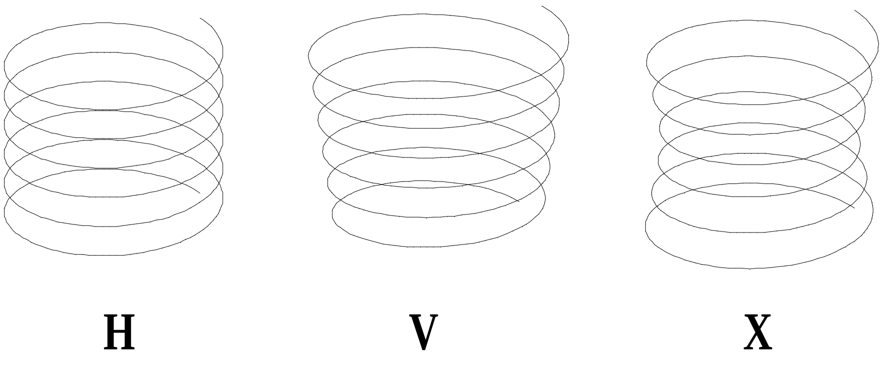

Fig. 7.12: Illustration of three types of fundamental profiles of ONMRs: H (cylindrical), V (conical) and X (biconical).

The mathematical formulation is:

H (Cylindrical):
$$R_m(\theta)=R_0 \tag{7.5.1}$$

V (Conical):
$$R_m(\theta)=R_0+\frac{M}{2}dR+(m-1+\frac{\theta}{2\pi})dR\,, \tag{7.5.2}$$

X (Biconical):
$$R_m(\theta)=R_0+\left|(\frac{M+1}{2}-m-\frac{\theta-\pi}{2\pi})\right|dR-\frac{M}{4}dR\,, \tag{7.5.3}$$

where m=1,2…M, dR/R_0<<1, $|R_{m+1}(\theta)-R_m(\theta)|=dR$ for all m, and dR=0.1 μm.

The FWHM of the transmission peak near 1550 nm for the three profiles has been found numerical using Eqs. (7.2.1)-(7.2.8). The resulting dependence of the FWHM on K is shown in Fig. 7.13 for M=3 and 4. The FWHM decreases monotonically with K when K is small (K<1), but fluctuates widely for larger values of K. For M=3 the FWHM of the H profile is nearly periodic in K and close to the minimum at $K=K_{Max}$. For M=4, on the other hand, the FWHM fluctuates in an irregular way and is relatively large at $K=K_M$. More specifically, at $K=K_{Max}$ simulations predict $\Delta\lambda$=0.02 nm for M=3 and 0.25 nm for M=4, respectively.

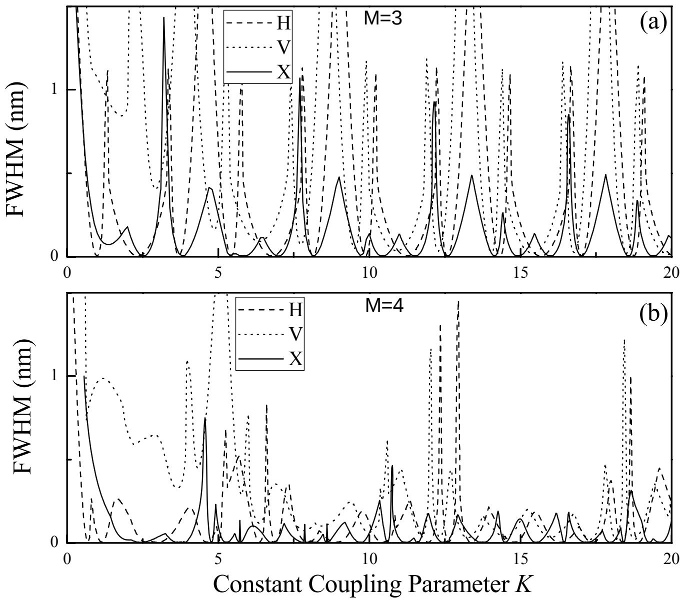

Fig. 7.13: The FWHM dependence on the constant coupling parameter K near λ_0=1550 nm for three geometries: H (dashed lines), V (dotted lines) and X (solid lines) profiles. (a) M=3, (b) M=4.

For most applications it is desirable to maximize the Q-factor of the ONMR. In principle, this can be achieved by selecting a K for which the FWHM is minimized. However, fabrication of the corresponding ONMR is extremely difficult because *K* is enormously sensitive to the distance between adjacent turns. It is therefore preferable to find ONMR geometries and/or coupling profiles for which the FWHM varies slowly with *K*. As shown in Fig. 7.13, an X-shaped resonator has a flatter FWHM than one with profile H, and profile H has a flatter FWHM than profile V. This implies that some geometry may lead to easier fabrication of high-Q resonators than others. In order to compare the different behaviour of the FWHM, the “tolerance ratio” (TR) is introduced, defined as the fraction of *K* values where the FWHM is close to the minimum within a given interval. In practical terms, the tolerance ratio is the probability that an arbitrarily chosen value of *K* will result in an ONMR with near-maximum Q-factor:

$$TR = \frac{\{K \mid Q < 0.01nm\}}{\Delta K} \tag{7.5.4}$$

Specifically, the FWHM threshold is arbitrarily chosen at 0.01 nm in the chosen *K* interval. A large tolerance ratio means FWHM is not so sensitive to K and is therefore an indication for the ease of fabrication of a high-Q resonator. Fig. 7.14 shows the tolerance ratios for ONMRs with *M*=3-9 turns, which are considered a feasible target with the current technology. The tolerance ratios of the H and X profiles increase quickly with *M*. This indicates that high Q-factors are readily achieved by fabricating resonators with as many turns as possible. However this assumes a high degree of accuracy over the entire structure, which is extremely challenging to maintain under practical fabrication conditions. The X profile is the optimal shape and its tolerance ratio is nearly 50% larger than that of the H profile. The V profile is by far the worst geometry, with a tolerance ratio close to zero. Therefore, the X profile provides the largest choice of *K* values to achieve an optimal Q-factor. Moreover, Fig. 7.15 also suggests that ONMRs with more turns (*M*=9 in the figure) provide a very narrow FWHM for essentially any coupling parameter.

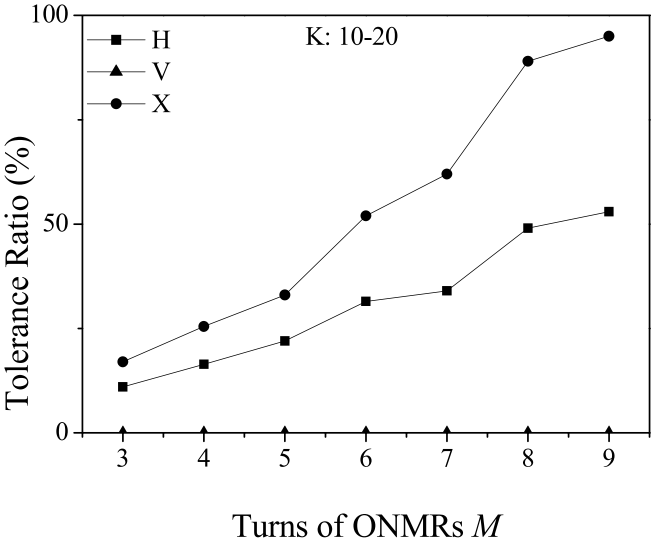

Fig. 7.14: Dependence of the tolerance ratio (defined as the fraction of the average coupling parameter *K* where the FWHM is below 0.01 nm) in the range *K*=10-20 on the number of turns *M* in microcoil resonators for profiles H, V, and X.

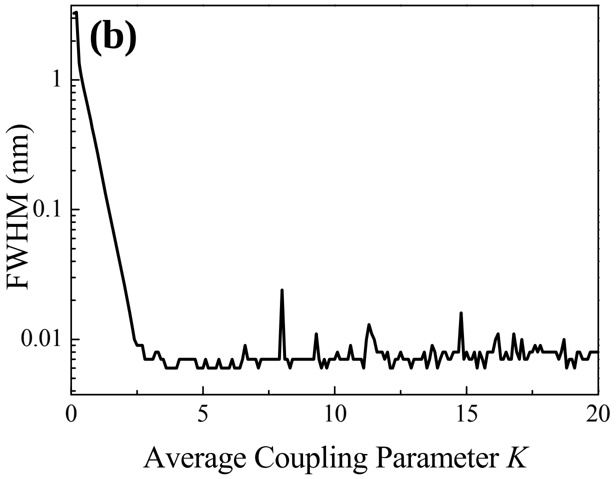

Fig. 7.15: FWHM for *M*=9 and profile X.

7.5.2 ONMRs with Varying Nonuniform Coupling

In Section 7.5.1, the coupling parameter was supposed constant and only the resonator geometry was changed. By contrast, in this section the coupling parameter is varied along the length of the microcoil while keeping the coil radius constant. The fabrication of such ONMRs is expected be even more challenging than the fabrication of ONMRs of varying geometry as described above, since varying the coupling profile requires a controlled and extremely accurate design of the pitch along the length of the ONMR.

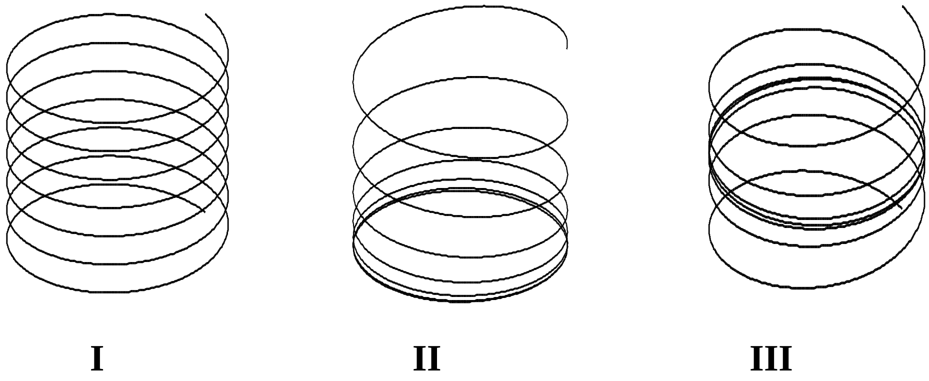

Fig. 7.16: Illustration of the three different coupling profiles.

The three different coupling profiles, illustrated in Fig. 7.16, will be discussed. Profile I is the uniform case with constant coupling, already discussed in Section 7.5.1, profile II exhibits an increasing pitch from the bottom to the top; and profile III has an increasing pitch from the center to the edges. Defining the coupling parameter as:

$$K_{p,p+1}(\theta)=2\pi R_0\kappa_{p,p+1}(\theta), \tag{7.5.5}$$

the three profiles can be expressed as:

I (Uniform): $$K_{pp+1}(\theta)=K_c \tag{7.5.6}$$

II (Linear): $$K_{pp+1}(\theta)=K_c(p-1+\theta/2\pi)/(M-1) \tag{7.5.7}$$

III (Triangle): $$K_{pp+1}(\theta)=K_c\left[1-\left|\frac{(p-1+\theta/2\pi)}{(M-1)/2}-1\right|\right] \qquad (7.5.8)$$

where *p=1,2...M-1* and K_c is the maximum coupling parameter in a special ONMR, different with K_{Max}, which is the coupling parameter when the pitch is zero between two pieces of nanowires.

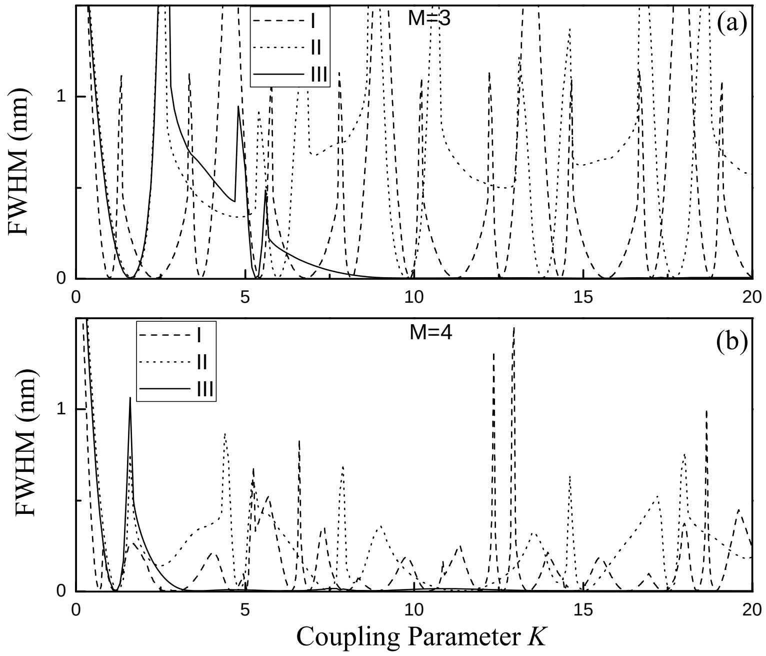

Fig. 7.17: FWHM of the transmission peak near λ_0=1550 nm versus coupling parameter *K* for coupling profiles I (dashed lines), II (dotted lines), and III (solid lines) for (a) *M*=3 and (b) *M*=4. A schematic of the profiles is shown in Fig. 7.17.

As previously discussed, the FWHM of the closest transmission peak to the 1550 nm wavelength is considered. Fig. 7.17 shows the dependence of the FWHM on *K* for the three profiles when *M*=3 and 4. The resonator with shape I has a flatter FWHM than the ones with profile II, and profile III has the flattest FWHM. III also exhibits a FWHM smaller than 0.4nm for all values of *K*>11 for *M*=3 and for *K*>4 for *M*=4. This implies that III is very insensitive to *K*, leading to an easier fabrication of high-Q resonators than the other profiles.

The tolerance ratios of the three coupling profiles for *M*=3-9 are shown in Fig. 7.18. Coupling profiles II and III present a similar behaviour to the geometric profiles V and X discussed in Section 7.5.1. The tolerance ratio is always very large (near 100%) for profile III and very small (<15%) for profile II. Note that limiting the sampling range of *K* can modify the behaviour of the tolerance ratio as observed in Fig. 7.18 for profile III and *K*=16 to 20, where the tolerance ratio is no longer increasing monotonically with *M* but has a marked minimum at *M*=7. The reason for this effect can be seen more clearly on a logarithmic plot of the FWHM versus the coupling parameter, shown in Fig. 7.19. The FWHM fluctuates widely, and thus the tolerance ratios increase monotonically only when the sampling range of *K* is sufficiently large (for example 0-20).

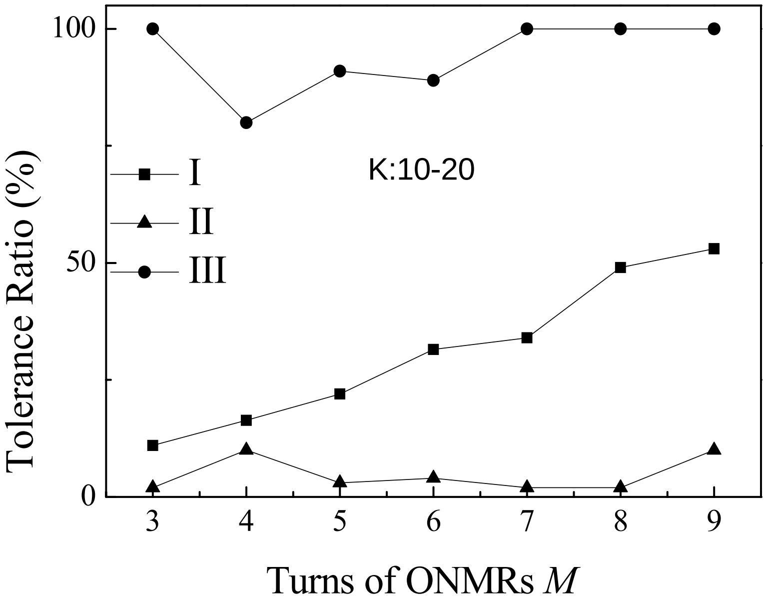

Fig. 7.18: Dependence of the tolerance ratio in the range *K*=10-20 on the number of turns *M* in a microcoil resonator for the different coupling profiles of Fig. 7.16: I (squares), II (triangles), and III (circles).

These results show clearly that high-Q-factor ONMRs can be achieved more easily by a gradual increase of the microcoil pitch from the center towards the two ends. However, the actual fabrication of ONMRs with variable coupling profiles remains a very challenging task with the current technology.

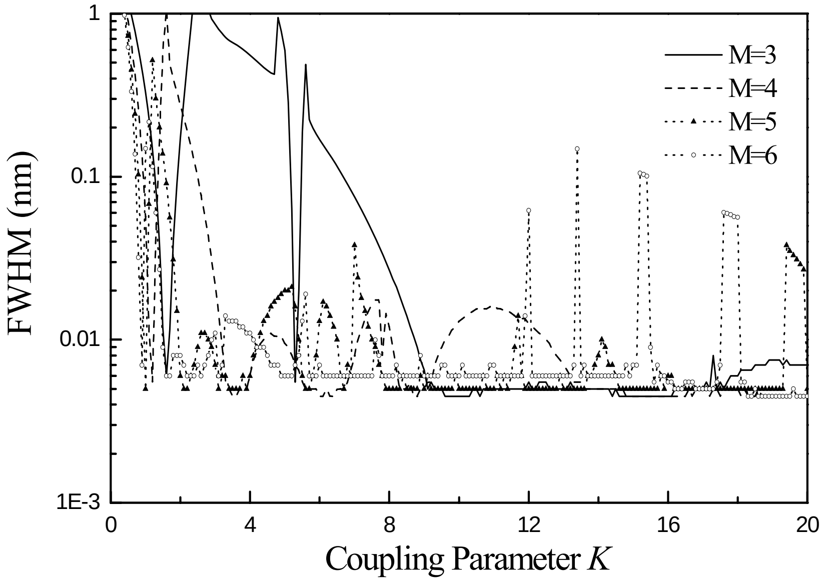

Fig.7.19: FWHM near λ_0=1550 nm versus coupling parameter K_c on a logarithmic scale for the coupling profile III.

7.5.3 ONMRs with Varying Input/Output Coupling

Section 7.5.2 showed that very high TRs can be achieved with coupling profile III where the coupling changes gradually over the length of the microcoil. This is difficult to fabricate with accuracy because of the high spatial precision

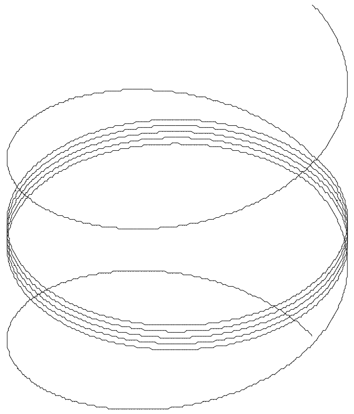

Fig. 7.20: Illustration of an ONMR with uniform diameter, constant coupling of the central turns and varying coupling at both ends.

required. Here a revised and simpler case is investigated, where the coupling changes only at the two ends of the coil but is constant for the turns in between. The coil diameter is again assumed constant. Fig. 7.20 shows a schematic of the corresponding geometry.

For the following, it is convenient to introduce a single coupling parameter $K(\phi)$,

$$\varphi = \theta + (p-1)2\pi \quad \text{for } K_{p,p+1} \tag{7.5.9}$$

$\theta=2\pi\phi=0\text{-}2\pi M$, which describes the coupling along the entire length of the coil and which is piecewise identical to the coupling $K_{m,m+1}$ of the individual rings. In order to conform with the geometry outlined above, $K(\phi)$ fulfils the conditions

$$K(\phi)=K_c \quad \text{for } 2\pi<\phi<2\pi(M-1), \tag{7.5.10}$$

$$K(0)=K(2\pi M)=0, \tag{7.5.11}$$

where K_c is the maximum coupling of the inner rings. This is in fact a generic geometry describing a microcoil resonator of M-2 rings while simultaneously the first and last microcoil turn mimic the coupling of the coil to the input and output fibre pigtails, respectively.

First the special case of M=3 is discussed. In this case, the model describes the system of a single ring with input and output pigtails, i.e., the single-loop resonator discussed in Chapter 6. Fig. 7.21 shows three different profiles for K and the corresponding dependence of the FWHM on the maximum coupling K_c. The main finding here is that in order to obtain a large tolerance ratio, i.e., a flat FWHM, the input and output coupling should decrease slowly. The actual shape of the coupling profile seems to play only a minor role. Fig. 7.22 explores this behaviour in more detail. Here the input coupling is chosen linearly increasing from zero to K_c between $\phi=2\pi x$ and 2π, the output symmetric to the input. TR for these coupling profiles as a function of x decreases from nearly 100% at x=0 (small gradient of K) to 0 for very steep gradients.

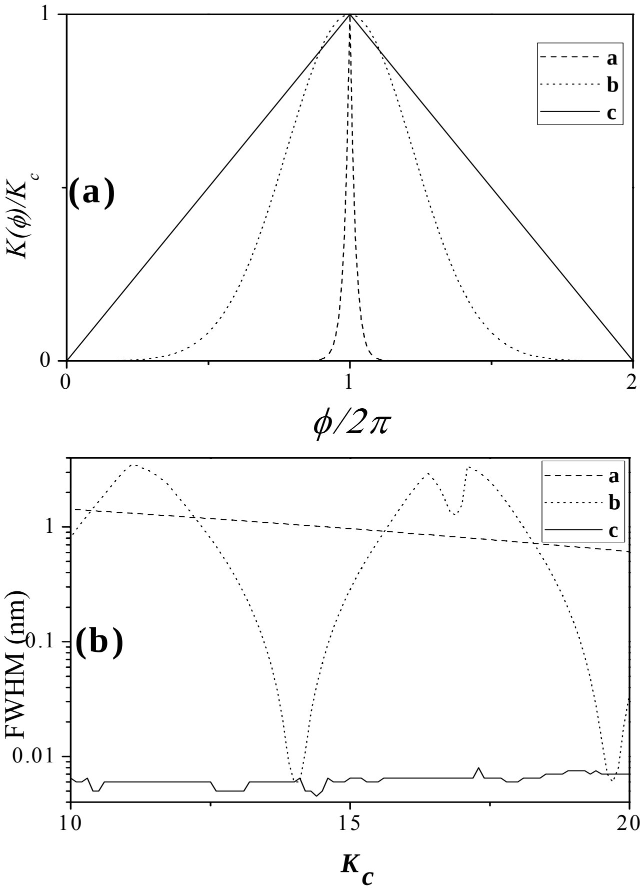

Fig. 7.21: (a) Three different coupling profiles for M=3. (b) Corresponding FWHM versus maximum

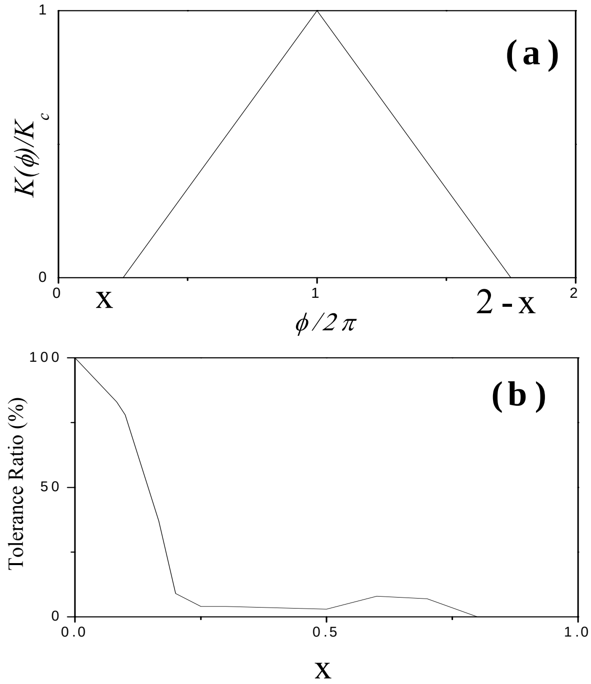

Fig. 7.22: (a) $K(\phi)$ with linearly increasing input coupling between $\phi=2\pi x$ and $\phi=2\pi$ (output coupling symmetric) for M=3. (b) Corresponding tolerance ratio versus x in the range K_c=10-20.

Next, the case of M=4 is investigated, that is, a coil of two central rings with input and output pigtails. Fig. 7.23 shows three different coupling profiles and the corresponding FWHM. As in the case of M=3 it can be noted that small gradients of the input and output coupling parameter lead to narrower resonances over larger ranges of the maximum coupling K_c.

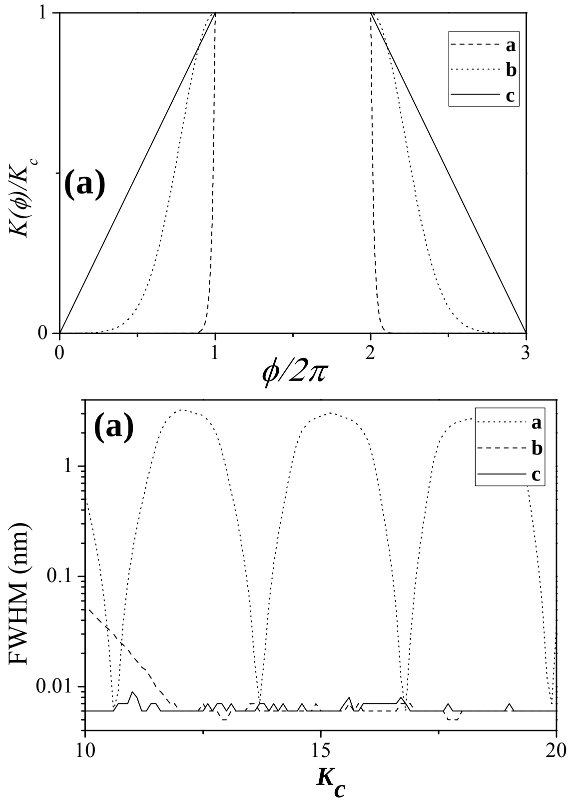

Fig. 7.23: (a) Three different coupling profiles for M=4. (b) Corresponding FWHM versus maximum coupling K_c.

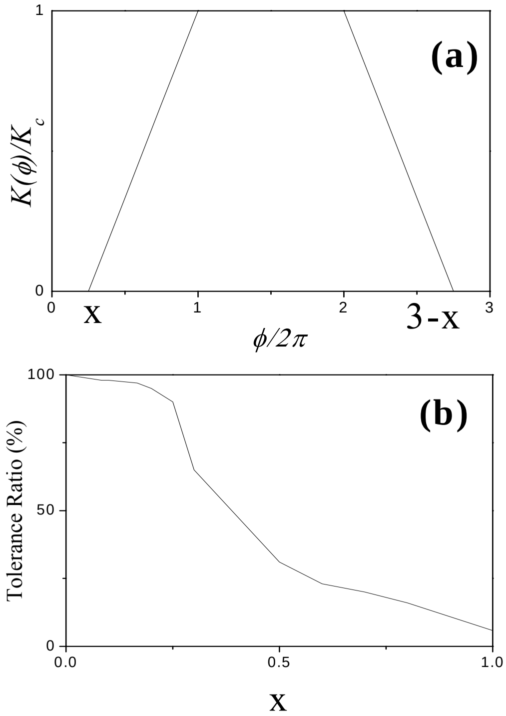

Fig. 7.24: (a) $K(\phi)$ with linearly increasing input coupling between $\phi=2\pi x$ and $\phi=2\pi$ (output coupling symmetric) for $M=4$. (b) Corresponding tolerance ratio versus x in the range $K_c=10\text{-}20$.

Fig. 7.24 depicts TR for varying gradient of the coupling, which shows more clearly that small gradients are preferable. The same trends have been confirmed by more simulations for $M=5, 6, 7$. Fig. 7.25 shows results of the FWHM versus maximum coupling K_c for $M=5, 6, 7$ and $x=0$. TRs are 100% for $M= 5, 6, 7$.

These results for input and output coupling are also consistent with the interpretation given in Section 7.5.1 for the case of varying coupling through the entire microcoil with a symmetric profile. An increase of the coupling in the input/output pigtails with a small gradient ensures that the condition of perfect coupling of light from an outer ring of the coil to an inner ring is met somewhere at the coil ends, thereby producing a low-loss high-quality resonator mode inside the coil.

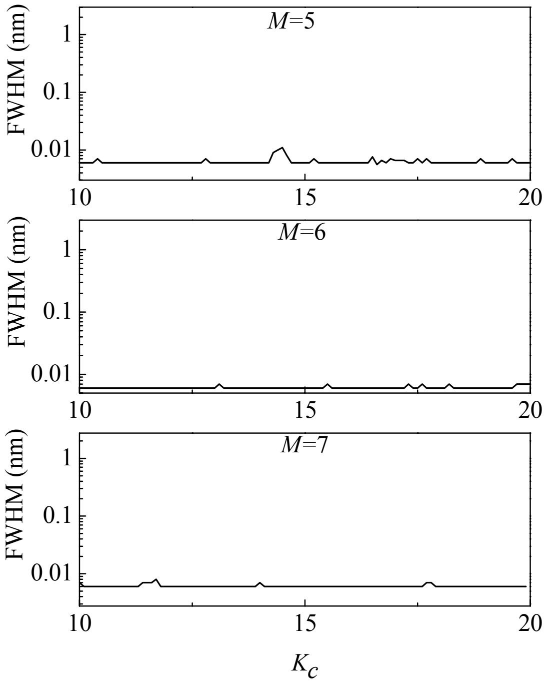

Fig. 7.25: FWHM versus maximum coupling K_c for M=5, 6, 7 and x=0.

7.6 Summary

ONMR has a very flexible structure for many applications, but it is also complex and difficult to manufacture. In particular, the FWHM of a uniform ONMR is very sensitive to K, and K is sensitive to many factors including the environment and the pitch, which leads to the difficulty in manufacturing high Q-factor ONMRs. In this chapter, generalized geometries for the ONMR have been investigated in order to find optimized designs which allow for the fabrication of high-Q resonators with as large fabrication tolerances as possible. This discussion has been based on numerical solutions of coupled wave equations including varying microcoil diameter and varying pitch. To qualify the easiness of fabrications for different profiles, the tolerance ratio was introduced: generally, larger tolerance ratios mean Q-factors more insensitivity to K.

Three possible generalizations of the generic cylindrical microcoil with uniform coupling have been presented and the tolerance ratios were compared respectively.

(i) Section 7.5.1 *ONMRs with non-cylindrical shape but uniform coupling*. Such a design can be realised by wrapping a nanowire around an angled low-refractive index rod. Optimum fabrication tolerances are achieved with a symmetric design where the coil diameter increases from the centre towards the ends of the coil. However, for the best performance, ONMRs with larger numbers of turns are preferred, which imposes additional fabrication difficulties.

(ii) Section 7.5.2 *ONMRs with varying coupling along the entire coil but constant radius*. The best performance is found if the coupling is maximum at the centre of the coil and decreases towards both ends. In this case, high-Q resonators can be obtained for nearly every value of the maximum coupling coefficient even for resonators with only three or four turns. On the other hand, the fabrication of ONMRs with well-defined varying pitch is thought to be a very challenging task.

(iii) Section 7.5.3 *ONMRs with constant radius and constant coupling for the inner turns but coupling continuously decreasing to zero in the first and last turns*. This design can be realized by first fabricating the inner turns with tight pitch, and then micro-tuning the input and output pigtails to obtain the decreasing coupling on the outermost turns. It has been found that very high fabrication tolerances can be achieved with this method, provided that the change of the pitch in the input and output ends of the microcoil is sufficiently slow.

In conclusion, option (iii) represents the most feasible design for high-Q microcoil resonators, combining a readily implemented fabrication technique with large tolerances on spatial accuracy. All of these results apply to ONMRs in air as well as to ONMRs embedded in low refractive index materials which can be used to stabilize the structure and prevent surface contamination/degradation and corresponding increase of propagation loss with time.

7.7 References

1. M. Sumetsky, "Optical fiber microcoil resonator," Optics Express **12**, 2303-2316 (2004).

2. K. Okamoto, *Fundamentals of optical waveguides* (Elsevier, Amsterdam ; Boston, 2006).

3. M. Sumetsky, "Uniform coil optical resonator and waveguide: transmission spectrum, eigenmodes, and dispersion relation," Optics Express **13**, 4331-4340 (2005).

4. G. Brambilla, F. Xu, and X. Feng, "Fabrication of optical fibre nanowires and their optical and mechanical characterisation," Electronics Letters **42**, 517-519 (2006).

5. L. M. Tong, R. R. Gattass, J. B. Ashcom, S. L. He, J. Y. Lou, M. Y. Shen, I. Maxwell, and E. Mazur, "Subwavelength-diameter silica wires for low-loss optical wave guiding," Nature **426**, 816-819 (2003).

6. K. J. Vahala, "Optical microcavities," Nature **424**, 839-846 (2003).

7. G. Brambilla, V. Finazzi, and D. J. Richardson, "Ultra-low-loss optical fiber nanotapers," Optics Express **12**, 2258-2263 (2004).

8. A. M. Clohessy, N. Healy, D. F. Murphy, and C. D. Hussey, "Short low-loss nanowire tapers on singlemode fibres," Electronics Letters **41**, 954-955 (2005).

9. F. Xu, P. Horak, and G. Brambilla, "Conical and biconical ultra-high-Q optical-fiber nanowire microcoil resonator," Applied Optics **46**, 570-573 (2007).

10. F. Xu, P. Horak, and G. Brambilla, "Optimized Design of Microcoil Resonators," Journal of Lightwave Technology **25**, 1561-1567 (2007).

Chapter 8

Manufacture of 3D Microcoil Resonators

In Chapter 7, the theory and optimization of 3D microcoil resonators was presented. In this chapter the manufacture and coating of ONMRs is demonstrated. Because most of experimental demonstrations in this chapter used ~1 μm diameter microfibres, ONMRs in this chapter are referred as Microfibre Coil Resonators (MCRs).

8.1 Manufacture

The microfibre used in the experiments was fabricated using the set-up presented in Section 2.2 and a microheater. The 3D-MCR was manufactured with the set up shown in Fig. 8.1. The microfibre had its pigtails connected to an EDFA and an OSA to check, in real time, the resonator properties during fabrication;

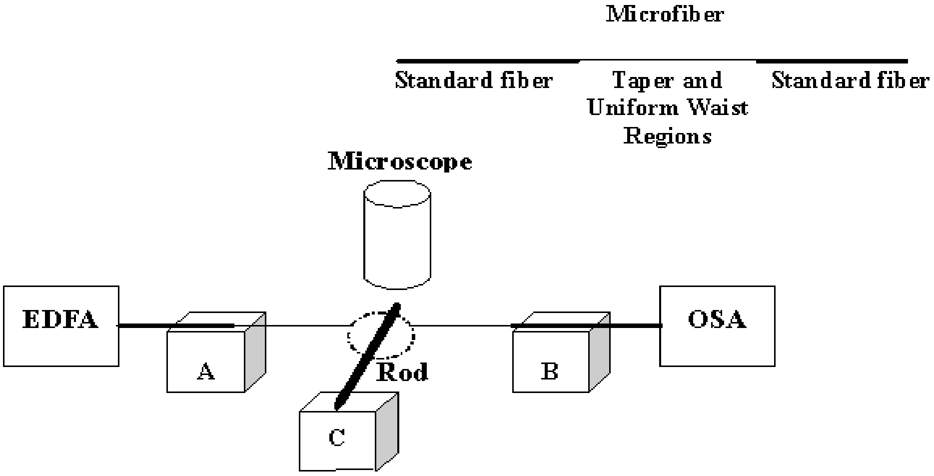

Fig. 8.1: Set up used to manufacture 3D MCR. A, B and C are XYZ stages.

then, with the aid of a microscope, the microfibre was wrapped on a low refractive index rod while one of its ends was fixed on a 3D stage; this process was carried out manually and the close positioning of the microfibre coils resulted from a combination of manually applied longitudinal tension (which kept the relative position of the coils and avoided considerable overlapping) and gravity (which translated vertically the new formed coil until it touched the coil beneath). Finally the other microfibre end was fixed to another 3D stage and both microfibre ends were moved little by little to find the optimum resonator spectrum. This methodology is similar to that theoretically predicted for the design optimization of 3D microcoil resonators presented in Section 7.5. Because the coupling coefficient between two adjacent microfibres is small, the microfibres need to be kept as close as possible.

In these experiments, the MCR was wrapped on a rod to maximize the MCR temporal stability and robustness. For microfibres with large evanescent fields or rods with high indices, it is possible that there are additional losses arising from the leakage loss because the fundamental mode becomes a leaky mode. If the loss is too high, it is difficult to optimize the microfibre position and MCR geometry. Generally, the loss can be minimized by increasing the microfibre thickness and the rod diameter, by using a low refractive index material for the rod and by improving smoothness of the rod surface. In these experiments a rod was coated with Teflon @AF (DuPont, United States), to provide a low refractive index (n~1.3 at λ~1.55 μm) at the interface with the microfibre. The coating thickness is about tens of micrometers.

8.2 Geometry and Spectrum

Fig. 8.2 shows the pictures of a two-turn, three-turn and four-turn MCR made from the same microfibre. The microfibre radius and the length of the uniform waist region were ~1.5 μm and ~ 4 mm respectively. The diameter of the rod is ~ 560 μm. The manual fabrication of the MCR means that the pitches between adjacent turns are nonuniform and the microfibre coils present some degree of twist.

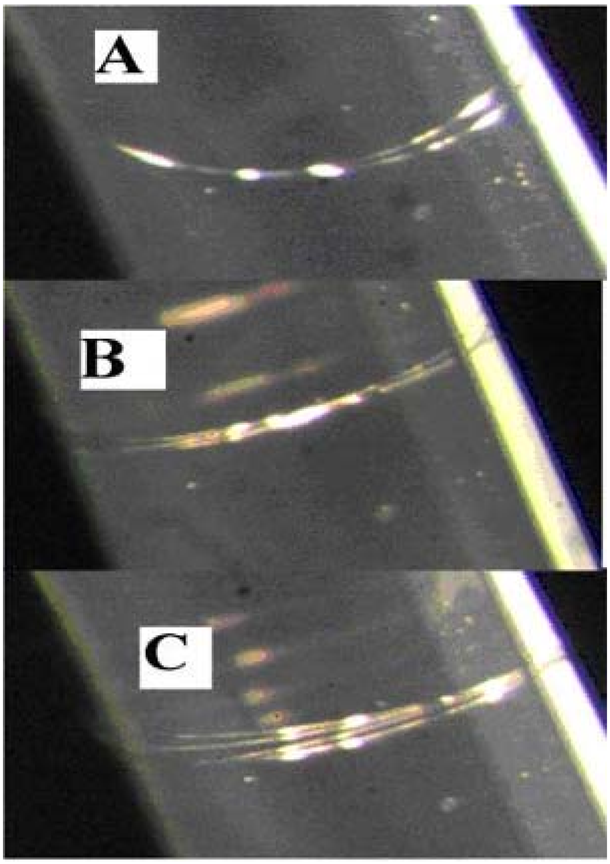

Fig. 8.2: Pictures of MCRs. The number of turns in the MCR is two in (A), three in (B) and four in (C).

Fig. 8.3 shows the resonator spectra of a straight microfibre not in contact with the rod, and of the three MCRs. The spectra in Fig. 8.3A-C show a complicated profile because the coupling among the three or four turns is irregular and non- uniform. The maximum extinction ratios for the two-, three- and four-turn MCR are 3 dB, 10 dB and 9.5 dB respectively. While the spectrum of the two-turn MCR is simple, with a free spectral range (FSR) of 0.86 nm, the spectra of three- and four-turns MCR show a complex profile. In particular, the spectrum of the three-turn MCR can be analyzed as a combination of two resonator modes (labelled ① and ② in Fig. 3B), with the same FSR (about 0.94 nm). There are two possible explanations for this double peak, which will be discussed later respectively: 1) they are generated by X-polarized and Y-polarized modes [1], or 2) they arise from two different resonators. The four-turn MCR (Fig. 8.3C) has an even more complicated spectrum, with three set of peaks: ① (3 dB), ② (~6 dB) and ③ (9.5 dB). As in the previous case, these groups of peaks can arise from different resonators or from a combination of two modes (X-polarization and Y-polarization modes) with the same FSR=0.93 nm: ① and ②+③. These modes are compatible with the complicated resonator structure.

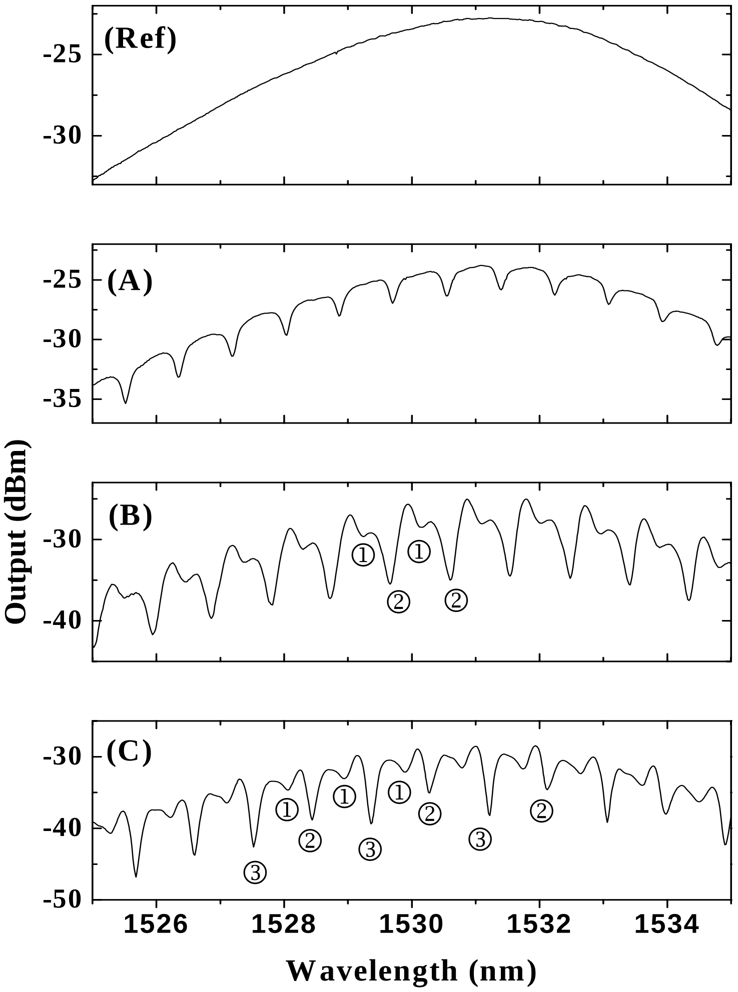

Fig. 8.3: Spectra of MCR with (A) two turns (B) three turns (C) four turns. The top spectrum represents the reference obtained for a free-standing microfiber.

The loss induced by wrapping the microfibre on the rod for the two-, three- and four-turn MCR was ~1 dB, 2.5 dB and 5 dB respectively, which come from the output difference of Figs. (A)-(C) and Ref in Fig. 8.3. The loss is possibly induced by surface roughness, mode discontinuities at the point of input/output, and leaky modes associated with the rod. The largest Q-factor obtained is about 10,000, which is lower than that achieved with an MCR immersed in a liquid [2]; this can be possibly explained by the small coupling strength associated to the short coupling length (here we define the coupling length as the length where two adjacent turns are touching together) and thick microfibre or by the additional loss at the microfibre/rod interface.

Although the pitches between the adjacent coils are not constant, the FSR can still be estimated using the theory presented in Section 6.5. The solution of coupled equations for a multi-turn MCR implies that the resonator condition and FSR can be written as:

$$2\pi n_{eff}/\lambda=(2p\pm 1/2)\pi \tag{8.2.1}$$

$$\text{FSR} \approx \frac{\lambda^2}{n_{eff}L} \tag{8.2.2}$$

where p is an integer, λ the wavelength, n_{eff} the effective index of the mode propagating in the microfibre and L the loop length. n_{eff} was calculated using the finite element method.

The finite element method is a method for solving partial differential equations (PDEs). The method requires the discrimination of the domain into sub-regions or cells. For example a two-dimensional domain can be divided and approximated by a set of triangles (the cells). On each cell the function is approximated by a characteristic form. The method is applicable to a wide range of physical and engineering problems, provided it can be expressed as a PDE. In this thesis, the commercial FEM software COMSOL was used.

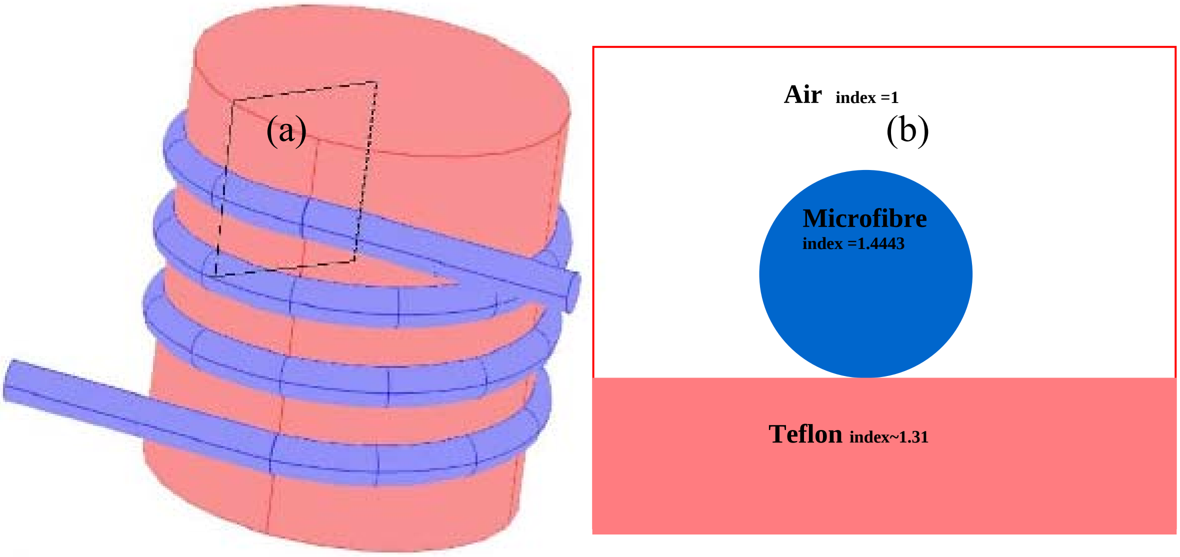

Fig. 8.4: (a) Illustration of a multiple-turn MCR. (b) Cross-section of the selected area in (a).

The cross-section of the microfibre wrapped on the rod is shown in Fig. 8.4; here the rod is assumed to be a Teflon rod because of the thick Teflon coating layer on the surface. The fundamental mode effective index given by COMSOL is ~1.4021. Eqs. (8.2.1)-(8.2.2) show that the resonating mode is expected to have FSR~1nm which is in good agreement with the experimental results. The small difference between the theoretical prediction and the experiments could arise from a real optical path longer than L, because the microfibre and coil diameters present some irregularity and the microcoil position is not always perpendicular to the rod.

For Fig. 8.3B, using Eq. (8.2.1) and the effective index difference between X- and Y- polarized modes, the difference between the resonator wavelengths of X- and Y- polarized modes can be estimated to be about 0.44 nm, which is similar with the 0.48 nm difference observed in Fig. 8.3B. It is therefore possible to ascribe the two types of peak to X- and Y-polarized modes.

Fitting the experiment results by the theory of ONMRs is very difficult (especially for Fig. 8.3B and Fig. 8.3C) because the coupling profile is very complicated. Simplified, Fig. 8.3A, Fig. 8.3B and Fig. 8.3C can be fitted by combining one, two and three simple resonators using Eq. (6.2.1), respectively.

The fitted results are shown in Fig. 8.5. Here the spectra of Fig. 8.3 were normalised by subtracting the reference spectrum. In Fig. 8.5A, the spectrum of the two-turn MCR for spectrum Fig. 8.3A was fitted by using the coupling parameter 0.663 and loss ~0.0616dB/mm. Fig. 8.5B shows the fit of the spectrum of the three-turn MCR (Fig. 8.3A) with the coupling parameter 0.17 for ① and 0.4 for ②, and loss ~0.289 dB/mm. Finally, Fig. 8.5C shows the fitting of the spectrum of the four-turn MCR (Fig. 8.3C) with coupling parameters 0.3 for ①, 0.7 for ② and 0.87 for ③, and loss ~0.13 dB/mm. The discrepancies between fit and experimental values (especially in spectrum B and C) can be attributed to the complicated coupling profiles and non-uniform diameters of microfibre and coil. The well fitted results suggest that it is more possible that the peaks come from two or three resonators in the two- or three- turn MCRs.

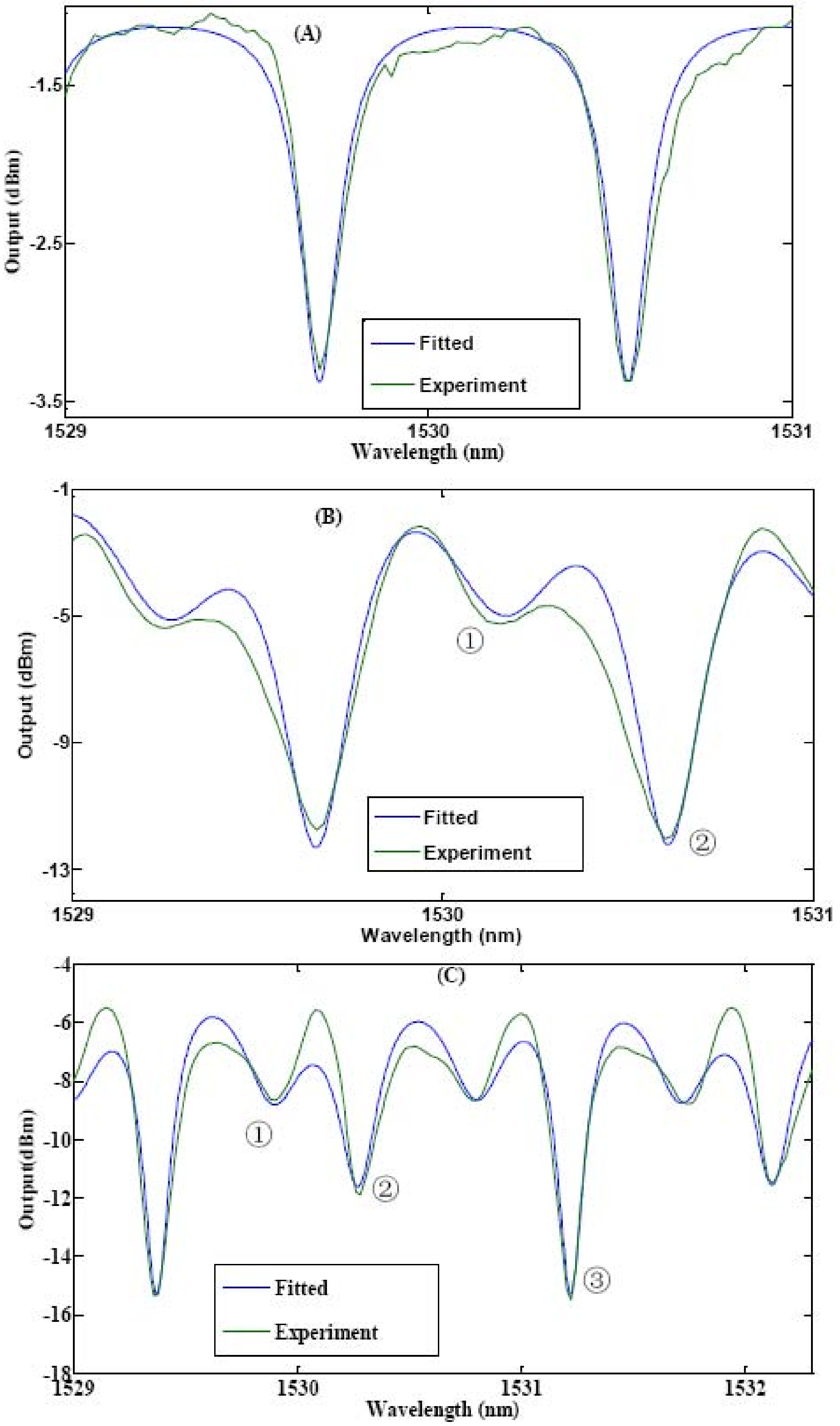

Fig. 8.5: Fitted results of spectra for the (A) two-turn, (B) three-turn, (C) four-turn MCRs in Fig. 8.3.

For practical reasons it is impossible to see the entire circumference of the microfibre coil, thus there are regions where the coils might overlap or their pitch increase. It is possible to tune the coupling by moving the pigtails position: moving slightly the two ends of the fibre up or down only changes the coupling area near the input and output ends without changing the coupling between inner turns. It is interesting to investigate this effect on the spectrum. Fig 8.6 shows the changes in the MCR spectrum of a three-turn MCR, similar to the one presented in Fig. 8.3B, when the pigtails are moved.

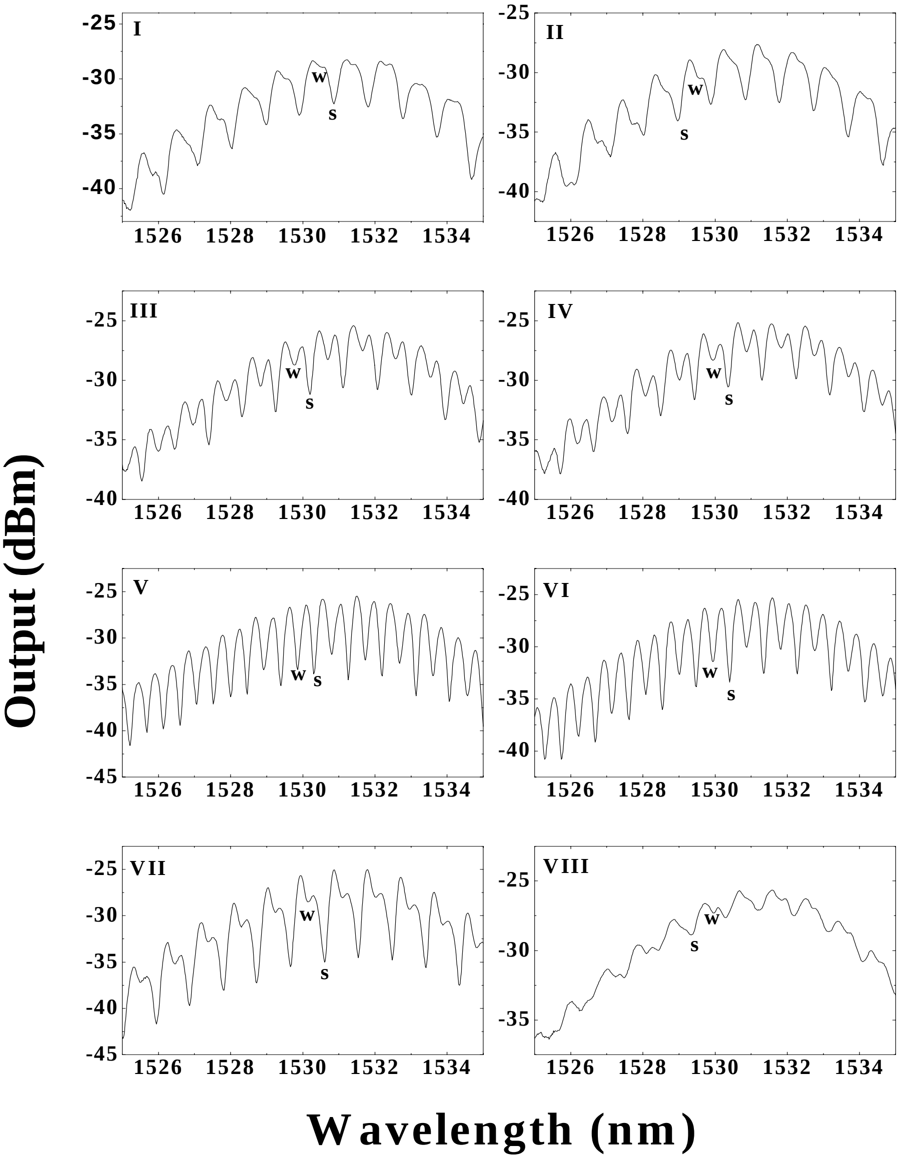

Fig. 8.6: Spectrum of the three-turn MCR during the pigtails tuning.

There are two resonator modes (identified with S and W) at any time. W is very weak in (I), increases from (II) to (V), where it achieves a maximum, and then decreases; S changes little from (I)-(VII). It is suggested that S arises from the coupling between inner coils, so it changes a little when the pigtails are moved, while W is the product of the coupling at the extremities of the MCR, therefore it changes considerably when the pigtails are moved. Both W and S decrease considerably at (VIII), probably because the degree of moving of the pigtails is excessive and the coupling region is considerably reduced. This result also proves the possibility of a second explanation for this double peak in Fig. 8.3B.

8.3 Embedding MCRs in Teflon

Although the structure of a MCR wrapped on a rod is stable in air, sub-micrometric wires experience ageing when exposed to air for some days (section 4.3); moreover, the MCR is not portable and can be easily damaged. For example, a demonstration of a MCR was recently reported for a microfibre immersed in a refractive index matching liquid [2]; still, the extinction ratio was smaller than 1.5dB, and the device was not portable. The embedding of a MCR in a low refractive index medium seems the best method to solve the reliability issues as it provides both protection from fast aging and geometrical and optical stability. Additionally, coated MCR wrapped on a rod makes the fabrication of high sensitivity biosensors possible (Chapter 9). In this section the manufacture of an embedded multicoil MCR is experimentally demonstrated.

The MCR was manufactured by wrapping a microfibre on a rod having a low refractive index with the same set-up as in section 8.1. The microfibre radius and the length of the uniform waist region were ~1.5 μm and 3.5 mm respectively. The rod had three layers: the inner core is a multimode silica optical fibre which provides rigidity to the structure; the intermediate layer consists of a coating polymer (Efiron UV373, manufactured by Luvantix, South Korea), which has a low refractive index (n~1.37 at λ~1.55 μm); the outer layer is a thin Teflon fluoropolymer resin coating, which has an extremely low-refractive-index (n~1.3 at λ~1.55 μm) and provides a uniform refractive index surrounding to the microfibre. The rod has a total diameter D~700 μm, with silica core of radius ~200μm.

The embedded structure was manufactured as follows: at first, with the aid of a microscope, the microfibre was wrapped on the rod, then the Teflon suspension was dropped onto the microfiber and the solvent was evaporated. Fig. 8.7a shows the three-turn MCR prior to the embedding process: the main coupling region is between the lower two turns on the right, even though there are also some small coupling regions on the opposite side of the rod. Because of the large refractive index difference between the silica microfibre and Teflon, the loss observed during the MCR fabrication was negligible. Indeed, this structure was also unaffected by air turbulences and preserved all the benefits of the self-touching loop resonator.

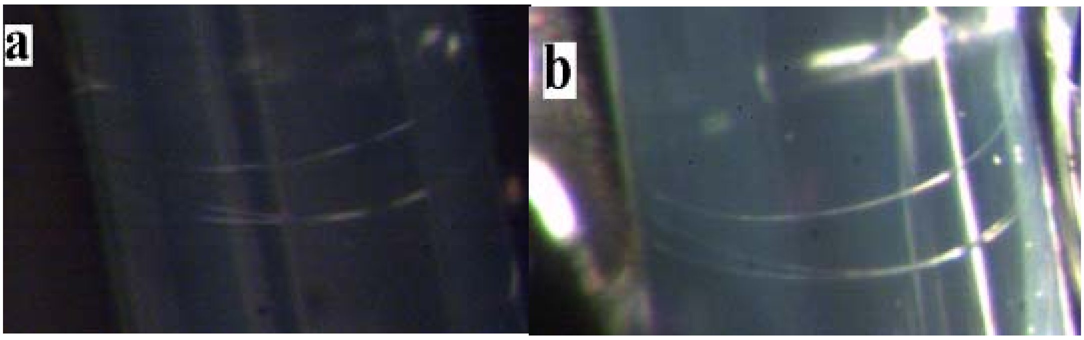

Fig. 8.7: Microscope picture of an MCR wrapped on a rod and embedded in Teflon. The microfibre and rod radii are 1.5 μm and 350 μm respectively.

The microfibre had its pigtails connected to an EDFA and an OSA to check, in real time, the resonator properties during fabrication and embedding. The MCR transmission spectrum in the wavelength interval 1525-1535 nm is shown in Fig. 8.8a: the overall resonances extinction ratio is about 7 dB.

The resonator embedding was carried out with the use of the 601S1-100-6 solution of Teflon® AF amorphous fluoropolymer resin (DuPont, United States), introduced in Section 4.4. The structure was repeatedly covered with Teflon solution on a Teflon-coated substrate, and the solvent was allowed to evaporate.

The coupling process is extremely challenging because the solution reduces the effect of surface forces and if the microfibre is not tightly wrapped around the rod the resonator conditions are lost. Moreover, because of the rapid solvent evaporation, there is a constant solvent flow around the microfibre and Teflon particles and air bubbles move rapidly in the solution. In this situation a collision with the microfibre (especially with its pigtails) can displace the microfibre and change the MCR transmission properties unexpectedly. This reason makes the coating process of the self-coupling loop resonator with Teflon@AF solution challenging. Particular care has also to be taken to avoid any particle contamination into the solution because contaminants eventually come into contact with the microfibre and significantly alter its overall loss.

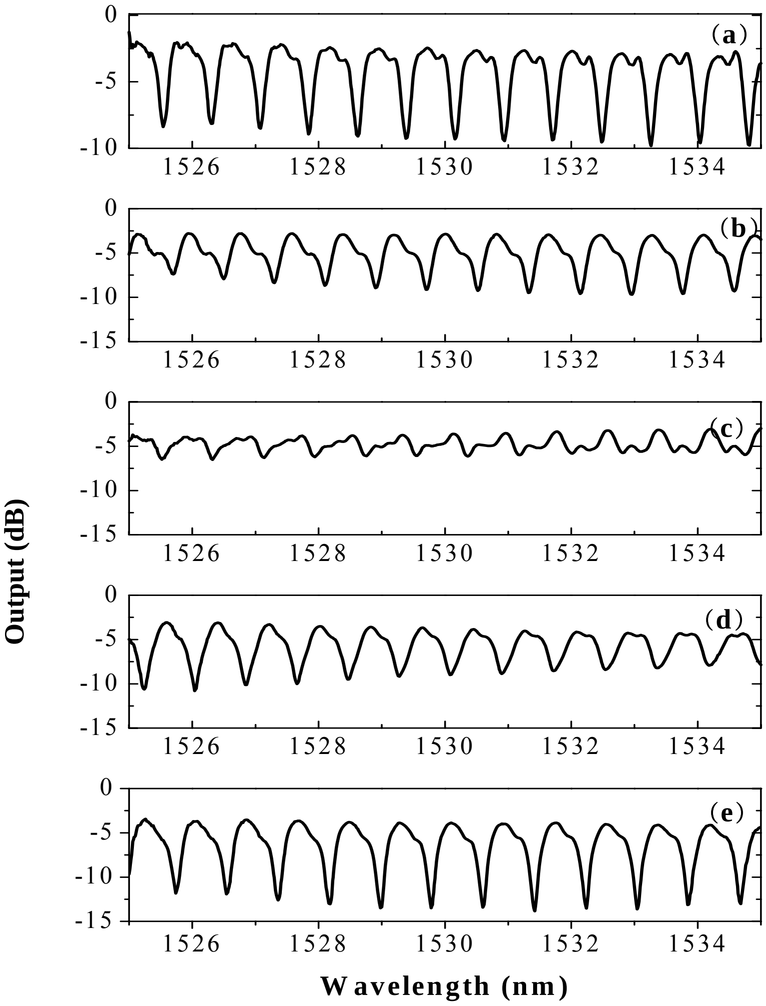

Fig. 8.8: Spectra of MCR recorded within 20 minutes during the embedding in Teflon. In (a) MCR rests in air; in (b)-(d) it is immersed in Teflon suspension, in (e) it is completely covered by dried Teflon.

The picture of the MCR after its embedding in Teflon is shown in Fig. 8.7b Coating with Teflon provides a smooth surface and a homogeneous medium. Although some sporadic bubbles are observed in the polymer, their effect on the MCR is negligible because none of them is in proximity of the microfibre. Fig. 8.8 shows the resonator spectra of the MCR (minus the spectrum of the unwrapped microfibre) before and after adding Teflon solutions. Fig. 8.8a shows the spectrum of the MCR in air before embedding; Fig. 8.8b-8.8d show the spectra taken during the solvent evaporation from the Teflon solution. The MCR spectrum changes quickly and randomly in the first moments after the addition of the Teflon solution, because of the large volume of solvent that frantically drags particles and air bubbles in the proximity of the microcoil, and then it gradually stabilizes when the solvent is completely evaporated and a dry layer of Teflon is deposited, as shown in Fig. 8.8e. The average coating time is about 20 minutes and this depends on the volume and concentration of the solution and temperature. A comparison between the spectra in Fig. 8.8a and 8.8e shows that a small shift to longer wavelengths and an increase in the resonance attenuation (from ~7 dB to ~9 dB) occurred. The increase of the resonance attenuation as a consequence of the embedding process can be explained by an increase in coupling: Teflon has a refractive index closer to that of silica than air, implying that when the microfibre is embedded the mode propagating in the microfibre has a bigger fraction of intensity in the evanescent field, therefore the possibility to experience a stronger coupling.

It is important to note that the spectra shape of the MCR in Fig. 8.8 is different, with respect to that of a simple self-touching loop resonator, because in this latter case the coupling is limited to a single coupling between two sections while the three turns MCR is a 3D microcoil resonator. As discussed in section 8.2, Fig. 8.8 can be taken as the combination of two simple resonators, one of which is dominating the spectrum. The ripples in Fig. 8.8a are possibly due to another coupling area, which is very weak and becomes negligible after embedding, as shown in Fig. 8.8e.

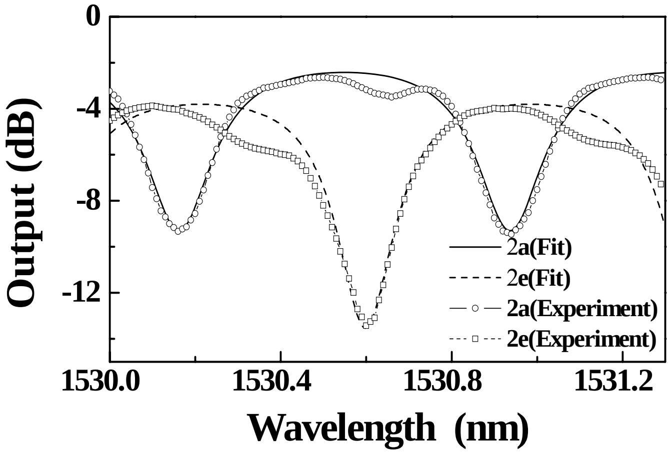

Fig. 8.9: Expanded view of the spectra presented in air (Fig. 8.8a) and embedded (Fig. 8.8e). The fit was carried out using Eq. (6.3.2).

The simple ring resonator model was used to describe the manufactured MCR as discussed in Section 5.2. The resonating condition and the free spectral range can be solved by Eqs. (8.2.1) and (8.2.2). This model predicts FSR~0.8 nm for both the microfibre in air and embedded in Teflon, in good agreement with the experimental results. The FSR depends on the diameter of the rod, which is easy to control, in contrast with the self-touching loop resonators in air. Additionally, the transmission formula of a simple loop resonator Eq. (6.2.1) was used to fit the spectra in Fig. 8.8a and 8.8e and the results are presented in Fig. 8.9. The coupling parameter and loss were 0.46 and ~0.6 dB/mm for spectrum Fig. 8.8a, and 0.53 and ~0.69 dB/mm for spectrum 8.8e. The coupling length was about ~150 μm, in good agreement with Fig. 8.8. The discrepancies between fit and experimental values at 1530.6 nm in spectrum (a) and at 1530.3 nm and 1531.1 nm in spectrum (e) can be attributed to the presence of an additional resonator with small strength and similar coupling length. It should be noted that the MCR properties have been only marginally affected by the embedding process and the overall loss increased only by ~15%.

8.4 Summary

In this chapter, multi-turn MCRs were demonstrated experimentally, and were coated with Teflon. This kind of device is stable, portable, strong, and suitable to be used for practical applications. One of the most important parameters of a resonator is the Q-factor. From Eq. (7.4.3), for simple ring-resonators and microcoil-resonators, the Q-factor depends on the loss and the coupling parameter, which depends on coupling coefficient and coupling length. For the most weakly-coupling cases, longer coupling lengths mean larger K and higher Q at the same loss. In these experiments, the embedded MCR has a Q-factor greater than 6000. Recently, a MCR was reported with Q-factor of 61000 in low refractive index liquid [2]. The Q factor of the resonator presented in this paper is low because of the high microfibre loss (~0.6 dB/mm) induced by the wrapping process. By using precisely controllable rotation and translation stages in a controlled environment all-coupling resonators (where the coupling length coincides with the loop length) with ultrahigh-Q factors should be obtainable. If then a disposable material is used for the rod, this can be dissolved after embedding, leaving a sensor with an intrinsic channel. This will be shown to exhibit very high sensitivity and low detection limits in Chapter 9.

8.5 References

1. M. Sumetsky, Y. Dulashko, J. M. Fini, A. Hale, and D. J. DiGiovanni, "The microfiber loop resonator: Theory, experiment, and application," Journal of Lightwave Technology **24**, 242-250 (2006).

2. M. Sumetsky, "Demonstration of a multi-turn microfiber coil resonator," in *Optical Fiber Communication Conference*(San Diego, USA, 2007).

Chapter 9

Sensors Based on Microfibre Resonators

In the past few years, evanescent-field-based optical resonators in the form of microspheres, photonic crystals, and microrings have been under intensive investigation for deployment as biological and/or chemical sensors [1-5]. For these applications, small size, high sensitivity, high selectivity, and low detection limits are the dominant requirements. Optical microresonators meet all these criteria, in particular they can provide large evanescent fields for high sensitivity, high Q-factors for low detection limits, and corresponding small resonant bandwidths for good wavelength selectivity. The drawback that all high-Q resonators present relates to the difficulty of coupling light into and out of the resonator. Optical nanowires with low cost, low loss and very large evanescent fields are ideal sensor elements, and can be exploited in high-Q microresonators such as loops (Chapter 6) or 3D (Chapter 7 and 8) microcoils. These microresonators do not exhibit the input/output coupling problems experienced in other high-Q resonators because the fibre pigtails at the extremities of the resonator launch and collect the totality of the light. However, in free space the fabrication of these devices with high reliability is challenging due to problems of stability, degradation, and cleanness. Coating is an elegant way to solve these issues (Chapter 8); yet, the determination of the coating thickness is a challenge because a thick coating layer will limit the sensitive evanescent field, while a thin layer does not provide an appropriate protection to the device. In this chapter, the possibility to exploit coated nanowire resonators for sensing applications is investigated.

Two sensing approaches are most commonly used: homogeneous sensing and surface sensing [6]. In homogeneous sensing, the device is typically surrounded by an analyte solution, which can be regarded as the top cladding of the waveguide. The homogeneously distributed analyte in the solution will modify the bulk refractive index of the solution. In surface sensing, the optical device is pretreated to have receptors or binding sites on the sensor surfaces, which can selectively bind the specific analyte [6]. In this chapter we only discuss the conceptually simpler case of homogeneous sensing. Currently, a lot of novel refractometric sensors have been reported using microsphere, microring, fibre gratings etc. [1, 3, 5, 7-12]. The sensitivities are in a wide range from several nm/RIU to 10000 nm/RIU (RIU is the refractive index unit). High sensitivity is preferred, but other parameter such as detection limit (defined as the smallest detectable refractive index change of analyte) has to be considered, too. In this chapter, refractometric sensors based on a coated microfibre loop resonator and a coil resonator are presented and their performance is investigated as a function of the geometry (in particular, the microfibre diameter and the coating thickness). The detection limit is discussed, too.

Finally, a sensor based on microfibre coil resonator is demonstrated experimentally.

9.1 Sensor Based on Microfibre Coil Resonator

9.1.1 Sensor Schematic and Manufacture

A coated microfibre coil resonator sensor (CMCRS) can be fabricated as follows: firstly, an expendable rod is initially coated with a layer of thickness *d* of a low-loss polymer such as Teflon, the rod is made from disposable materials such as PMMA (PolyMethylMethAcrylate), which is a polymer with an amorphous structure and is soluble in Acetone; then an optical microfibre is wrapped on the rod as explained in Chapter 8; next, the whole structure is coated with the same low-loss polymer used in Chapter 8, and finally the rod is removed. Fig. 9.1 shows the final structure after the rod is removed: the nanowire is shown in blue, the analyte channel (in the space previously belonging to the support rod) in brown and Teflon in light green. It is a compact and robust device with an intrinsic fluidic channel to deliver samples to the sensor, unlike most ring or microsphere resonators which require an additional channel. The embedded nanowire has a considerable fraction of its mode propagating in the fluidic channel, thus any change in the analyte properties is reflected in a change of the mode properties at the CMCRS output. Since the CMCRS is fabricated from a single tapered optical fibre, light can be coupled into the sensor with essentially no insertion loss: a huge advantage over other types of resonator sensors.

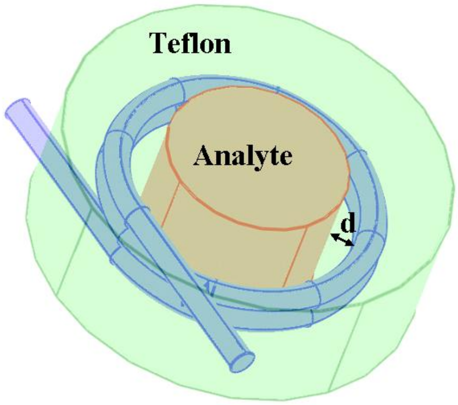

Fig. 9.1: Schematic of the CMCRS.

9.1.2 Theory of the CMCRS

Assuming continuous-wave (CW) input, a change of the analyte refractive index will lead to a change of the effective index n_{eff} of the propagating mode, thereby shifting the mode relative to the resonance and thus modifying the transmission coefficient *T*. Here, only the simplest case of a two-turn resonator is investigated, although it can be easily extended to the case of multi-turn resonators. A two-turn CMCRS can be easily evaluated using coupled mode equations as discussed in Section 7.2.1; if β is the real propagation constant, α the loss coefficient, and $K = \kappa L$ the coupling parameter for coupling coefficient κ and nanowire length *L* of a single turn, then *T* can be obtained from Eq. (7.2.16):

$$T = \frac{\exp(i\beta L - \alpha L) - i \sin K}{\exp(-i\beta L + \alpha L) + i \sin K} \qquad (9.1.1)$$

Resonances ($|T|$ is the minimum) occur if K and β are near to the values

$$K_m = \arcsin\gamma + 2m\pi, \qquad (9.1.2)$$

$$\beta_n = 2\pi n_{eff}/\lambda_{0n} = (2n+1)\pi/(2L) \qquad (9.1.3)$$

respectively. λ_{0n} is the resonant wavelength, and

$$\gamma = \exp(-\alpha L) \qquad (9.1.4)$$

(m and n are integers).

The mode properties are particularly affected by two important parameters: the nanowire radius r and the coating thickness d between the nanowire and the fluidic channel. n_{eff} is a function of r and d hence the resonance wavelength varies with r and d according to Eq. (9.1.3) Fig. 9.2 shows the cross-section of the coated nanowire. The effective index has been evaluated by a finite element method with the commercial software COMSOL3.3; only the fundamental mode was considered. The fundamental mode which has the largest propagation constant is the only mode that is well-bounded in the vicinity of the fibre core [13, 14].

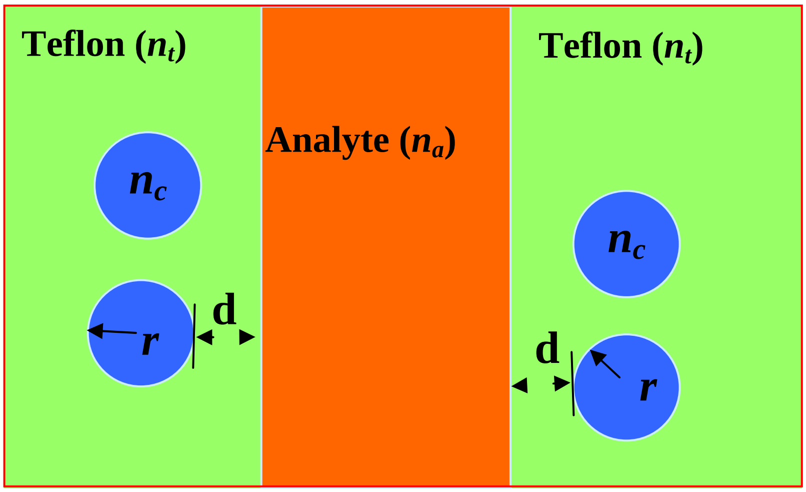

Fig. 9.2: The cross section of CMCRS.

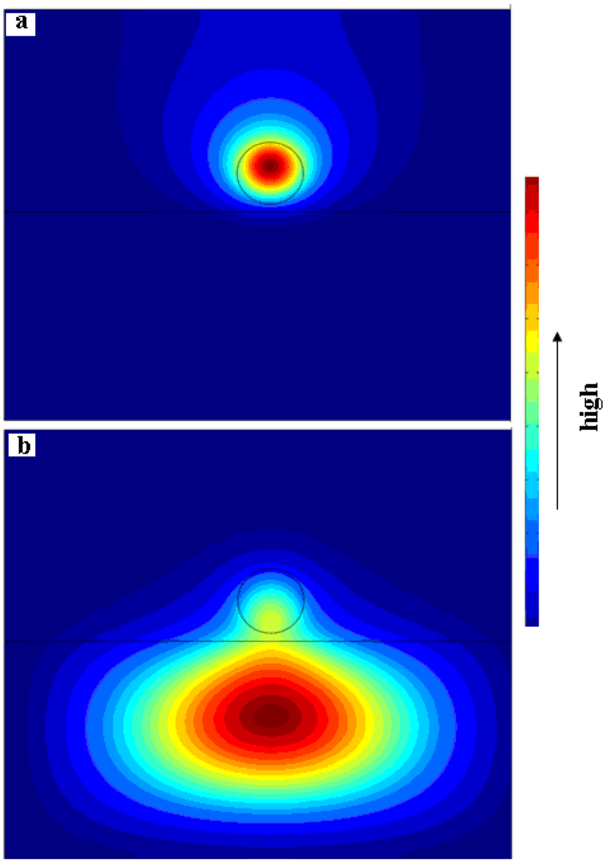

Fig. 9.3: Intensity distribution of rigid mode at two examples (a) n_a=1 and (b) n_a=1.37 when n_c=1.451, n_t=1.311, d=100 nm, r=500 nm.

Fig. 9.3 shows the intensity distribution of the fundamental mode at two examples (a) n_a=1 and (b) n_a=1.37 when n_c=1.451, n_t=1.311, d=100 nm, r=500 nm, λ=1550nm. When n_a is small (Fig. 9.3a) the field is still bound within the microfibre physical boundary, while it shifts into the coating and leaks into the analyte area, when n_a is large (Fig. 9.3b).

Fig. 9.4 shows the dependence of n_{eff} on the analyte refractive index n_a assuming the refractive index of the nanowire and of Teflon to be n_c=1.451 and n_t=1.311, respectively. Here we use the parameters r=500 nm and the three values 10 nm, 100 nm, and 500 nm for d.

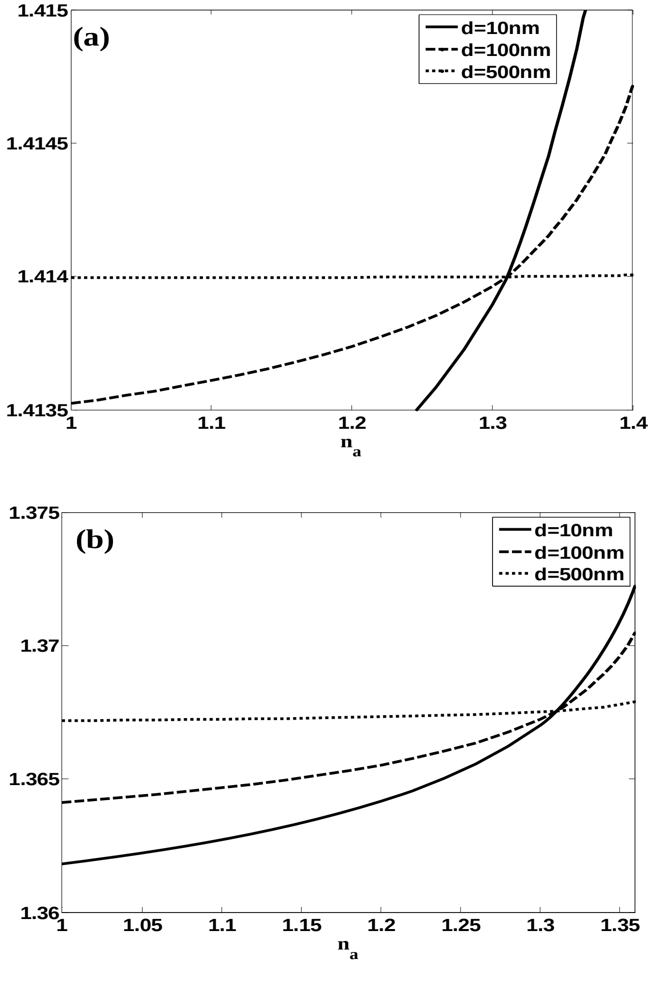

Fig. 9.4: Dependence of the effective index of a coated nanowire n_{eff} on the index of the analyte n_a for n_t=1.311, n_c=1.451, r=500 nm, d=10 nm (solid line), 100 nm (dashed), and 500 nm (dotted). The wavelength of the propagating mode is (a) λ=600 nm, (b) λ=970 nm.

Generally, n_{eff} increases with n_a, and increases more quickly with smaller d since in this case a larger fraction of the mode is propagating in the analyte, as shown in Fig. 9.3. If $n_a=n_t$, light cannot see the boundary between Teflon and the analyte solution, and therefore n_{eff} is the same at different Teflon thickness d. As seen in Fig. 9.4a or 9.4b, this value of n_a is a cross-point for different d.

9.1.3 Sensitivity

The homogeneous sensitivity S is obtained by monitoring the shift of the resonant wavelength λ_0 (corresponding to one of the propagation constants β_n in Eq.(9.1.3)) and can be defined as [6]

$$S=\frac{\partial\lambda_0}{\partial n_a}=\frac{\partial\lambda_0}{\partial n_{eff}}\frac{\partial n_{eff}}{\partial n_a}=\frac{2\pi}{\beta_n}\frac{\partial n_{eff}}{\partial n_a}=\frac{\lambda_0}{n_{eff}}\frac{\partial n_{eff}}{\partial n_a} \tag{9.1.5}$$

Since water is the solvent for most analytes and the device performances are affected by high losses (Eqs. (9.1.1)-(9.1.5)), it is useful to work in a spectral region of low water absorption. Fig. 9.5 shows the absorption index H of water for the 200-1000 nm spectral region, where H is defined as the ratio of the imaginary part and real part of the complex refractive index:

$$H=\frac{imag(n)}{real(n)} \tag{9.1.6}$$

The smooth solid-line curve is based mostly on data of Clarke and James (CJ)[15], Lenoble and Saint-Guilly (LSG)[16], Tyler (TSW)[17]. As shown in Fig.9.5, the absorption of water increases at long wavelengths [18]. In Fig. 9.5, the lines are discontinued because they have different multiplying coefficient. In this thesis, only two short wavelengths 600nm and 970nm are considered.

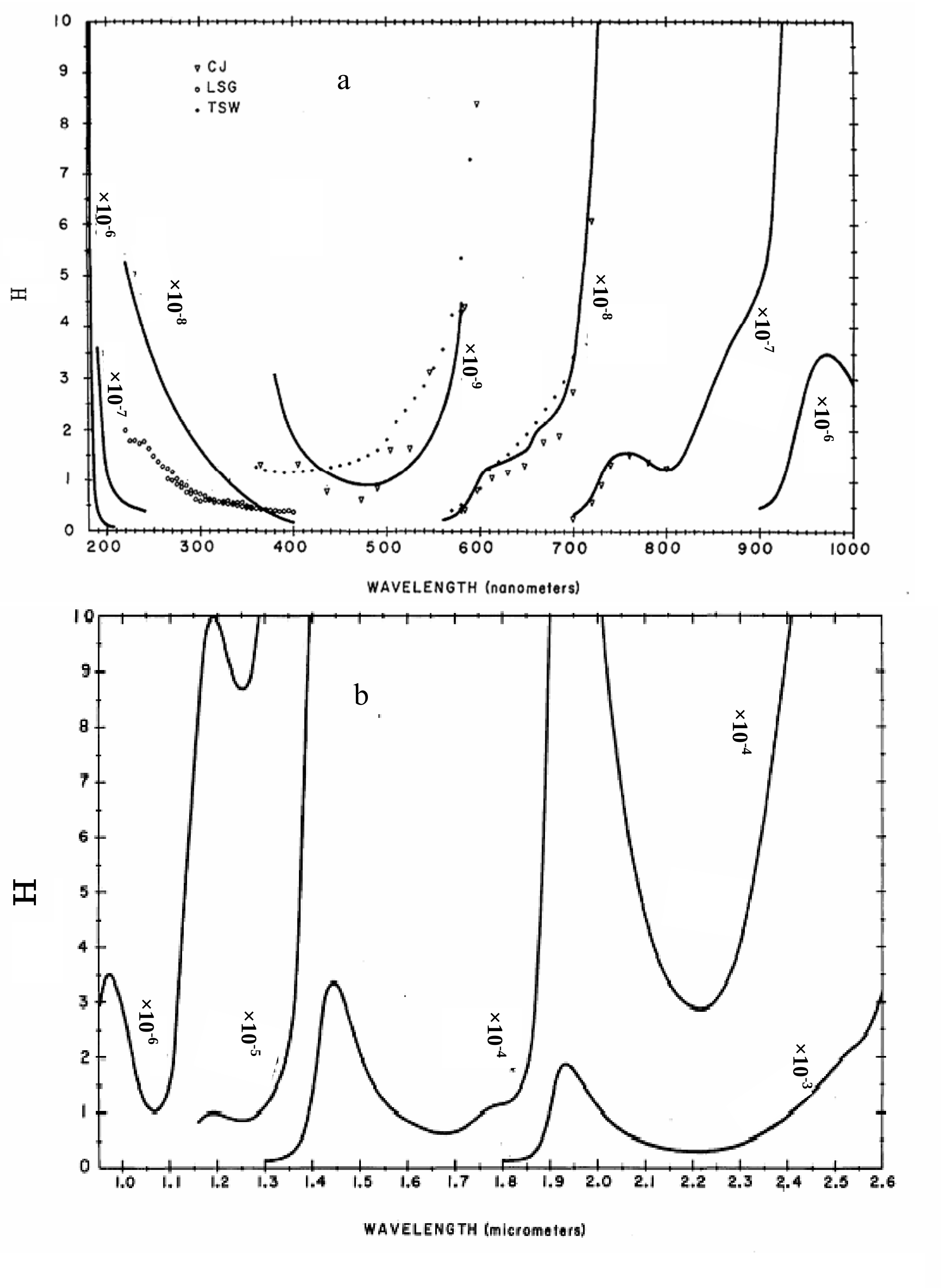

Fig. 9.5: Absorption index of water (a) for the 200-1000 nm spectral region [18]. (b) for the 950-2600 nm spectral region [18]. Here the lines are discontinuous because they have different multiplying coefficients.

S was calculated near n_a=1.332 at 600 nm and 970 nm. Fig. 9.6 shows the dependence of *S* on the nanowire radius *r* for different *d*. *S* increases when *d* decreases or λ increases because of the increasing fraction of power in the evanescence field.

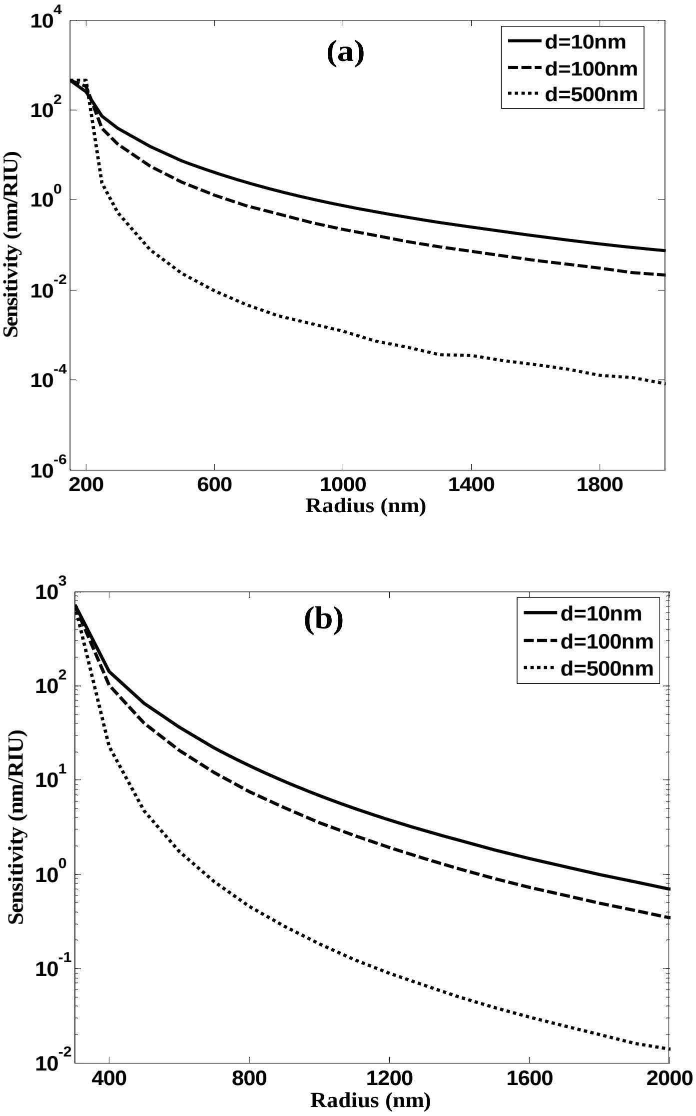

Fig. 9.6: Sensitivity of the CMCRS versus nanowire radius for (a) λ=600 nm and (b) λ=970 nm and for different values of *d*. Here, n_a=1.332, n_t= 1.311, and n_c=1.451.

Decreasing the nanowire radius *r* also increases the sensitivity *S* because this increases the fraction of the mode field inside the fluidic channel. *S* reaches 500 nm/RIU (where RIU stand for refractive index unit) at $r \approx 200$ nm for λ=600 nm and 700 nm/RIU at $r \approx 300$ nm for λ=970 nm. For even smaller values of *r*, the fundamental mode is no longer well confined and most of the evanescent field is in the analyte. The change of n_{eff} becomes linearly dependent on n_a, the derivative in the last term of Eq. (9.1.5) reaches a uniform value and the sensitivity reaches a plateau.

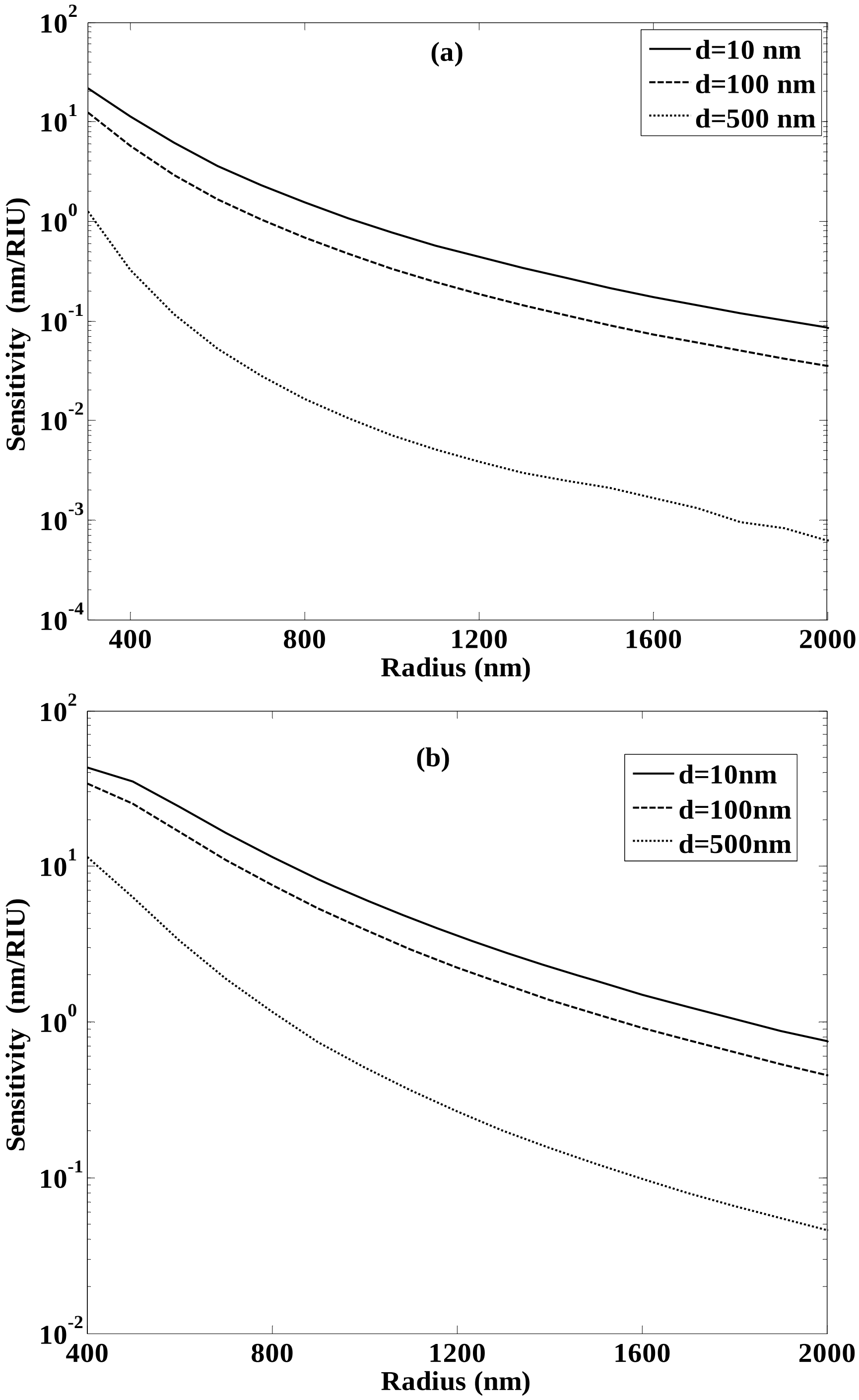

Fig. 9.7: Sensitivity of the CMCRS versus nanowire radius with UV375-coating for (a) λ=600 nm and (b) λ=970 nm and for different values of *d*. Here, n_a=1.332, n_t= 1.375, and n_c=1.451.

The sensitivity was also calculated when the coating material is UV375 (index~1.375) at wavelength λ=600 and λ=970. Fig 9.7 shows the sensitivity of the UV375 coated CMCRS versus nanowire radius for (a) λ=600 nm and (b) λ=970 nm and for different values of d. Here, n_a=1.332, n_t= 1.311, and n_c=1.451. The sensitivity is smaller than the Teflon coated CMCRS. It is only 50 nm/RIU for r=400 nm, d=10 nm and λ=970 nm. Since the refractive index of UV375 is higher than Teflon, a smaller fraction of the evanescent field is in the channel and the last element of Eq. (9.1.5) is smaller than in the case of Teflon coated CMCRS.

9.2 Sensor Based on a Microfiber Loop Resonator

9.2.1 Schematic and Manufacture

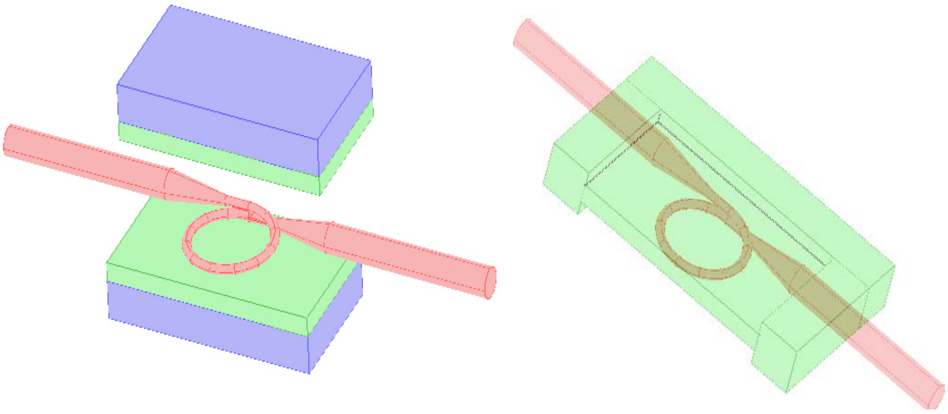
(a) (b)

Fig. 9.8: (a) Schematic of the manufacturing process of an ENLR. (b) The final structure of the ENLR.

An embedded nanowire loop resonator (ENLR) can be fabricated as shown in Fig. 9.8(a): two substrates are fabricated with disposable materials (blue) such as PMMA and coated with a thin layer of a low-loss low-refractive-index polymer such as Teflon (green); next, the self-coupling nanowire loop resonator (red) with a 1 mm diameter is manufactured on one of the substrates; then the other substrate is placed on top of the nanowire resonator. The use of a thick substrate allows to easily handling thin coating layers. The whole system is subsequently coated by a thick polymer layer and at last the expendable materials are removed, leaving a thin layer of low refractive index material on the nanowire.

The final device is shown in Fig. 9.8(b): a very thin polymer layer covers the loop of the ENLR while a thick coating deposit is used to fix the two fibre pigtails. The ENLR is a compact device with two sides exposed to the liquid to sense. The embedded nanowire has a considerable fraction of its mode propagating outside the embedding medium both in the in the upper and lower areas, thus any change in the analyte properties reflects in a change of the mode properties at the ENLR output.

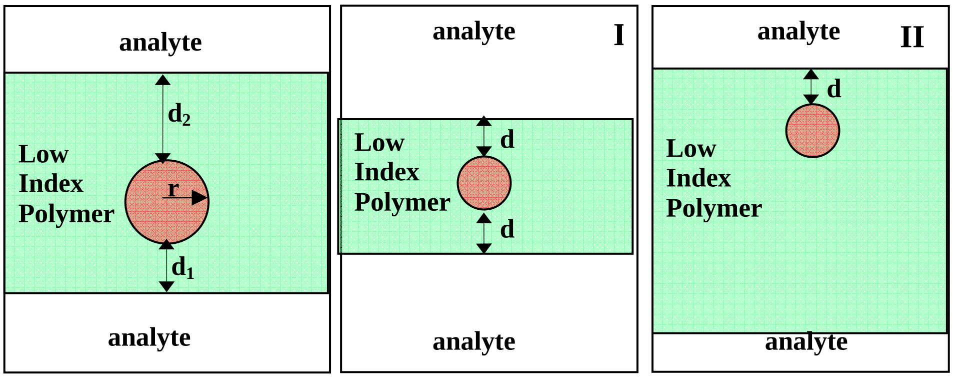

Fig. 9.9: Cross-section of the ENLR, (I) $d_1=d_2=d<1\,\mu\text{m}$, (II) $d_1\rightarrow\infty$ and $d_2=d<1\,\mu\text{m}$.

9.2.2 Theory of ENLR

As for the CMCRS, a change of the analyte refractive index will lead to a change of the effective index n_{eff} of the propagating mode, thereby shifting the mode relative to the resonance and thus modifying the transmission spectrum. The transmission coefficient T can be easily evaluated using Eq. (6.5.2); if $\beta = 2\pi n_{eff}/\lambda$ is the propagation constant, α the loss coefficient, and $K = \kappa L$ the coupling parameter for coupling coefficient κ and nanowire loop length L, the resonance condition is Eq. (6.5.2):

$$\beta_n=(2n+1)\pi/(2L), \tag{9.2.1}$$

where n are integers.

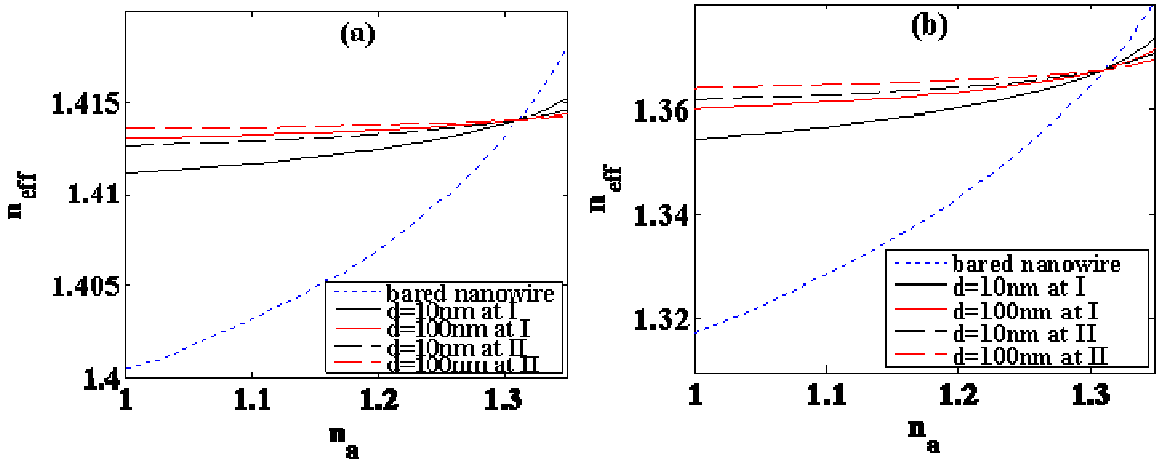

Fig. 9.10: Dependence of the effective index of a coated nanowire n_{eff} on the index of the analyte n_a for n_t=1.311, n_c=1.451, r=500 nm d=10 nm (black line) and 100 nm (red) for small coating thicknesses (case I: solid line) and infinitely thick layer on one side (case II: dashed). The blue dotted line represents a bare nanowire. The wavelength of the propagating mode is (a) λ=600 nm, (b) λ=970 nm.

Because of the interface with the analyte, the mode propagating in the coated fibre nanowire experiences a refractive index surrounding which is strongly affected by the analyte. The ENLR cross-section is shown in Fig. 9.9; the mode properties are particularly affected by three parameters: the nanowire radius r and the coating thicknesses d_1 and d_2 in the upper and lower layers. When one of the distances d_1 and d_2 is very large, the device resembles the case of a conventional D-shaped fibre [13, 14]. Two typical cases are investigated, (I) $d_1=d_2=d<1\mu$m and (II) $d_1\rightarrow\infty$ and $d_2=d<1\mu$m. Fig. 9.10 shows the dependence of n_{eff} on the analyte refractive index n_a assuming the refractive index of the nanowire and of the embedding low refractive index polymer (Teflon) to be n_c=1.451 and n_t=1.311, respectively. While *r* is assumed to be 500 nm, two values for *d* are considered: 10 nm and 100 nm. Generally, n_{eff} increases with n_a, and increases more quickly with smaller *d* in I and II since in this case a larger fraction of the mode is propagating in the analyte. n_{eff} in I is larger than in II when $n_a<n_t$, and n_{eff} in I is smaller than in II when $n_a>n_t$. If $n_a=n_t$, the propagating light does not see the boundary between Teflon and the analyte solution, and therefore n_{eff} is independent of the Teflon thickness *d*, as seen in Fig. 9.10. The dependence for the bare nanowire is presented for comparison. Compared with ENLRs which have only one side or two sides for sensing, the bare nanowire has a largest fraction of the mode is propagating in the analyte, hence, n_{eff} is larger than in ENLRs when $n_a<n_t$, and n_{eff} is smaller than in ENLRs when $n_a>n_t$.

9.2.3 Sensitivity

The sensitivity near n_a=1.332 at short wavelengths (600 nm and 970 nm) was calculated using Eq.(9.1.5). Fig. 9.11 shows the dependence of *S* on the nanowire radius *r* for different *d* at I and II. *S* increases when *d* decreases or λ increases in accordance with the results of Fig. 9.11. Decreasing the nanowire radius *r* also increases *S* because this increases the fraction of the mode field inside the fluidic channel. *S* reaches 500 nm/RIU (where RIU is refractive index unit) at $r\approx200$ nm for λ=600 nm and 700 nm/RIU at $r\approx300$ nm for λ=970 nm. This is higher than in most microresonator sensors.

At the same wavelength and diameter of microfibre, the sensitivity in case I (two sensing surfaces) is larger than in case II (one sensing surface), because of the larger overlap between the evanescent field propagating in the microfiber and the analyte. For even smaller values of *r*, the sensitivity reaches a plateau because the fundamental mode is no longer well confined and most of the evanescent field is in the analyte. In this case n_{eff} becomes linearly dependent on n_a, and the derivative in the last term of Eq. (9.1.5) reaches a uniform value and so the sensitivity reaches a plateau.

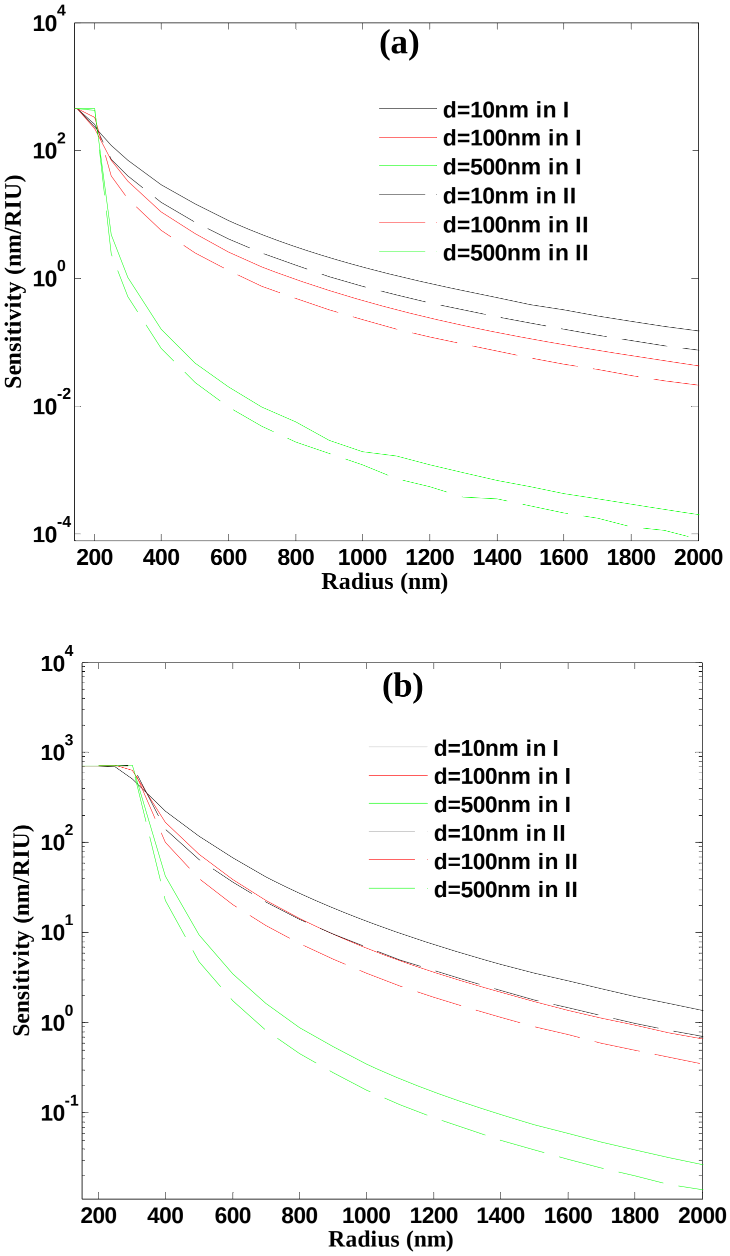

Fig. 9.11: Sensitivity of the ENLR versus nanowire radius for (a) λ=600 nm and (b) λ=970 nm and for different values of *d* in I (solid line) and II (dashed). Here, n_a=1.332, n_t= 1.311, and n_c=1.451.

In these simulations, β and the loss are assumed uniform, which in practice it is difficult to realize. For example, where the nanowire loop closes, the ENLR height doubles, the overlay thickness can change, the two device/analyte interfaces are not parallel, and therefore *d* and *β* are not uniform. Additionally, when d is as small as 10 nm, the refractive index is close to the value of the surface refractive index, rather than to the bulk refractive index. For theoretical estimation, *d, β* and *n* can be assumed to represent the averaged values over the nanowire loop and it is still possible to assume that they are uniform along the device length.

The sensitivity predicted for the ENLR sensors is the same as the sensor based on a 3D resonator CMCRS (Section 9.1), because the mode propagating in the microfiber experiences the same effective refractive index changes. Still, the manufacture of the embedded sensor is not easier than that of the nanowire without support, but the protected device is clearly advantageous.

9.3 Detection Limit

For a resonating wavelength-shift sensor, the detection limit is another critical parameter to evaluate the sensing capability of a device. The detection limit can be defined as $\delta\lambda_0/S$ [6], where $\delta\lambda_0$ is the smallest measurable wavelength shift. Theoretically, $\delta\lambda_0$ is determined merely by the instrument resolution, and independent of the resonance shape or the resonant bandwidth. However, it is difficult for a broad resonator shape to achieve the accurate detection because it is easy to be perturbed by noise and other reasons [6]. To enhance the accuracy in detecting the wavelength shift, a narrower resonance is required. Experimentally, $\delta\lambda_0$ can be taken as a fraction of FWHM of the monitored resonance [3] (in literature the fraction has been consistently assumed to be 1/20). The sharper the resonance, the smaller $\delta\lambda_0$ can be achieved. Generally, the sensor performance is mainly limited by its own properties, but the instrument resolution is also important especially when the Q-factor of the sensor is very large. Additionally, there are other limitations for the sensor, for example temperature, vibrations….. Table 9.1 summarizes the features of some common evanescent field index sensors based on resonators as reported in the literature. The analyte index is close to 1.3.

For the CMCRS and ENLR, FWHMs and Q-factors depend on the resonator coupling and loss. In traditional microresonators light is coupled into the resonator using prism coupling, anti-resonator reflecting waveguide coupling, or fibre taper coupling [1-5]. With probably the only exception of the fibre taper coupling, which has been proved to be reasonably efficient [19], coupling to microresonator has been considerably complicate in terms of device design and/or of increase of the overall loss. The CMCRS and ENLR, on the other hand, have low insertion loss. Resonant coupling and therefore high Q-factors can also be achieved by optimized designs [20, 21]. Losses in the CMCRS and ENLR arise from surface scattering, material (analyte, coating, and fibre) absorption, and bending losses. The smallest reported loss of an optical nanowire is about α=0.001 dB/mm with radii in the range of hundreds of nanometers [22, 23]. The water absorption can be reduced to levels well below 0.0001 dB/mm by operating at short wavelengths as shown in Fig. 9.5. Cladding materials (such as Teflon or UV375) can be used for low coating loss. For example, for water-core Teflon waveguides losses of 1 dB/m have been reported [24, 25]. The estimated bend loss for a 200-nm-radius nanowire and a 500-μm-diameter coil at a wavelength of 600 nm is 10^{-4} dB/mm (from Eq. (3.2.1)), which quickly decreases further for increasing coil diameters. Therefore, if the propagation loss is assumed to be α=0.01 dB/mm, the other losses can be neglected. From Eq. (6.5.2) for a CMCRS or ENLR with r=200 nm at λ=600 nm, the FWHM is $4\cdot10^{-4}$ nm and the detection limit is 10^{-6}-10^{-7} RIU. In Table 9.1 microspheres and microcapillaries have extremely high Q-factors, which upon optimization could lead to sensitivities comparable to the one predicted here for the CMCRS. However, the ease of mode size control via the nanowire diameter and the lossless input and output coupling via the fibre pigtails are unique features of the CMCRS. Additionally, planar ring resonators are expected to have similar sensitivities when similar design parameters are used. Yet, from the experimental point of view it is challenging to achieve losses comparable to the loss achieved in microfibres.

Table 9.1: Summary of surface sensitivity and FWHM for evanescent field refractometric resonating sensors.

Type of sensor	S (nm/RIU)	Wavelength (nm)	FWHM (nm)	FWHM/ δλ/δn (RIU)	Ref.
Microsphere	30	980	$2 \cdot 10^{-4}$	$6 \cdot 10^{-6}$	[3]
Photonic crystal microresonator	228	1500	~1	$3 \cdot 10^{-3}$	[1]
Microcapillary	45	980	$1.55 \cdot 10^{-4}$	$3 \cdot 10^{-6}$	[5]
Hollow-core ARROW*	555	700	>1	$2 \cdot 10^{-3}$	[9]
Slot Waveguide	212	1300	0.722	$3 \cdot 10^{-3}$	[26]
Ring resonator by capillary fibre	~30	1545	>0.5		[27]
CMCRS or ENLR	700	970	$4 \cdot 10^{-4}$	10^{-7}	This thesis

9.4 Manufacture of CMCRS

In this section, we experimentally demonstrate for the first time a CMCRS based on a Teflon-coated 3D microfibre coil resonator.

The CMCRS was fabricated as follows: first, a microfibre was fabricated. The length and diameter of the uniform waist region of the fabricated microfibre were 50 mm and ~2.5 μm respectively. The microfibre was then wrapped on a 1mm-diameter PMMA rod. The whole structure was repeatedly coated by the Teflon solution 601S1-100-6, as shown in Section 8.3. The dried embedded microcoil resonator was then left into Acetone to dissolve the support rod. The whole PMMA rod was completely dissolved in 1-2 days at room temperature. At last the OMCRS sensor with a ~1mm-diameter microchannel and two input/output pigtails was obtained. The picture of the sensor is shown in Fig. 9.12. The sensor consists of a microfibre resonator with five turns and a microfluidic channel inside. The adjacent microfibres are very close and the major coupling area is in the middle. Although some bubbles are left inside the CMCRS during the drying process, these seem to be far from the microfibre and do not affect the overall sensor operation.

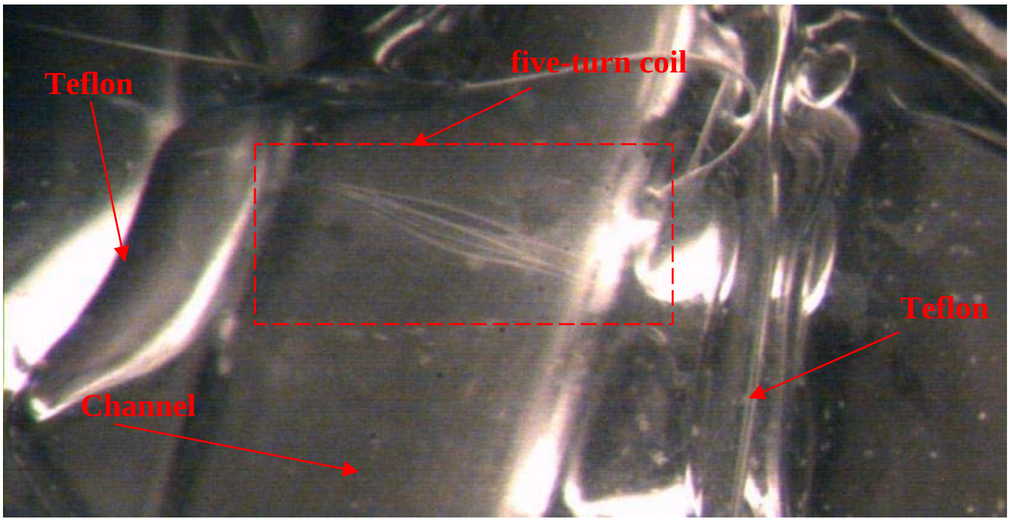

Fig. 9.12: Picture of CMCRS.

9.5 Sensitivity

The sensitivity was measured inserting the sensor in a beaker containing mixtures of Isopropyl and Methanol, where the Isopropyl had the following ratios: ①60%, ②61.5%, ③63%, ④64.3%, ⑤65.5%, ⑥66.7%, ⑦67.7%. The ratio was increased by adding small calibrated Isopropyl quantities to the solution in a position far from the sensor. The refractive indexes of Isopropyl and Methanol at 1.5 μm are 1.364 and 1.317 respectively [28]. The sensor was connected to an Erbium-doped fiber amplifier and an optical spectrum analyzer and then immersed into the mixtures. Fig. 9.13 shows the spectra recorded at 1530 nm. The resonator peak shifts towards longer wavelengths for increasing Isopropyl concentration as expected. The extinction ratio increases from ①, achieves maximum at ④ and then decreases and this can be explained by the change of coupling coefficient with the refractive index.

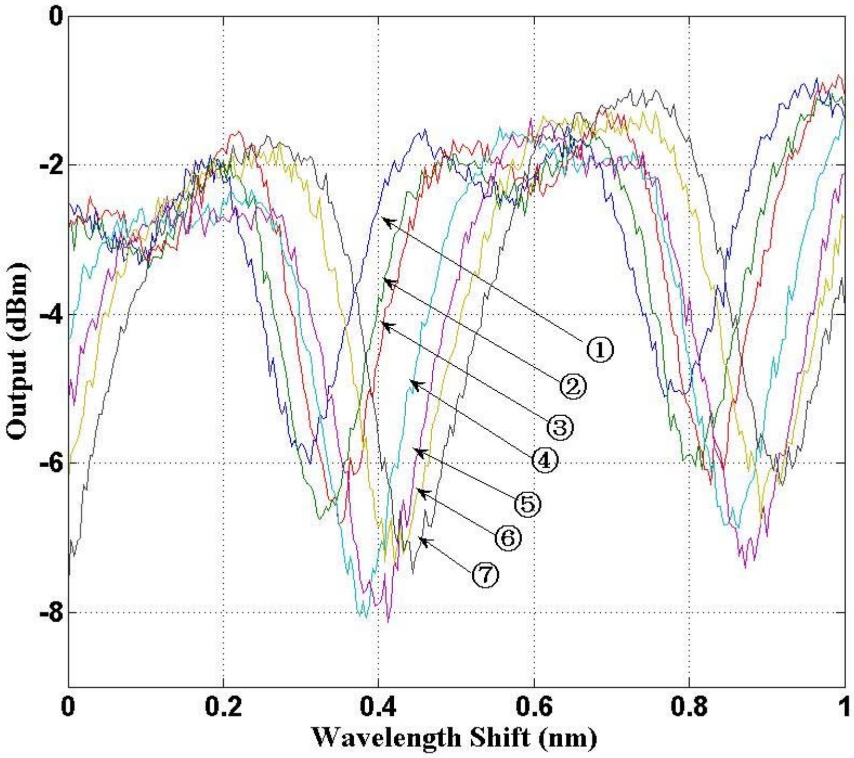

Fig 9.13: Output spectrum of the OMCRS in seven different mixtures of Isopropyl and Methanol; the Isopropyl fraction is ①60%, ②61.5%, ③63%, ④64.3%, ⑤65.5%, ⑥66.7%, and ⑦67.7% respectively.

Even though the transmission properties of a multi-turn microfibre coil resonator can be simulated by solving multiple coupled wave equations, its spectrum is very complicated. In most cases, there is only one dominating resonance, which can be easily evaluated using the coupled mode equations with results analogous to those of a single-loop resonator. From Eqs. (9.1.1)-(9.1.3), it is clear that the wavelength at resonance changes with n_{eff}. The effective index n_{eff} of the fundamental mode propagating in the optical microfibre was evaluated for different d. Fig. 9.14 shows the measured wavelength shift (dashed lines) and calculated (solid lines) for r=1250 nm and different polymer thicknesses d. The error bars originate from two sources: the index error arises from the estimation of the liquid volume in the mixture; the wavelength error comes from the estimated difference between the real and the measured resonance centres in the spectrum.

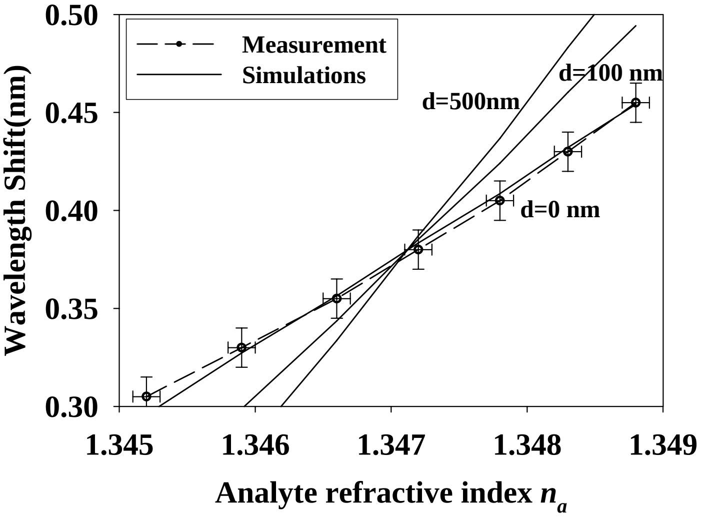

Fig. 9.14: Dependence of the measured and calculated wavelength shifts on the liquid mixture refractive index. The dashed line represents the measured results while the solid lines are the calculated results for *r*=1250 nm and different polymer thicknesses *d*.

The simulation shows that the slope increases when the thickness *d* decreases because of the larger evanescent field. The best fit occurs for *d*~0 suggesting that the Teflon layer is very thin. This is consistent with the experimental results: since the microfiber has been wrapped tightly onto the support rod, Teflon can only penetrate the small gaps provided by the support rod roughness, which is in average considerably smaller than 100nm. The small difference observed in Fig. 9.14 has been attributed to the uneven profile of the microfibre diameter, to the imprecise winding of the microcoil resonator, to the roughness of the channel inner surface and to the uneven distance of the microfibre from the microfluidic channel. The sensitivity, defined as the slope of these lines [29], was evaluated to be about 40 nm/RIU from the data of Fig. 9.14. This value is comparable with those reported previously for microsphere and microring resonators [1, 3, 4], but smaller than recently reported values for a slot waveguide (212.13 nm/RIU) [26]. The relatively low value for the sensitivity can be attributed to the small overlap between the mode propagating in the microfibre resonator and the analyte. Another factor which has probably affected the sensor sensitivity is the lack of smoothness of the device surface in contact with the analyte; this is possibly caused by PMMA residues on the surface of the channel or it may originate from the original roughness of the PMMA support rod. This roughness produced the moderately low Q-factor observed in the resonator ($Q \sim 10^4$), which limited the interaction length between the mode and the analyte. It is believed that the overall sensitivity can be considerably improved to $\sim 10^4$ by using thinner microfibres and by fabricating microcoil resonators with higher Q-factors. The minimum detectable refractive index change (Δn_{min}=FWHM/ $\delta\lambda/\delta n$, column 5 in table 9.1) for this sensor is limited by the accuracy in the measurement of the peak wavelength (15pm). Assuming S=40nm/RIU, the minimum detectable refractive index change results to be $\Delta n_{min} \sim 0.015/40 \sim 4 \cdot 10^{-4}$. This value can be decreased with the use of better detection systems and more stable sources.

9.6 Summary

New refractometric sensors based on microfibre coil resonator and loop resonators were theoretically discussed and experimentally demonstrated. A microfibre coil resonating sensor was manufactured and a sensitivity of ~40 nm/RIU was recorded.

9.7 References

1. M. Adams, G. A. DeRose, M. Loncar, and A. Scherer, "Lithographically fabricated optical cavities for refractive index sensing," Journal of Vacuum Science & Technology B **23**, 3168-3173 (2005).

2. C. Y. Chao, W. Fung, and L. J. Guo, "Polymer microring resonators for biochemical sensing applications," IEEE Journal of Selected Topics in Quantum Electronics **12**, 134-142 (2006).

3. N. M. Hanumegowda, C. J. Stica, B. C. Patel, I. White, and X. D. Fan, "Refractometric sensors based on microsphere resonators," Applied Physics Letters **87**, 201107 (2005).

4. I. M. White, H. Oveys, X. Fan, T. L. Smith, and J. Y. Zhang, "Integrated multiplexed biosensors based on liquid core optical ring resonators and antiresonant reflecting optical waveguides," Applied Physics Letters **89**, 191106 (2006).

5. I. M. White, H. Y. Zhu, J. D. Suter, N. M. Hanumegowda, H. Oveys, M. Zourob, and X. D. Fan, "Refractometric sensors for lab-on-a-chip based on optical. ring resonators," IEEE Sensors Journal **7**, 28-35 (2007).

6. C. Y. Chao, and L. J. Guo, "Design and optimization of microring resonators in biochemical sensing applications," Journal of Lightwave Technology **24**, 1395-1402 (2006).

7. A. N. Chryssis, S. M. Lee, S. B. Lee, S. S. Saini, and M. Dagenais, "High sensitivity evanescent field fiber Bragg grating sensor," IEEE Photonics Technology Letters **17**, 1253-1255 (2005).

8. O. Esteban, N. Diaz-Herrera, M. C. Navarrete, and A. Gonzalez-Cano, "Surface plasmon resonance sensors based on uniform-waist tapered fibers in a reflective configuration," Applied Optics **45**, 7294-7298 (2006).

9. S. Campopiano, R. Bernini, L. Zeni, and P. M. Sarro, "Microfluidic sensor based on integrated optical hollow waveguides," Optics Letters **29**, 1894-1896 (2004).

10. F. Prieto, B. Sepulveda, A. Calle, A. Llobera, C. Dominguez, and L. M. Lechuga, "Integrated Mach-Zehnder interferometer based on ARROW structures for biosensor applications," Sensors and Actuators B-Chemical **92**, 151-158 (2003).

11. F. Prieto, B. Sepulveda, A. Calle, A. Llobera, C. Dominguez, A. Abad, A. Montoya, and L. M. Lechuga, "An integrated optical interferometric nanodevice based on silicon technology for biosensor applications," Nanotechnology **14**, 907-912 (2003).

12. P. Debackere, S. Scheerlinck, P. Bienstman, and R. Baets, "Surface plasmon interferometer in silicon-on-insulator: novel concept for an integrated biosensor," Optics Express **14**, 7063-7072 (2006).

13. D. Marcuse, F. Ladouceur, and J. D. Love, "Vector Modes of D-Shaped Fibers," IEE Proceedings-J Optoelectronics **139**, 117-126 (1992).

14. M. S. Dinleyici, and D. B. Patterson, "Vector modal solution of evanescent coupler," Journal of Lightwave Technology **15**, 2316-2324 (1997).

15. G. L. Clarke, and H. R. James, "Laboratory analysis of the selective absorption of light by sea water," J. Opt. Soc. Am. **29**, 43-55 (1939).

16. J. Lenoble, and B. Saint-Guily, "The absorption of ultraviolet. light by distilled water," Compt. Rend. **240**, 954-955 (1955).

17. J. E. Tyler, R. C. Smith, and J. W. H. Wilson, "Predicted Optical Properties for Clear Natural Water," Journal of the Optical Society of America **62**, 83 (1972).

18. G. M. Hale, and M. R. Querry, "Optical-Constants of Water in 200-Nm to 200-Mum Wavelength Region," Applied Optics **12**, 555-563 (1973).

19. M. Cai, O. Painter, and K. J. Vahala, "Observation of critical coupling in a fiber taper to a silica-microsphere whispering-gallery mode system," Physical Review Letters **85**, 74-77 (2000).

20. F. Xu, P. Horak, and G. Brambilla, "Optimized Design of Microcoil Resonators," Journal of Lightwave Technology **25**, 1561-1567 (2007).

21. F. Xu, P. Horak, and G. Brambilla, "Conical and biconical ultra-high-Q optical-fiber nanowire microcoil resonator," Applied Optics **46**, 570-573 (2007).

22. G. Brambilla, F. Xu, and X. Feng, "Fabrication of optical fibre nanowires and their optical and mechanical characterisation," Electronics Letters **42**, 517-519 (2006).

23. S. G. Leon-Saval, T. A. Birks, W. J. Wadsworth, P. S. J. Russell, and M. W. Mason, "Supercontinuum generation in submicron fibre waveguides," Optics Express **12**, 2864-2869 (2004).

24. R. Altkorn, I. Koev, R. P. VanDuyne, and M. Litorja, "Low-loss liquid-core optical fiber for low-refractive-index liquids: fabrication, characterization, and application in Raman spectroscopy," Applied Optics **36**, 8992-8998 (1997).

25. P. Dress, M. Belz, K. F. Klein, K. T. V. Grattan, and H. Franke, "Physical analysis of teflon coated capillary waveguides," Sensors and Actuators B-Chemical **51**, 278-284 (1998).

26. C. A. Barrios, K. B. Gylfason, B. Sánchez, A. Griol, H. Sohlström, M. Holgado, and R. Casquel, "Slot-waveguide biochemical sensor," Optics Letters **32**, 3080-3082 (2007).

27. M. Sumetsky, R. S. Windeler, Y. Dulashko, and X. Fan, "Optical liquid ring resonator sensor," Optics Express **15**, 14376-14381 (2007).

28. C. B. Kim, and C. B. Su, "Measurement of the refractive index of liquids at 1.3 and 1.5 micron using a fibre optic Fresnel ratio meter," Measurement Science & Technology **15**, 1683-1686 (2004).

29. I. M. White, and X. Fan, "On the performance quantification of resonant refractive index sensors," Optics Express **16**, 1020-1028 (2008).

Chapter 10

Summary and Future work

This chapter summarizes the work and results presented throughout this thesis on optical nanowire devices and presents possible future directions of research.

10.1 Summary and Conclusion

The Optical Fibre Nanowires (OFN) are versatile building blocks for the assembly of micro- and nano-photonic devices since they offer a number of unique optical and mechanical properties, including: large evanescent fields; high nonlinearity; extreme flexibility and configurability; low-loss interconnection to other fibres and fiberized components. Additionally, the OFN is fabricated by stretching optical fibres and thus preserves the original dimensions of the optical fibre at its input and output allowing ready splicing to standard fibres.

OFNs were manufactured with the so-called flame-brushing technique, their loss mechanisms were discussed and their loss measured on different diameters; The time-dependences of loss in bare OFN and OFN embedded in Teflon were measured and compared; a method to avoid unrecoverable induced loss by embedding OFN devices in Teflon was then presented, providing a practical solution to the manufacture of OFN resonators and sensors.

The first kind of device in this thesis was a short adiabatic taper tip, fabricated by P-2000, the profile of which was design using the theory previously developed by J.D. Love [1] and T.A. Birks [2]. Experimentally, the optical trapping of 1μm microspheres was demonstrated using this kind of taper tip at low powers (10 mW).

Most applications based on OFN are based on resonators; the Optical Nanowire Loop Resonator (ONLR) is the simplest OFN resonator and was investigated in theory and experimentally. An ONLR with a Q-factor of 7800 was demonstrated. The ONLR is easy to manufacture and can be cascaded, but it is not stable in air. Aerogel has been used for packaging and stabilizing the ONLR, but it is still not strong enough to protect it. The Optical Nanowire Microcoil Resonator (ONMR) is a more complicated resonator but it has a stable geometry because it is wrapped on a rod; still, it is more difficult to manufacture. Theoretical simulations suggest that the Q-factor is very sensitive to the coupling between adjacent turns; it is possible to reduce this kind of sensitivity and make it easier to obtain high-Q-factors by optimizing the geometry of the profiles. In this thesis, three different methods were presented.

Two-, three-, and four-turn MCRs were demonstrated experimentally by wrapping a several-microns-diameter microfibre on a Teflon-coated rod. MCRs were also embedded in Teflon to stabilize the structure and prevent surface contamination /degradation which would increase the propagation loss with time. The embedded MCRs are stable, portable, robust, and represent the key element for practical applications. In these experiments, the embedded MCR had a Q-factor greater than 6000. Recently, a MCR was reported with a Q-factor of 61000 in low refractive index liquid [3]. The Q factor of the resonator presented in this paper is low because of the high microfibre loss (~0.6 dB/mm) induced by the wrapping process. By using precisely controllable rotation and translation stages, in a controlled environment, all-coupling resonators (where the coupling length coincides with the loop length) with ultrahigh-Q factors should become obtainable.

Finally, refractometric sensors based on microfibre coil resonators and loop resonators were theoretically discussed, the dependence of the effective index on the analyte and the radius was calculated, and the relation between the sensor sensitivity and the nanowire radius calculated. The highest possible sensitivity was estimated to be 700 nm/RIU for nanowires with 300nm radius at wavelength of 970 nm. The estimated detection limit for the sensors was 10^{-6}-10^{-7} RIU. The sensor based on the microfibre coil resonator was demonstrated experimentally and a sensitivity of ~40 nm/RIU measured.

In conclusion, I

1) studied the basic theoretical characteristics and loss characteristics on OFN;

2) designed and manufactured short adiabatic tapers for optical tweezers, succeeding in the experimental demonstration of the phenomenon;

3) completed a series of simulations on OFN resonators;

4) experimentally demonstrated loop resonators and 3D resonators;

5) presented the schemes on the applications of OFN resonator in sensing, and

6) demonstrated a sensor based on Teflon-coated multi-turn microfibre resonator with a sensitivity of 40 nm/RIU.

The main objectives of the project have been achieved.

10.2 Future work

Future work is to reduce the surface roughness by improving the manufacture techniques; manufacture higher-Q-factor MCRs, and higher sensitivity sensors based on microfibre coil and loop resonators. It is also interested to investigate the nonlinearity aspects of OFN: including nonlinear signal processing, Raman lasers and applications in low threshold and high-efficient micro lasers, and supercontinuum generations in OFNs from other kinds of materials. Of course, it is important to find more new applications on OFN devices.

10.3 References

1. J. D. Love, W. M. Henry, W. J. Stewart, R. J. Black, S. Lacroix, and F. Gonthier, "Tapered Single-Mode Fibers and Devices .1. Adiabaticity Criteria," IEE Proceedings-J Optoelectronics **138**, 343-354 (1991).

2. T. A. Birks, and Y. W. Li, "The Shape of Fiber Tapers," Journal of Lightwave Technology **10**, 432-438 (1992).

3. M. Sumetsky, "Demonstration of a multi-turn microfiber coil resonator," in *Optical Fiber Communication Conference*(San Diego, USA, 2007). Paper PDP46.

List of Publications

BOOK CHAPTER:

- G. Brambilla, **F. Xu**, P. Horak and D. J. Richardson, ‘Optical Fiber Nanowires, Sub-wavelength Wires and Related Devices’, Chapter 5, ‘Progress in Optical Fibers Research’, ISBN 978-1-60021-868-2, © 2007 Nova, Science Publishers, Inc.

JOURNALS:

- **F. Xu**, and G. Brambilla, “Preservation of Micro-Optical Fibres by Embedding,” *Jpn. J. Appl. Phys.*, **47**, 8B (2008).
- **F. Xu**, and G. Brambilla, "Demonstration of optical microfiber coil resonator refractometric sensor," *Appl. Phys. Lett.*, **92**, 101126 (2008).
- **F. Xu**, V. Pruneri, V. Finazzi, and G. Brambilla, "An embedded optical nanowire loop resonator refractometric sensor," *Opt. Express* **16**, 1062-1067 (2008).
- **F. Xu,** and G. Brambilla， “Manufacture of 3D microfiber coil resonators,” IEEE *Photonics Technol. Lett.* **19**, 1481-1483 (2007).
- **F. Xu**, and G. Brambilla，“Embedding Optical Microfiber Coil Resonators in Teflon," *Opt. Lett.*, **32**, 2164-2166 (2007).
- **F. Xu**, P. Horak, and G. Brambilla, "Optical microfiber coil resonator refractometric sensor," *Opt. Express* **15**, 7888-7893 (2007).
- **F. Xu**, P. Horak, and G. Brambilla, "Optimized Design of Microcoil Resonators," *J. Lightwave Technol.* **25**, 1561-1567(2007).
- G. Brambilla, **F. Xu**, “Adiabatic submicrometric tapers for optical tweezers”, *Electronics Letters* .**43**, 204-206 (2007).
- **F. Xu**, P. Horak, and G. Brambilla, “Conical and biconical ultra-high-Q optical-fiber nanowire microcoil resonator,” ***Appl. Opt.***, **46**, 570-573 (2007).
- **F. Xu**, P. Horak, and G. Brambilla, “Conical and bi-conical high-Q optical nanofiber microcoil resonator”, ***Proc. of SPIE,*** 6351-101 (2006).
- G.. Brambilla, **F. Xu**, Feng. X, “Fabrication of optical fiber nanowires and their optical and mechanical characterization”, ***Electron. Lett.***, **42** ,517-519 (2006).

CONFERENCE PRESENTATIONS:

- **F. Xu**, and G. Brambilla, “Microfibre resonating optical sensors for microfluidics,” ***Photon*** Edinburgh 26-29 Aug 2008.
- **F. Xu**, and G. Brambilla, “High Sensitivity Refractometric Sensor Based on Embedded Optical Microfiber Loop Resonator,” ***CLEO/QELS*** San Jose USA 4-9 May 2008

- G. Brambilla and **F. Xu**, “Demonstration of a Refractometric Sensor Based on Optical Microfiber Coil Resonator,” ***CLEO/QELS*** San Jose USA 4-9 May 2008.
- G. Brambilla and **F. Xu**, “Micro-optical fibre sensor,” ***MOC '07*** Takamatsu Japan 28-31 Oct 2007.
- **F. Xu**, P. E. Horak, and G. Brambilla, “A simplified way to manufacture high-Q microfiber coil resonators by controlling the input/output coupling”, ***CLEO/Pacific Rim 2007*** Seoul Korea 26-31 Aug 2007.
- **F. Xu**, G. Brambilla, “Embedded optical microfiber coil resonator“, ***OECC/IOOC 2007*** Yokohama, Japan 9-13 Jul 2007.
- **F. Xu**, G. Brambilla, “Manufacture of 3D microfiber resonator “, post deadline paper, ***OECC/IOOC 2007*** Yokohama, Japan 9-13 Jul 2007.
- G. Brambilla, **F. Xu**, “Optical fibre nanowires and related structures“, ***ICTON 2007*** Rome, Italy 1-5 Jul 2007 (Invited).
- **F. Xu**, P. Horak, and G. Brambilla “Optical refractometric sensors based on embedded nanowire microcoil resonators“, ***OSA Topical Conference on Nanophotonics*** Hangzhou, China 18-21 Jun 2007.
- **F. Xu**, G. Brambilla, and D.J.Richardson, “Adiabatic SNOM tips for optical tweezers”***5th International Conference on Optics-Photonics Design & Fabrication (ODF '06)*** Nara, Japan 6-8 Dec 2006.
- Brambilla G., **F. Xu**, and D. J. Richardson, “SEM characterization of mm-long nanowires”, ***Nano-molecular Analysis for Emerging Technologies II (NMAET II)*** Teddington 17-18 Oct 2006.
- **F. Xu**, P. E. Horak, and G. Brambilla, “Conical and bi-conical ultra-high-Q optical-fibre-nanowire microcoil resonator”, ***APOC 2006*** Gwangju Korea 3-7 Sep 2006.